UC Davis
UC Davis Electronic Theses and Dissertations

Title

Magnetless Non-reciprocal Microwave Components Based on Spatial Temporal Modulation of Higher Order Coupled Resonators

Permalink

https://escholarship.org/uc/item/8884j06w

Author

Nafe, Mahmoud

Publication Date

2021

Peer reviewed|Thesis/dissertation

Magnetless Non-reciprocal Microwave Components Based on Spatial
Temporal Modulation of Higher Order Coupled Resonators

By

MAHMOUD NAFE
DISSERTATION

Submitted in partial satisfaction of the requirements for the degree of

DOCTOR OF PHILOSOPHY

in

Electrical and Computer Engineering

in the

OFFICE OF GRADUATE STUDIES

of the

UNIVERSITY OF CALIFORNIA

DAVIS

Approved:

Juan Sebastián Gómez-Díaz, Chair

Anh-Vu Pham

Xiaoguang Liu

Committee in Charge

2021

To my parents, Ali and Ola, who sacrifice everything for their children.

To my brother, Ahmed, who is my backbone and role model in life.

To my sister, May, whose kindness knows no bounds.

CONTENTS

LIST OF FIGURES

List of Tables

<div align="center">ABSTRACT</div>

<div align="center">**Magnetless Non-reciprocal Microwave Components Based on Spatial Temporal Modulation of Higher Order Coupled Resonators**</div>

Full duplex communication has gained tremendous interest over the past few years. This is because, it can theoretically double the maximum achievable data rate in a given bandwidth. This is achieved by allowing the simultaneous transmission and reception over the same channel. Such an increase in the data rate, or spectrum efficiency in general, has the potential to be used with future cellular network in order to support applications with heavy data traffic demands, such as autonomous vehicles, virtual reality, and the internet-of-things. A bottleneck challenge facing full-duplex communication is the problem of self interference, which is caused by the leakage of the high power transmitted signal into the receiver. The self-interference can be stronger than the desired signal by $90\,\mathrm{dB}$ or more causing the receiver to de-sensitize. To suppress the self-interference, a circulator is needed at the antenna-air interface to provide a 20-25 dB of isolation between the transmitter and the receiver.

Circulators are non-reciprocal devices that allow only one direction of wave propagation. Traditionally, they are designed using ferromagnetic materials biased by either a magnet or a current. As a result, they are bulky in size and expensive. Moreover, ferromagnetic materials are non-compatible with IC fabrication processes, therefore it hinders the integration of the circulator with the transceiver RFICs. Consequently, circulator-based full-duplex transceivers are deemed impractical. Recently, space-time modulation of the dielectric permittivity is shown to break the reciprocal signal transmission response. Upon modulating the permittivity of conventional substrates by a sinusoidal signal that traverses the substrate in clockwise/anti-clockwise direction, a preferred sense of rotation is imparted. As a result, at a given frequency only one direction of propagation is allowed. This is analogues to the alignment of magnetic dipole moments of magnetic material upon biasing it by an external magnetic field, which breaks the bi-directional wave propagation.

Although various magnetic-free circulators based on spatial-temporal modulation are demonstrated in literature showing excellent performance in terms of low insertion loss, good impedance matching, deep isolation of more than 50 dB, and high linearity and power-handling, the 20-dB isolation bandwidth is still limited to 5-7 %. This limitation is primary due to the use of first order resonant circuits, which are intrinsically narrowband.

In the first part of this dissertation, this problem is tackled through the use of higher order coupled resonators. Moreover, a generic methodology is proposed to synthesize a network to satisfy a desired 20-dB isolation bandwidth. This is achieved by utilizing microwave filter design theory and techniques. For demonstration, a magnetic-less circulator with a wideband 20-dB isolation fractional bandwidth is designed and fabricated at 500 MHz. The architecture of the proposed circulator is composed of a second order coupled resonators connected in a Y-topology. The fabricated prototype shows a 20-dB isolation fractional bandwidth of 15.4%, insertion loss of 4 dB, and is well-matched across the circulator passband.

In the second part of this dissertation, the space-time modulation is incorporated into the co-design of a magnetic-free isolating and filtering 3-dB microwave power-divider. The proposed circuit is composed of two branches each containing three coupled resonators. The circuit is analyzed using the coupling matrix for proper adjustment of the filter electrical parameters to allow the power-splitting operation. Moreover, the resonant frequency of each resonator is modulated spatially and temporally to break the reciprocal response, i.e. it allows only forward transmission. As a proof-of-concept, the resonators are implemented using folded $\lambda/2$ varactor-loaded distributed resonators at a center frequency of 900 MHz with a 3-dB fractional bandwidth of 5 %. The measured results show an insertion loss of 3.37 dB, a port-to-port isolation better than 20 dB across the band, a 20-dB reverse transmission isolation bandwidth of 45 MHz, and an impedance match at all ports better than 10 dB across the operating bandwidth.

Zhigang Peng, and Jie Wang. You all made my time at UCDavis much more enjoyable and fun. To Li, Xiaonan, and Jingjun: I will miss our daily lunch/dinner at the Tercero dinning commons. Thank you Jungjun for spending your Saturdays teaching me how to drive. I passed my behind-the-wheel test in one attempt thanks to you. I would like to thank Dr. Xiaohu Wu who I consider my co-advisor. He taught me how to design microwave filters. I cannot image how hard my PhD could have been without our daily discussions, and brainstorming. To Saleh, I will miss our conversations over your delicious Iranian tea. I wish you all the best in your PhD journey. To Daniel, thank you for always being my go-to-person for advice and for teaching me how to properly solder PCBs. To Hind, I cannot thank you enough for offering to help with the layout of my first PCB. I was short on time, and never used Allegro. Simply, you saved the day. To Naimul and Hao, thank you for your advice and effort, which made it easy for me to land an internship opportunity at Skyworks.

Fourth, I would like to thank everyone at the Islamic Center of Davis and the UCDavis Muslim Student Association. You really made me feel home. To Khalid Shahin, Ahmed El-Moghazy, and Tarek Diab: I will always cherish our outings together every Saturday when we either drank coffee at Starbucks or ate ice cream at MacDonald's. Those few hours we spent together really helped to wash away the fatigue and tiredness of working late-hours in the lab during the week, and re-charged my battery for working even harder the following week. To Assem Elshimi, I simply value our friendship. Your encouraging words always boost my confidence. Thank you for showing me around Austin/Texas and for the countless times you invited me to enjoy your delicious homemade koshary.

Fifth, I would like to thank the amazing team at Skyworks. To my mentor Harish Muthali, Thank you for finding the time out of your busy schedule to meet with me as many times as I needed (even on weekends). Working with you truly made significant difference in my technical background and skills. I am also touched by how you care about my welfare; always asking me about my parents, and how do I manage my accommodation and commute. To Nick Cheng, thank you for always giving me valuable career advice. Every discussion with you creates a clear picture of how my next five years would be.

This motivates me beyond imagination. To Qi Zeng, thank you for teaching me every single step in the simulation and optimization of a multi-chip-module. To Hai Ta, thank you for teaching me the theory and design of Baluns. To Grace Milroy, Mengping Yu, Lada Tith, and Mark Dang: thank you all for being so welcoming and approachable. You really made my internship fun and enjoyable.

Last but not least, I would like to thank my family in Egypt. My father, Ali, my mother, Ola, my brother, Ahmed, and my sister, May. Your love and prayers played a major role in achieving this milestone in my career. They lifted me up and motivated me to continue despite all the challenges and stresses of a PhD work. I dedicate this work in its entirety to you.

Chapter 1

Introduction

1.1 Overview of Electromagnetic Reciprocity

1.1.1 Time-Reversal Symmetry and Reciprocity Theorem

Every electrical engineer who studied an introductory course in electromagnetics or microwave engineering should have encountered the term reciprocity or non-reciprocity. In the analysis of microwave networks, a generic network is considered to be reciprocal if the off-diagonal elements of its scattering parameters (S-parameters) are equal, which can be described mathematically as

$$\mathbf{S} = \mathbf{S}^T \tag{1.1}$$

, where T corresponds to the transpose operation and $\mathbf{S}$ is the network S-parameters matrix [12]. While this elegant definition seems simple, in fact it took scientists decades of huge efforts to study and analyze the phenomenon of reciprocity. Reciprocity is a fundamental property that occurs in the various fields of study, such as mechanics, thermodynamics, electromagnetics, optics, and circuits. The early efforts of scientists were focused on analyzing physical laws and media under time-reversal. As its name suggests, time-reversal is, generally speaking, going backward in time (similar to rewinding a recorded movie). A system is set to be time-reversal invariant or follows the property of time-reversal symmetry (TRS) if and only if, the backward evolution in time returns the objects/variables to their original state/value [1]. Fig 1.1 depicts an example, where one can observe the evolution of a process in a given system with time. At a give time t,

1
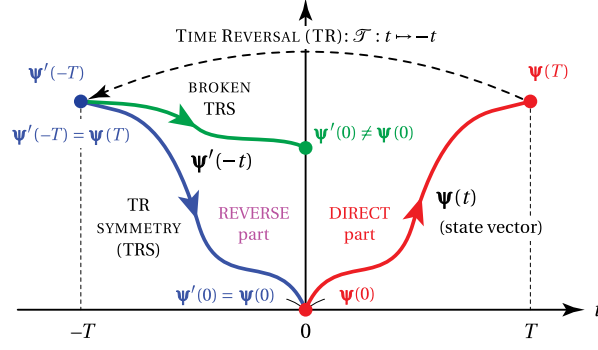
Figure 1.1: Illustration explaining time-reversal symmetry. Here under time-reversal ($t \to -t$), the process represented by the red and blue curves starts and ends at the same state, thus it follows TRS. Meanwhile, the process represented by the red and green curves has different start and end states, therefore it breaks the TRS. [1]

the state of the process is described by $\Psi(t)$. First, the process is observed from $t = 0$ to $t = T$, then the sign of the time variable is reversed. As a result, the system is now excited at $t = -T$ and is monitored up to $t = 0$. This operation is referred to as time-reversal, and is described mathematically as

$$\mathcal{T}\{t\} = t^{'} = -t \qquad (1.2)$$

, where $\mathcal{T}$ is a time-reversal operator [2]. Moreover, when the time-reversal operator is applied to the state $\Psi(t)$, it follows

$$\mathcal{T}\{\Psi(t)\} = \Psi^{'}(t^{'}) = \Psi^{'}(-t). \qquad (1.3)$$

, where $\Psi^{'}(t^{'})$ is the state of the process upon time-reversal ($t^{'} = -t$). Based on (1.2) and (1.3), a system is time-reversal symmetric if the direct path (red curve) and the reverse path (blue curve) are symmetric around y-axis. If the reverse path ends at a different state compared to the direct path (green curve), therefore the system is time-reversal asymmetric [2]. Mathematically, TRS-systems must satisfy

$$\mathcal{T}\{\Psi(t)\} = \Psi^{'}(-t) = \Psi(t). \qquad (1.4)$$

Having discussed the concept of time-reversal symmetry, it should be noted that although the laws of physics are themselves invariant, their respective physical quantities may have even (TRS) or odd (anti-TRS) time-reversal parity [1]. In regards to the field of
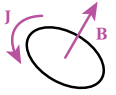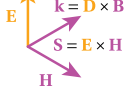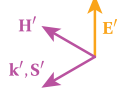
$f(t)$ $\xrightarrow{\mathcal{T}}$	$f'(t') = \pm f(-t)$	FIELD – PARITY
q	$q' = q$	q, ρ – even
$\mathbf{E}$	$\mathbf{E}' = \mathbf{E}$	$\mathbf{E}, \mathbf{P}, \mathbf{D}$ – even
$\mathbf{J}$, $\mathbf{v}$	$\mathbf{J}' = -\mathbf{J}$, $\mathbf{v}' = -\mathbf{v}$	$\mathbf{v}, \mathbf{J}$ – odd
$\mathbf{J}$, $\mathbf{B}$	$\mathbf{J}'$, $\mathbf{B}' = -\mathbf{B}$	$\mathbf{B}, \mathbf{M}, \mathbf{H}$ – odd
$\mathbf{E}$, $\mathbf{k} = \mathbf{D} \times \mathbf{B}$, $\mathbf{S} = \mathbf{E} \times \mathbf{H}$, $\mathbf{H}$	$\mathbf{H}'$, $\mathbf{E}'$, $\mathbf{k}', \mathbf{S}'$	$\mathbf{k}, \mathbf{S}$ – odd
$\eta = E / H$	$\eta' = E'/H' = -\eta$	η – odd
$\alpha = \Im\{k\} < 0$ loss	$\alpha' = \Im\{k'\} = -\alpha > 0$ gain	α – odd

Figure 1.2: Time-reversal parity of the various electromagnetic physical quantities. [1]

electromagnetics, Fig. 1.2 summarizes the time-reversal parity of relevant physical quantities. The parity of each quantity is determined by applying (1.2) and (1.3) to fundamental electromagnetic laws, such as Coulomb-, Faraday-, Ampere-, and Gauss-law. Moreover, by following the time-reversal parity of electric and magnetic fields and applying the time-reversal operator to both sides of Maxwell equations, it is straight-forward to show that Maxwell equations are TRS [1]. This important fact shows that if all quantities in a system are time-reversed (following the rules in Fig 1.2), then the solution to Maxwell equations will remain the same in both the direct and reverse systems. Moreover, violating one rule would result in breaking the time-reversal symmetry.

In the field of electromagnetics, it is common to think in terms of a source and an observation point. Therefore, scientists in this field tend to think of the reverse path (Fig. 1.1) as swapping the locations of the source and the observation point. Moreover, if the field generated at the observation point in both cases is the same, therefore the wave propagation/transmission in this medium/system is set to be bidirectional/reciprocal [13]. Considering the situation depicted in Fig. 1.3, for a system/medium to be reciprocal it
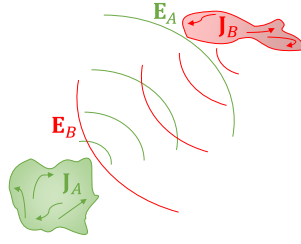
Figure 1.3: Illustration showing two electric current densities and their respective electric fields. [2]

must satisfy the reciprocity theorem

$$\iiint_V J_A E_B \, dv = \iiint_V J_B E_A \, dv \qquad (1.5)$$

, where J_A and J_B are electric current densities located in different locations (enclosed in a volume V) and E_A and E_B are the electric fields associated with each current density. Furthermore, it was shown that any non-magnetic, linear, passive, and time-invariant system/medium satisfies (1.5), and hence is reciprocal. It is worth mentioning that in electronic circuits, operating at low frequencies, another form of reciprocity theorem is used

$$V_1 I_2 = V_2 I_1 \qquad (1.6)$$

, where V_1 is the voltage applied at port 1 and I_1 is the corresponding current flowing into the port [12]. Similarly, V_2 and I_2 are the voltage and current at port 2, respectively.

1.1.2 Techniques to Break the Reciprocity Theorem

Breaking the reciprocity theorem would give rise to the development of novel electronic components, such as isolators, circulators, gyrators, and non-reciprocal phase shifters. These components are vital for a variety of applications, such as wireless communications, biomedical, radar, and quantum computing. As explained in the previous section, if a system/device satisfies all the following conditions: contains/constitutes of a dielectric material with symmetric permeability- or permittivity- tensor, linearity, passivity, and time-invariance, it must obey the reciprocity theorem. Conversely, breaking only one of these conditions is enough to violate the reciprocity theorem, and hence allows the system/device to have a non-reciprocal transmission response. In the next sub-sections,

4

a brief review of the research that was conducted into breaking the reciprocity theorem (and building non-reciprocal components) is presented.

1.1.2.1 Using Magneto-optic Effect

Historically, non-reciprocity was first achieved through the use of ferromagnetic materials. In these materials, the magnetic dipole moments can be aligned by an external magnetic field, which causes the permeability tensor to become asymmetric (such interaction is known as magneto-optic effect) [3]. It is worth mentioning that, in the optical regime it is the permittivity that becomes tensorial and asymmetric (due to the cyclotron orbiting). To illustrate how the wave-material interaction becomes direction-dependant (due to the magneto-optic effect), let us consider a ferromagnetic circular slab biased with an external magnetic field $\overrightarrow{H} = H_0 \, \hat{a}_z$ as shown in Fig. 1.4. When a wave is incident upon the slab with a magnetic field of $\overrightarrow{H_{inc}} = H_x \hat{a}_x + H_y \hat{a}_y + H_z \hat{a}_z$, a magnetization vector $\overrightarrow{M}$ is induced inside the material which is expressed as

$$\overrightarrow{M} = \begin{bmatrix} \chi_{xx} & \chi_{xy} & 0 \\ \chi_{yx} & \chi_{yy} & 0 \\ 0 & 0 & 0 \end{bmatrix} \times \begin{bmatrix} H_x \\ H_y \\ H_z \end{bmatrix} \tag{1.7}$$

, where χ_{ij} are the material magnetic susceptibilities. From (1.7), the magnetic flux density can be deduced

$$\overrightarrow{B} = \mu_0 \left(\overrightarrow{H_{inc}} + \overrightarrow{M} \right) = \begin{bmatrix} \mu_0(1 + \chi_{xx}) & j\mu_0\chi_{xy} & 0 \\ -j\mu_0\chi_{xy} & \mu_0(1 + \chi_{yy}) & 0 \\ 0 & 0 & \mu_0 \end{bmatrix} \overrightarrow{H_{inc}} \tag{1.8}$$

, where μ_0 is the free space permeability [3]. It follows from substituting (1.8) into Maxwell equations that a biased ferromagnetic material has two different propagation constants for left- and right-handed circular wave polarizations [3]. As a result, a linearly polarized wave (combination of left- and right-handed circularly polarized waves) experiences a rotation angle

$$\theta_F(z) = -\frac{(\beta_+ - \beta_-) \, z}{2} \tag{1.9}$$

, where β_+ and β_- are the propagation constants for left- and right-handed circularly polarized waves, respectively. Because of the resulting rotation, the magneto-optic effect
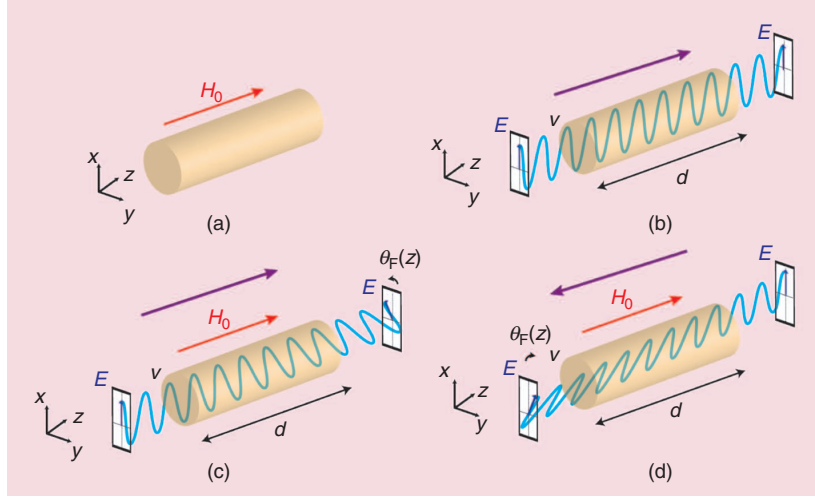
Figure 1.4: Illustration showing the magneto-optic effect. (a) Ferromagnetic material of length d under external magnetic field H_0. (b) An incident linearly polarized wave experiences no rotation in the absence of H_0. (c) Forward propagation from left to right through the biased material causes a positive rotation in the polarization plane. (d) Backward propagation from right to left has a reversed sense of rotation causing a negative rotation in the polarization plane. [3]

is also commonly referred to as Faraday rotation (in recognition of Michael Faraday who introduced and studied this concept).

Fig 1.4 (b) shows the case of no external bias, and as a result both propagation constants become equal. Therefore, no rotation occurs to the polarization of the incident wave. On the other hand, under external bias (Fig 1.4 (c)), the polarization gets rotated to an angle θ_F, which depends on the strength of external biasing field and the length of the ferromagnetic material. Moreover, when the incident wave travels in the opposite direction (Fig 1.4 (c)), or equivalently rotating the direction of the biasing magnetic field, the sense of rotation is reserved. Consequently, the forward and backward traveling waves experience different rotation angles, and thus a non-reciprocal transmission phase is achieved.

Magneto-optic effect or Faraday rotation was used in the realization of various non-reciprocal electronic components [4, 5]. For instance, Fig. 1.5 (a) shows a microstrip implementation of a microwave circulator, where a ferrite disk is inserted into the dielectric substrate. Without external bias, the magnetic moments are randomly oriented in space
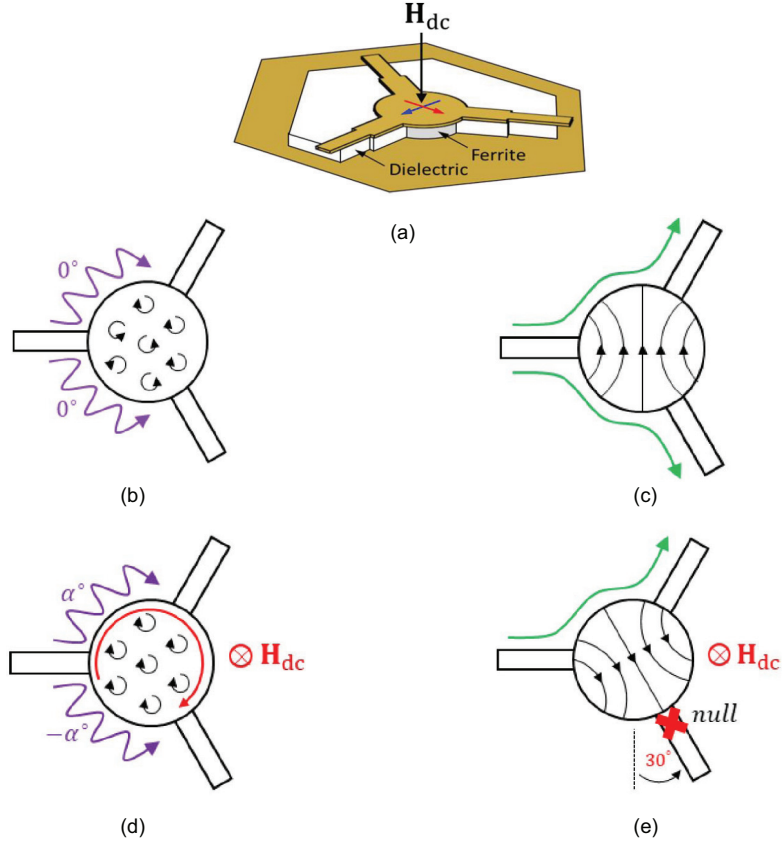
Figure 1.5: Microwave circulator based on ferrite disk. (a) Ferrite disk inserted in the microstrip dielectric substrate. In the un-biased state, the magnetic dipole moments are randomly oriented (b) and overall field is distributed equally at the output ports (c). Under external bias, the magnetic dipole moments are aligned (d) a null in the overall field can be created at one of the output port (e). [4, 5]

(Fig. 1.5 (b)), which causes the guided modes rotating clockwise and anti-clockwise to have the same cut-off frequency (i.e. the degeneracy is lifted).

As a result, when a signal is incident from one port, the power gets split equally at the output ports (the overall field distribution is the same at the output ports as shown in Fig. 1.5 (c)). When the ferrite disk is biased with an external field H_{dc}, the magnetic dipole moments are aligned in one direction to generate a magnetic field along that of the external field (Fig. 1.5 (d)). Consequently, one direction of rotation is more favored by the disk, which causes the clockwise and anti-clock wise modes to have different wave velocities and propagation constants. Therefore, their cut-off frequencies become different (i.e. the degeneracy is lifted). Moreover, the strength of the external biasing field can

be chosen such that the overall field distribution shows a null at one output port, and maximum at the other port as depicted in Fig. 1.5 (e). Since, the structure has circular symmetry, therefore the any input power from one port will rotate to the neighbouring port yielding the functionality of a circulator.

Magnetic-based circulators have the advantage of high linearity and power handling. Commercial magnetic-based circulators show a third-order input intercept point in the range of $70 - 80$ dBm [3]. This made them a suitable candidate for military applications, where transceivers operate with extremely high power signals. On the other hand, the use of ferrites results in bulky and heavy non-reciprocal devices, which makes them not suitable for applications requiring low weight transceivers, such as wearable electronics. Moreover, ferrites/ferromagnetic materials are not compatible with IC fabrication processes. This hinders their integration with other CMOS-based front-end modules, which causes an increase in the module overall cost [3].

1.1.2.2 Using Active Devices

With the development of transistors, active or transistor-based non-reciprocal devices have gained tremendous interest owing to the possibility of integrating a whole transceiver (that contains isolators and circulators) on chip. A transistor is intrinsically unidirectional, since an input signal at the transistor gate can be amplified at the drain, but not vice versa. Based on that Tanaka et al., proposed the first transistor-based circulator whose schematic is shown in Fig. 1.6 [6]. The schematic is composed of a cascade of three common-source single stage amplifiers. The circulator ports are connected to the transistor gate of each stage. It should be noted that since the schematic does not contain any reactive components, therefore the circuit performance was wideband. On the other hand, this design is sensitive to matching, since any reflection can leak into the neighbouring ports leading, which will travel till it reaches the other third port i.e. any reflection due to mismatch will cause reduction in the isolation.

Another recent implementation of transistor-based non-reciprocal microwave devices was suggested by Kodera et al., where a transistor is loaded into the gap of a split-ring resonator as shown in Fig. 1.7 (a) [14]. The non-reciprocity is achieved since the transitor
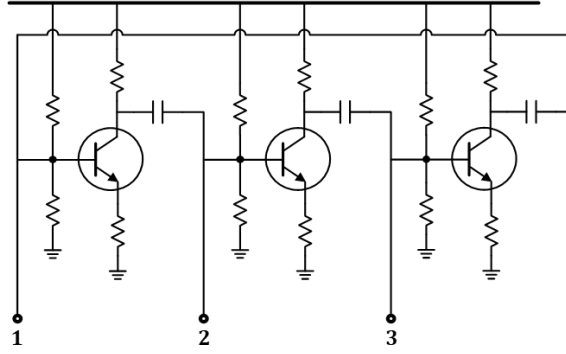
Figure 1.6: Transistor-based circulator composed of a three stage common source amplifier. [4,6]

will only allow currents to flow in an anticlockwise direction i.e. only through its drain. A RF isolator (Fig. 1.7 (b)) is created by using a two-metal layer substrate, where a transmission line and an array of transistor-loaded split-ring resonators are placed on the top and bottom layers, respectively. When a signal travels from port 1 to port 2, a current is induced at the bottom array of split-ring resonators. Following the right-hand rule, the direction of current flow is anticlockwise, hence the transistor will allow the flow of current. In this case, the transmission line will experience a relatively small equivalent resistance, and the signal will travel without attenuation. On the other hand, a signal traveling in the opposite direction will induce a current that flows into the gate of the transistor. As a result, the transmission line will be loaded by a large equivalent resistance, which causes the signal to attenuate as it travels down the transmission line. In a similar fashion, a circulator can be implemented utilizing the same technique by simply adding a third port as shown in Fig. 1.7 (c).

Although using transistors to design non-reciprocal components greatly reduce the size and fabrication cost, this came on the expense of poor linearity and noise performances. This is because active devices generate additional noise and distortion. As a result, devices implemented with this approach are only suited for biomedical applications [15]. In particular, they are not suited for integration with RF front-ends used in cellular wireless applications [3].
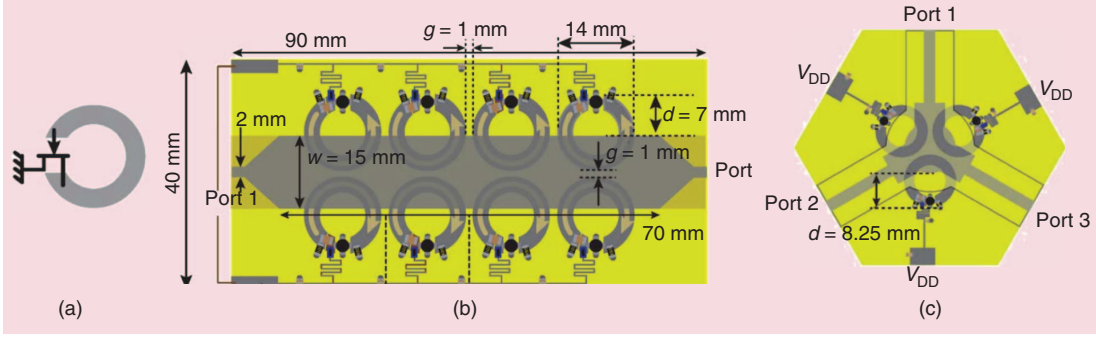
Figure 1.7: Implementation of transistor-based non-reciprocal devices using (a) transistor-loaded split-ring resonator. (b) isolator, and (c) circulator. [3, 7]

1.1.2.3 Using Non-Linear Effects

In both of the aforementioned reciprocity-breaking techniques, an external bias (magnetic field or dc supply voltage) is needed, which either increases the overall size or consumes power. Using non-linearity tackles this issue since the reciprocity is broken due to the non-linear characteristics of the constitutive material or resonator themselves, and not with the aid of an external bias. For instance, in the optical regime the material permittivity is described by Kerr-effect as

$$\epsilon = \epsilon_0(\chi^{(1)} + 3\chi^{(3)}|E|^2) \qquad (1.10)$$

, where $\epsilon_0\chi^{(1)}$ is the linear permittivity of the medium, $\chi^{(3)}$ is the third-order non-linear susceptibility, and E is the electric field intensity [16]. Fig. 1.8 shows an optical isolator, which is realized by cascading two media between two ports. The first material is a linear lossless one with real permittivity of ϵ_1, while the second is a non-linear material with a complex permittivity of $\epsilon_2' - j\epsilon_2''|E|$. It should be noted that the losses in the second medium is dependant on the intensity of the incident electric field.

The principal of operation is as follows: when a signal is injected at port 1, it will experience a linear medium with low loss. Therefore, the signal will travel with minimum attenuation until it reaches the interface between the two media. At the interface, a large reflection will occur due to the mismatch between the reflection coefficients of the two media, and a small portion of the signal will get transferred into the second medium. This small portion will not be large enough to trigger the second medium non-linear behaviour,
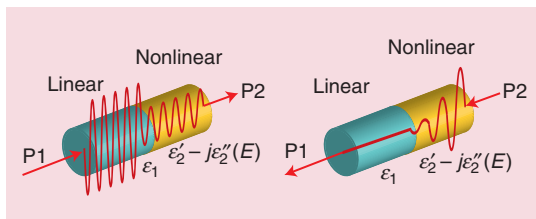
Figure 1.8: Demonstration of an optical isolator constructed by creating a spatially asymmetric structure (a cascade of linear and non-linear media). [3]

and hence it will reach port 2. In the opposite transmission direction, the signal will first experience a large attenuation, which will lead to the signal reaching the interface to have a small amplitude. Taking into account the reflection at the interface, the amplitude of the signal reaching port 1 will be negligible.

Based on the above explanation, one can infer that the non-reciprocal behaviour is dependant on the signal amplitude. As a result, there is a trade-off between the magnitude of forward transmission and the range of signal amplitudes at which the directivity (defined as the ratio between forward and backward transmission) is large. Another limitation to this approach is that it was shown in [17] that the reciprocity can not be broken if both ports are excited simultaneously. Despite these shortcomings, the above optical isolator can be used in optical systems that incorporate pulsed-radars, such as LiDAR systems [18].

1.1.2.4   Using Time-variant Media

Time-variant media are defined as media whose one of their electrical properties (permeability, conductivity, or permittivity) are changing, continuously or discretely, with time. Using time-variance to break the reciprocity theorem aims at developing non-reciprocal devices that are linear and passive. As a result, the developed devices can simultaneously handle more power and exhibit low noise figure. This makes such devices an attractive choice for futuristic wireless applications, such as full-duplex systems.

Interestingly, before the advent of transistors, time-variance was first used to implement parametric amplifiers [19,20]. The architecture of parametric amplifiers is composed of a transmission line, which is loaded periodically in space with varactors. In addition, the varactors are modulated by a sinusoidal signal, which is referred to as a pump sig-

11

nal. The pump signal role is to effectively change the transmission line characteristics, and thus a wave traversing the transmission line experiences a time-varying medium. Recently, Qin *et al.* [8] demonstrated that a circulator can be implemented under the following conditions

$$\omega_m = \omega_s \pm \omega_p, \quad \beta_m = \beta_s \pm \beta_p \tag{1.11}$$

, where ω_m, ω_s, and ω_p are the angular frequencies of the up/down-converted signal, the source signal, and the pump signal, respectively, and β_m, β_s, and β_p are their corresponding wave-numbers. It should be noted that the above equation is only satisfied when the source and pump signals propagate in the same direction. The proposed circulator architecture is shown in Fig. 1.9, which is composed of a differential transmission line, a transceiver, an antenna, and a pump signal source. Moreover, the pump signal is injected into the transmission line from the antenna side, where in the receive mode after a certain transmission line length, the received signal is fully down-converted to another frequency due to the mixing between the pump and the received signals. Meanwhile, in the transmit mode the transmitted and pump signals propagate in opposite directions, which makes (1.11) hard to satisfy. As a result, the transmitted signal reaches the antenna without being converted to another frequency.

Moreover, an additional duplexer is needed to provide sufficient isolation between the transmitter and the receiver. This causes an additional increase in the circulator insertion
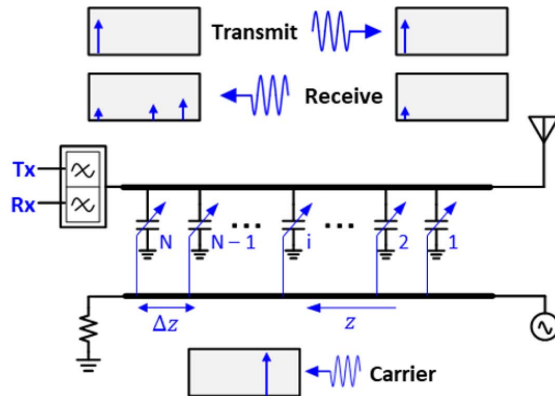
Figure 1.9: Architecture of a RF Circulator based on time-variant transmission lines proposed in [8].

loss (IL), and limits the bandwidth of operation to the duplexer operation bandwidth. To alleviate the use of duplexers, non-reciprocal transmission at same frequency is in demand. To that end, Dimitrious *et al.* [10] proposed the use of Angular Momentum Biasing (AMB) to bias materials and break the reciprocity theorem. As discussed earlier, the application of a magnetic field aligns the magnetic dipole moments of a ferrite material causing the material to allow only one direction of wave propagation (Fig. 1.10 (a)). In a similar fashion, changing the permittivity of a circular dielectric substrate with a sinusoidal signal that traverse the substrate in clockwise/anticlockwise direction imparts a preferred sense of rotation in the substrate (Fig. 1.10 (b)). As a result, at a given frequency only one direction of rotation is guided in the medium as shown in Fig. 1.10 (c).
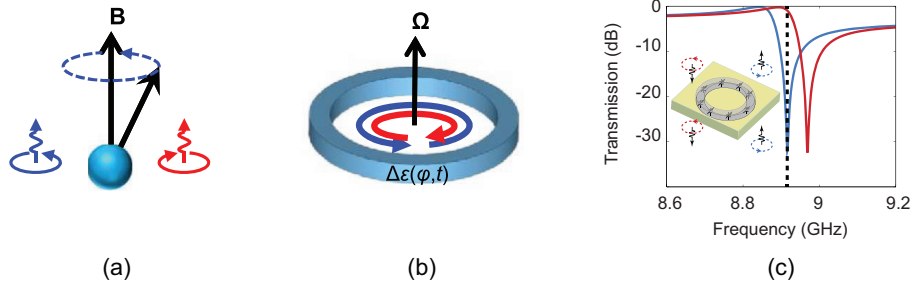
Figure 1.10: Breaking non-reciprocity using (a) magnetic bias and (b) angular momentum bias. (c) non-reciprocal transmission [9, 10].

Recently, spatial-temporal modulation (STM) is introduced as an efficient method to implement RF circulators using AMB [9]. Instead of modulating a continuum medium, the dielectric ring resonator is split into three coupled resonators as shown in Fig. 1.11 (a). Moreover, the resonance frequency of each resonator is modulated by a sinusoidal signal. Furthermore, there is a progressive phase shift of 120° between the modulating signals. Figures 1.11 (b) and 1.11 (c) depict the schematic and PCB implementation of the resonators using lumped components (LC tanks). Mathematically, the instantaneous frequency of the nth resonator can be described as

$$f_n = f_0 + \Delta f \cos[2\pi f_m t + (n-1)\frac{2\pi}{3}] \tag{1.12}$$

, where n = 1,2,3, f_0 is the tank static (un-modulated) resonant frequency, and f_m and Δf are the modulation frequency and depth, respectively. It is worth mentioning that

13
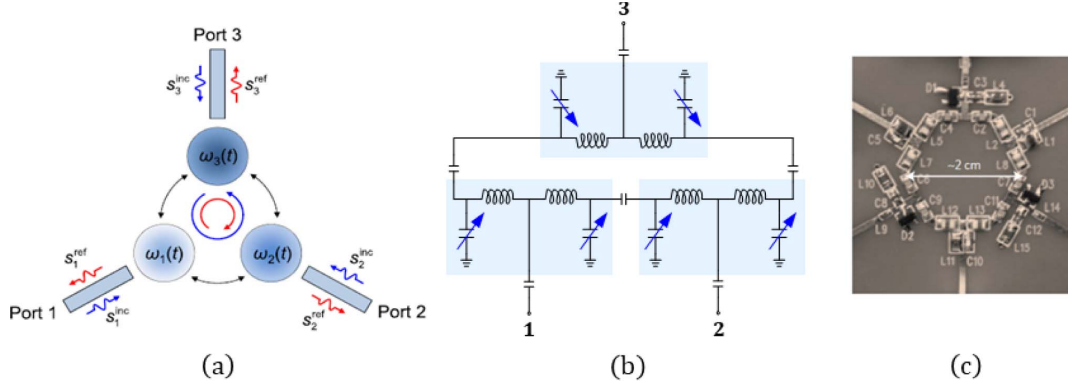
Figure 1.11: (a) Implementation of angular momentum biasing through the spatial-temporal modulation of three coupled resonators, and corresponding (b) schematic and (c) fabricated PCB. [4]

the nomenclature of spatial-temporal modulation stems from the fact that the resonators are distributed in space and are being modulated by a time varying signals.

Afterwards, Kord *et al.* [5,21] fully analyzed the architecture proposed in [9], where he was able to demonstrate that there are four possible schematics as shown in Fig. 1.12 for realizing a STM-based RF circulator. These structures originate from the combination of a series (bandpass) or a shunt (bandstop) LC resonator connected in a Y or a Δ topology. In addition, he provided a detailed analysis based on KCL/KVL equations, which helped to choose the modulation parameters that optimize the circulator overall performance. For demonstration, he designed a circulator based on bandstop/Δ structure, where the measured results showed insertion loss of 3.3 dB, return loss (RL) of 10.8 dB, isolation (IX) of 55 dB, and a 20 dB IX fractional bandwidth (FBW) of 6 % [21].

In order to reduce the strength of the intermodulation products, which are generated due to the mixing between the RF signal and the modulating signal, Kord *et al.* in [22] combined two single-ended circulators with opposite circulatory directions to form a differential circulator. It was shown that the higher order intermodulation products are significantly reduced when combined/summed at the RF ports, leading to an improvement of about 19 dB in terms of maximum intermodulation products.

Table 1.1 summarizes the advantages and disadvantages of all the reciprocity-breaking approaches, which are discussed in this chapter. From the table, it is clear that using
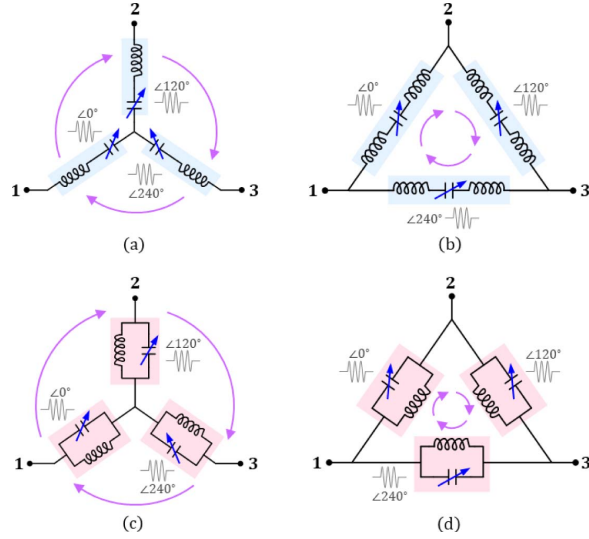
Figure 1.12: Possible architectures for STM-based single-ended circulators: (a) series LC (bandpass) connected in a Y, (b) series LC (bandpass) connected in a Δ, (c) shunt LC (bandstop) connected in a Y, and shunt LC (bandpass) connected in a Δ. [4]

magneto-optic effects (magnets/magnetic materials) leads to devices with excellent performance in terms of low insertion loss, and high linearity and power handling. However, they are expensive and heavy. This makes them a prime candidate for military applications. In addition, among the magnetic-free techniques, time variance stands out as the approach that produces devices with a good compromise among the listed metrics. Therefore, this approach has been attracting great deal of interest for its potential usage in the various commercial applications, such as full-duplex systems [23], radar [24], and quantum computing [25–27].

1.2 Full-Duplex Communication

The electromagnetic spectrum is a congested and scarce resource in wireless communication. In addition, it is expected that there will be tremendous increase (1000-fold) in the required network capacity and data rates of the upcoming 5G cellular network, which are needed to support applications, such as downloading high-definition videos in few seconds, virtual reality, autonomous vehicle, and the internet-of-things. Therefore, an efficient way is needed to utilize the band of frequencies that will be allocated for a given application. In traditional wireless transceivers, half-duplexing (HD) was introduced to

Table 1.1: Comparison of the performance of non-reciprocal devices implemented using the different reciprocity-breaking techniques

Technique	Magneto-Optic	Active	Non-Linearity	Time Variance
Bias	Magnetic	dc supply	N/A	Space/Time-varying signals
Size	Large	Small	Small	Small-Medium
Cost	High	Low	Low	Low
Insertion Loss	Low	Low-Gain	Medium	Low-Medium
Isolation	Medium	Medium-High	Low	Medium-High
Bandwidth	Wide	Average	Low	Average-Wide
Power Handling	High	Low	Low	Medium
Linearity	High	Low	Low	Medium
Noise Figure	Low	High	Medium	Low-Medium
Power Consumption	Low	High	Low	Low-Medium

avoid any interference between the transmitter and the receiver since they are both located on the same device. There are two forms of HD, namely time-division duplexing (TDD) and frequency-division duplexing (FDD). In TDD, the transmitter and receiver communicate over the same channel/frequency, however they use different time slots to transmit/receive. Meanwhile, in FDD, the transmitter and receiver operate at all time, however they are separated in frequency channels. In both cases, the spectral efficiency is sacrificed in order to avoid any self-interference (interference due to the leakage of the transmitted signal into the receiver). [28, 29]

Recently, full-duplex communication systems have been introduced as an efficient way to make use of the spectrum. This is because in FD, the transmitter and receiver communicate simultaneously at the same time and frequency. Therefore, the network data-rate and capacity can theoretically be doubled in comparison to using TDD and FDD. Moreover, there are other advantages to using FD, such as the reduction of delays in relay-nodes. Fig. 1.13 (a) summarizes the time-frequency usage of the aforementioned duplexing techniques. [30, 31]

Since the transmitted signal can be in the order of 90 dB above the receiver noise
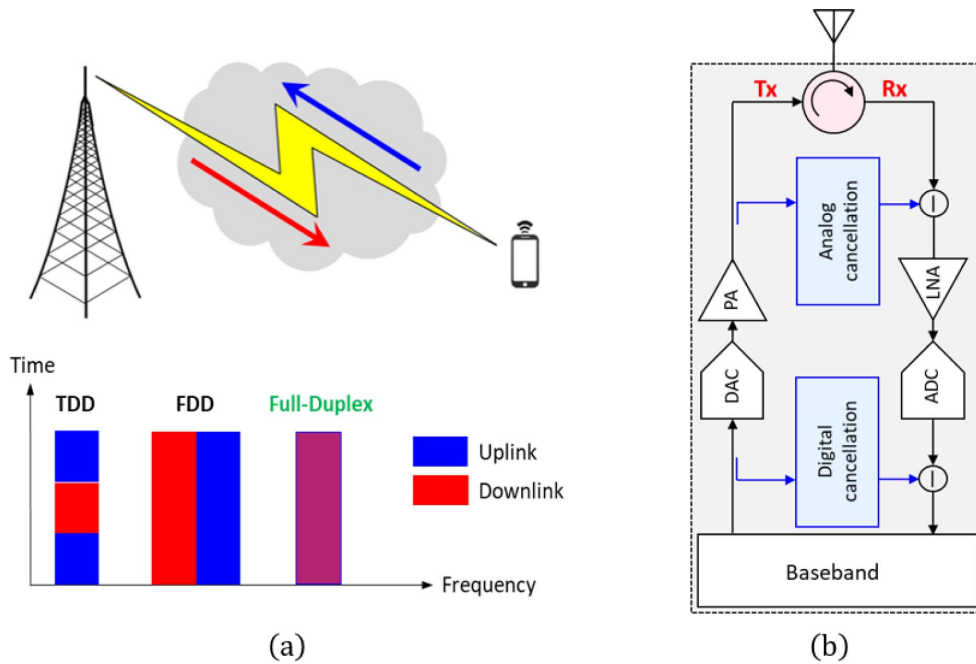
Figure 1.13: Illustration showing (a) frequency and time usage in TDD, FDD, and FD and (b) a FD transceiver with SI-cancellation circuits at the different locations along transceiver chain. [4]

floor, therefore the self-interference is considered the bottleneck for the deployment of FD in commercial wireless transceivers. As a result, the leaked transmitted signal can de-sensitize the receiver. To achieve a proper signal-to-noise ratio, self-interference cancellation of about 110 dB is required. Such a huge number can not be achieved at a signal stage rather it is often distributed at different locations along the receiver chain. Fig. 1.13 (b) depicts the SI-cancellation at the Digital-Analogue interface, Analogue-RF interface, and antenna-air interface. [32]

At the antenna-air interface, the SI-cancellation can be achieved through the use of circulators. A 20 dB of isolation is sufficient to relax the design of subsequent SI-cancellation circuits. It is worth mentioning that the use of circulators became an attractive choice after the introduction of time-variance as a magnet-free reciprocity breaking approach. Alternatively, balanced-duplexing circuits [33] or multiple antennas [34] were used to realize the required 20 dB isolation, however on the expense of a fundamental 3 dB loss or an increase in form-factor, respectively.

1.3 Dissertation Overview

As discussed in the previous section, the differential topology of STM-based circulators provided an excellent circulator performance in terms of IL, RL, IX, linearity, and power handling however, the 20 dB IX FBW was still about 4-6 %. In [35], the use of second order matching networks was proposed to improve the matching and isolation bandwidth. Despite, improving the isolation FBW to about 13.8 %, this came on the expense of an increase in the insertion loss to about 5 %. In addition, the measured passband was not flat, which could cause distortions when integrated with transmitters that use amplitude modulation.

In this dissertation, the application of spatial temporal modulation to higher order coupled resonators is investigated in order to widen the 20 dB IX FBW and improve the out-of-band rejection. In contrast to prior work, a design methodology is proposed to synthesize a circulator network to satisfy a targeted 20 dB IX BW. This is achieved through the use of the well-established microwave filter design theory and techniques. Moreover, a miniaturized RF front-end is demonstrated through leveraging the filter-coupled mode theory to co-design a novel power divider with the integrated functionalities of a bandpass filter and an isolator. It is worth mentioning that the isolator is magnetic-free i.e. implemented via STM of coupled resonators.

The dissertation is organized as follows:

Chapter 2 presents a magnetic-free circulator with a wideband 20 dB IX FBW. The proposed circulator is based on the spatial temporal modulation of second order LC resonators. Furthermore, a generic design procedure is illustrated, which is based on relating the circulator modulated IX FBW response with the 3 dB FBW of a static filter. Based on that, a circulator is designed and fabricated at 500 MHz achieving a measured 20 dB IX FBW of 15.4 %, low insertion loss of 4 dB, flat group delay across the bandwidth, and return loss of 12 dB.

Chapter 3 investigates the responses of higher order (2nd-, 3rd-, and 4th-) STM-based circulators. In particular, a comparison between the optimum modulated reflection, transmission, and isolation responses of each order is presented. In addition, the relationship

between the 20 dB IX FBW and the normalized modulation frequency is studied for all orders.Also, the insertion loss of single-ended and differential higher order circulators are studied and a lower-bound on the modulation frequency is found.

Chapter 4 demonstrates a novel 3 dB power divider with the integrated functionalities of a bandpass filter and an isolator. The bandpass filter is composed of a 3-pole Chebyshev filter with a modified input quality factor to take into account the power-splitter operation i.e. the addition of a second branch. The isolator is implemented by STM of the resonators in each branch. It is worth mentioning that the application of STM not only reduces the reverse transmission, but also improves the port-to-port isolation, which is about 10 dB in conventional microwave T-power dividers. A prototype is designed at 900 MHz, showing a measured IL of 3.37 dB, port-to-port isolation better than 20 dB across the bandwidth, 20 dB reverse transmission isolation bandwidth of 45 MHz (5 % 20 dB IX FBW), and all ports are well-matched (better than 10 dB across the operational bandwidth).

Lastly, Chapter 5 concludes and summarizes the work presented in this dissertation. In addition, several future work are suggested.

The main contributions of this work are either published or are currently being prepared for publication in the following conferences and journals:

- M. Nafe, X. Wu, and Xiaoguang Liu, "A Design Methodology For Wideband Magnetless Microwave Circulator Based on Spatial-Temporal Modulation of Coupled-Resonator Filters," IEEE Transactions on Microwave and Techniques (submitted).

- M. Nafe, X. Wu, and Xiaoguang Liu, "Novel Multi-functional Non-Reciprocal Filtering Microwave Power Divider Using Space-Time Modulated $\lambda_g/2$ Resonators," IEEE Transactions on Microwave and Techniques (submitted).

- M. Nafe, X. Wu and X. Liu, "A Wideband Magnetic-Free Circulator Using Spatio-Temporal Modulation of 2-pole Bandpass Filters," 2019 IEEE Radio and Wireless Symposium (RWS), 2019, pp. 1-3.

- Mahmoud Nafe, M. Naimul Hasan, Hind Reggad, Daniel Kuzmenko, Jingjun Chen, Xiaoguang Liu, "Magnetic-free Circulator Based On Spatio-Temporal Modulation

Implemented via Switched Capacitors for Full Duplex Communication," 2018 USNC-URSI Radio Science Meeting (Joint with AP-S Symposium), July, 2018.

- Xiaohu Wu, Mahmoud Nafe, and Xiaoguang Liu, "Non-Reciprocal 2nd-Order Bandpass Filter by Using Time-Modulated Microstrip Quarter-Wavelength Resonators," IEEE International Conference on Microwave and Millimeter-wave Technology, May, 2019.

- X. Wu, M. Nafe and X. Liu, "A Magnetless Microstrip Filtering Circulator based on Coupled Static and Time-Modulated Resonators," 2020 IEEE/MTT-S International Microwave Symposium (IMS), 2020, pp. 948-951.

- X. Wu, M. Nafe, A. Á. Melcón, J. S. Gómez-Díaz and X. Liu, "Frequency Tunable Non-Reciprocal Bandpass Filter Using Time-Modulated Microstrip $\lambda_g/2$ Resonators," in IEEE Transactions on Circuits and Systems II: Express Briefs, vol. 68, no. 2, pp. 667-671, Feb. 2021.

- Xiaohu Wu, Mahmoud Nafe, A. Álvarez Melcón, J. S. Gómez-Díaz, and Xiaoguang Liu, "A non-reciprocal bandpass diplexer," in International Journal of RF and Microwave Computer-Aided Engineering, vol. 31, no. 6, 2021.

Chapter 2

Wideband Magnetic-free RF Circulator Based on Spatial-Temporal Modulation of Second Order Coupled Resonators

In this chapter, we present a single-ended magnetic-free RF circulator with a broadband 20-dB isolation bandwidth. This is achieved through the use of spatio-temporal modulation angular momentum biasing of second order LC resonators connected in Y topology. In addition, we demonstrate a generic design procedure based on microwave filter design theory to build a three-fold symmetric static circulator response with a prescribed fractional bandwidth and operational frequency. As a proof of concept, we design a magnetic-free circulator at $500\,\mathrm{MHz}$ and fractional bandwidth of 25% using off-the-shelf lumped components. The simulated and measured data are in good match, showing a 20-dB isolation fractional bandwidth of 15.4%, insertion loss of $4\,\mathrm{dB}$, and is well-matched across the circulator passband.

2.1 Introduction

Numerous applications of wireless communication emerge everyday, and they all share the same resource that is the electromagnetic spectrum. Such congested spectrum as well as the ever lasting demand of improving the provided quality of service, such as

enabling high data rates in mobile communications, motivated researchers around the world to explore different methods to efficiently use that scarcely available spectrum. One promising approach is the use of Full Duplex (FD) systems, where simultaneous transmission and reception over the same frequency channels is permissible, and as a result the spectrum efficiency is theoretically doubled [30, 36, 37].

The main challenge that faces FD systems is the potential leakage of the transmitter (Tx) high power signal into the receiver (Rx) front end causing it to saturate, such problem is called Self Interference (SI). Although the amount of SI cancellation varies depending on the application, it is usually distributed across the receiver chain. One of those locations, also the first, is the air-antenna interface, where a 20-dB of cancellation is reserved. To that end, several approaches have been proposed among them is the use of circulators, which are a 3-port devices that only allow unidirectional wave propagation as opposed to power splitters. This functionality is achieved by breaking the Lorentz time-reversal symmetry, which is satisfied in any linear passive time-invariant system [1, 3]. In RF and microwave circuits, circulators have conventionally been implemented using ferromagnetic materials, biased by magnets. This resulted in heavy and bulky devices. In addition, ferromagnetic materials are hard to integrate with modern IC fabrication processes.

To alleviate the use of magnets and ferromagnetic materials, several techniques have been suggested, such as using active transistors [6,7] and non-linear resonators [16]. Unfortunately, those approaches did not find their way to commercial wireless systems. Since, the former suffered from poor noise figure and linearity, while in the latter case the non-reciprocity is dependant on the input power, and it only works for a limited range. In the aforementioned techniques, the non-reciprocity has been realized by violating either the passivity or the linearity condition. Recently, the use of time variance has gathered a great deal of interest, since theoretically it can yield linear and noise-free devices. In literature, the time variance is realized through the Spatial-Temporal Modulation (STM) of material properties, such as conductivity [38–41] or permittivity [9, 21, 22, 35]. The term spatial-temporal modulation signifies the use of multiple modulating signals, sinusoidal or square waves, distributed in space. Although circulators that are designed using

conductivity-STM showed high linearity (can handle up to $2--4$ watts of input power), low insertion loss $(2--4\,\text{dB})$, compact size, and their potential to operate at millimeter wave frequencies, they suffered from asymmetry in their S-parameters. This asymmetry makes the circulator prune to antenna impedance mismatch as well as high sensitivity to random variations in clock jitter and synchronization.

In the context of permittivity modulation, Sounas *et. al* [10] introduced the concept of Angular Momentum Biasing (AMB) to realize a dielectric ring metasurface with a unidirectional wave propagation. He illustrated that the degeneracy in the ring's modes can be lifted by modulating its permittivity by a sinusoidal signal along the azimuth direction. Shortly after the introduction of AMB, Estep *et. al* [9] built a RF circulator using three coupled LC resonators connected in a Y topology. The STM-AM biasing was implemented practically via varactors, and a progressive phase of $120°$ is applied to the modulation signals as shown in Fig. 2.1 (a). Although the proposed circulator showed a reverse isolation $(\text{IX} = |S_{31}|\,(\text{dB}))$ more than 50 dB, it had the following drawbacks; first, the circulator performance was extremely sensitive to the loaded quality factor (Q_l), which makes it difficult to match to 50 ohms. Second, the series LC resonators boost the voltage across the varactor deteriorating the circulator power handling. Third, a strong higher order intermodulation (IM) products were generated in the structure. Fourth, the 20-dB IX FBW was limitted to 5-7%.

Remarkably, Kord *et. al* presented a few circulator designs that circumvent one or more of the above mentioned drawbacks [21,22,35]. In [21], a circulator composed of three first order bandstop resontors connected in a Δ topology is proposed to tackle the issue of low power handling and high sensitivity to Q_l. Although the devised circulator was less complicated compared to [9] and showed a much better insertion loss, it still suffered from the generation of strong higher order IM products. In [22], two Δ-based circulators with a $180°$ phase shift between their modulating signals are combined to realize a differential based circulator. Thanks to the odd symmetry that the structure exhibits with respect to the IM products, the first order IM product was reduced by 18 dB as compared to a single ended circulator. In both previous designs, the 20-dB IX FBW did not exceed

5-7%, which hinders their usage in practical application, where the input signal occupies a finite bandwidth. In [35], Kord *et. al* suggested the use of a broadband matching network to widen the isolation response. Although he was able to extend the 20-dB IX FBW to 13.8 %, the proposed design suffered from high insertion loss, despite using differential topology, of $5\,\mathrm{dB}$.
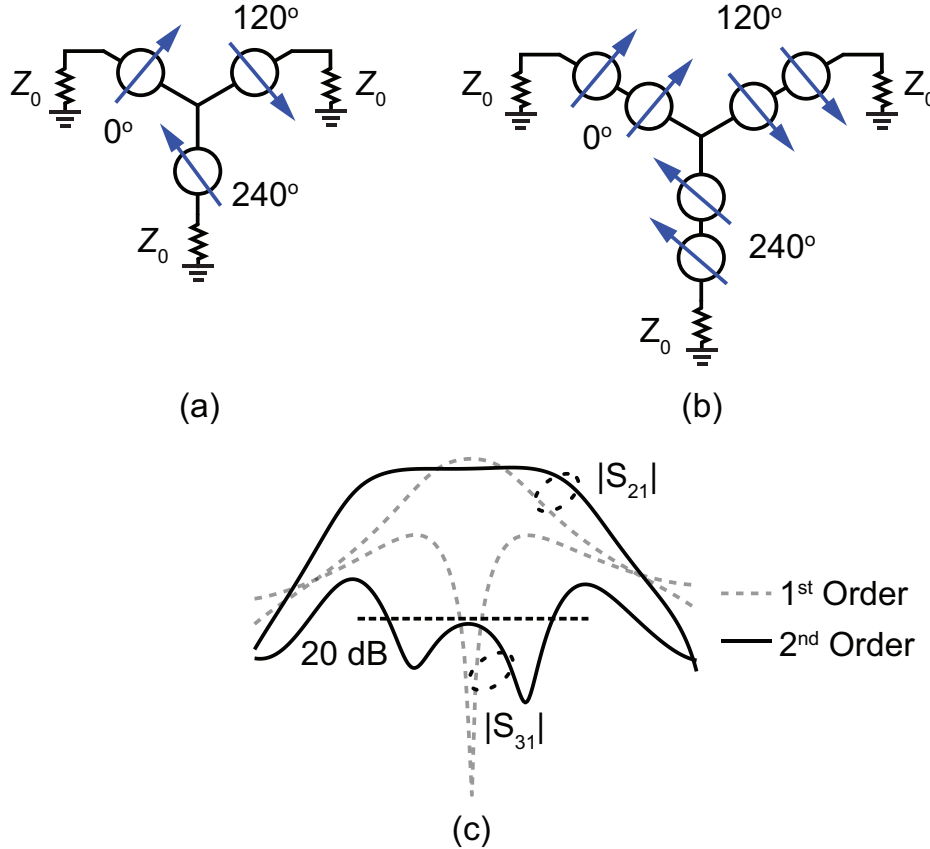
Figure 2.1: Conceptual illustration for magnetless circulator based on STM-AMB of (a) first order and (b) proposed second order resonators, and (c) their transmission and reverse isolation responses. White circles represent a resonant LC circuit.

Recently, Wu *et. al* have introduced the concept of higher order STM [42,43] to build a magnet-free non-reciprocal isolating filter. In [42], it was shown analytically and experimentally that cascading two or more time varying resonators can result in a non-reciprocal isolator with a filter-like characteristics of low insertion loss ($1.5\,\mathrm{dB}$) and deep isolation ($> 20\,\mathrm{dB}$) over the filter passband ($170 - -220\,\mathrm{MHz}$). Notice that since the aim of their work is the implementation of a magnet-free isolator, the applied spatio-temporal modu-

lation can be considered linear rather than angular. Inspired by this idea, we presented a magnet-free circulator based on STM-AM of second order passband resonator as shown in Fig. 2.1 (b) [11]. The reported results were based on heuristic simulations without either clear design methodology or experimental verification. Fig. 2.1 (c) compares the transmission and isolation responses of STM-AM of first and second order resonators. It is clear that a wider passband and 20-dB IX FBW can be attained with the use of second order resonators on the expense of a little increase in insertion loss ($\approx 0.5\,\text{dB}$). Although not shown for clarity but similar argument can be made about having a flat group delay over a wider frequency range, which is an important feature to avoid signal distortion and to relax the linearity conditions in PA design. Furthermore, unlike previous reports that lack any information about the synthesis procedure, in this chapter we show that the static circulator characteristics are fully determined by its back-to-back 2 port filter response. Based on that, we designed a three-fold symmetric circulator demonstrating a 20-dB IX FBW of 15.4 %, which, to our best knowledge, is one of the largest IX BW to date using STM AM biasing.

This chapter is organized as follows: Section II first illustrates the analysis and design of a Y topology to yield the static wideband response. Then, the modulated circulator response is optimized via parametric studies of the modulation parameters. Section III discusses the circulator implementation using off-the-shelf lumped elements. In addition, small and large signal measurements are demonstrated. Finally, Section IV concludes and summarizes the chapter.

2.2 Analysis and Design

In this section, first we explain the rationale behind the proposed design procedure. Then, we analytically derive the S-parameters of a 3-port Y-network and a 2-port symmetric network. Based on that, we show a step-by-step procedure to synthesize a Y-network to provide the circulator static response. After that, we perform a parametric study to reach the optimum circulator modulated response. Finally, we present design guidelines for the design of a circulator with arbitrarily 20-dB IX FBW.
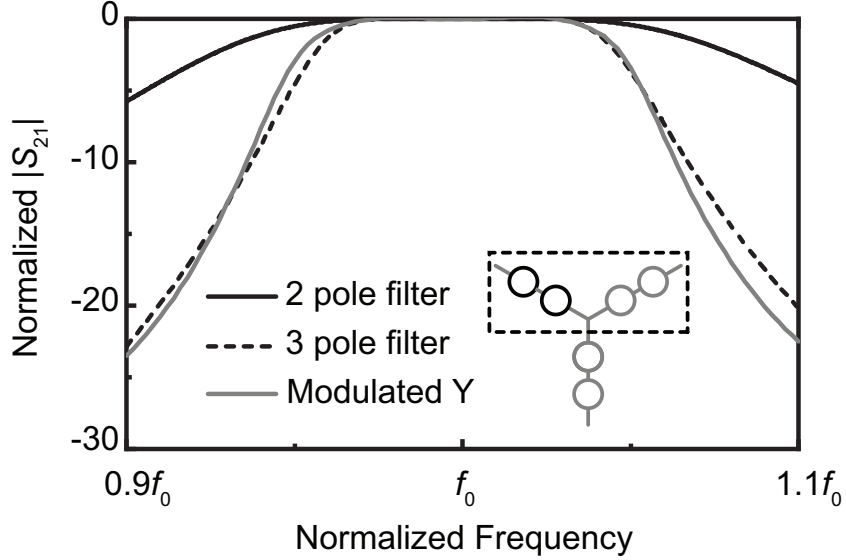
Figure 2.2: Normalized transmission $|S_{21}|$ of the optimized modulated Y, and static 2- and 3-pole filter reported in [11].

2.2.1 Design Methodology Rationale

In our early findings [11], we have demonstrated, via simulation results, that about $8\,\%$ 15-dB IX FBW can be achieved using second order STM-AMB LC resonators connected in a Y. To reach that result, we have hypothesized that the circulator transmission and isolation properties can be set primarily based on the static passband characteristics of one branch of the Y topology, which is a 2-pole filter response. Based on that, we have started the design procedure with a static 2-pole 0.01-dB Chebyshev filter with equal ripple FBW of $5\,\%$. Then, a three-fold symmetric Y is constructed, and the STM-AMB parameters are swept to reach a design that exhibits a good compromise between IL, RL, and IX bandwidth.

Fig. 2.2 compares the optimal circulator response with that of the 2-pole static filter response, which reveals that our initial premise has not been true. Guided by the observation that the circulator passband is narrower and has a sharper roll-off, this suggests that its response is of a higher filter order. By noticing that one arm of the Y-topology constitutes a 3-pole filter (a higher order), we have designed a 3-pole 0.01-dB Chebyshev filter with the same ripple FBW of $5\,\%$. Interestingly, its response is very close to the optimal modulated response as depicted in Fig. 2.2.

26

$$(a)$$

$$(b)$$
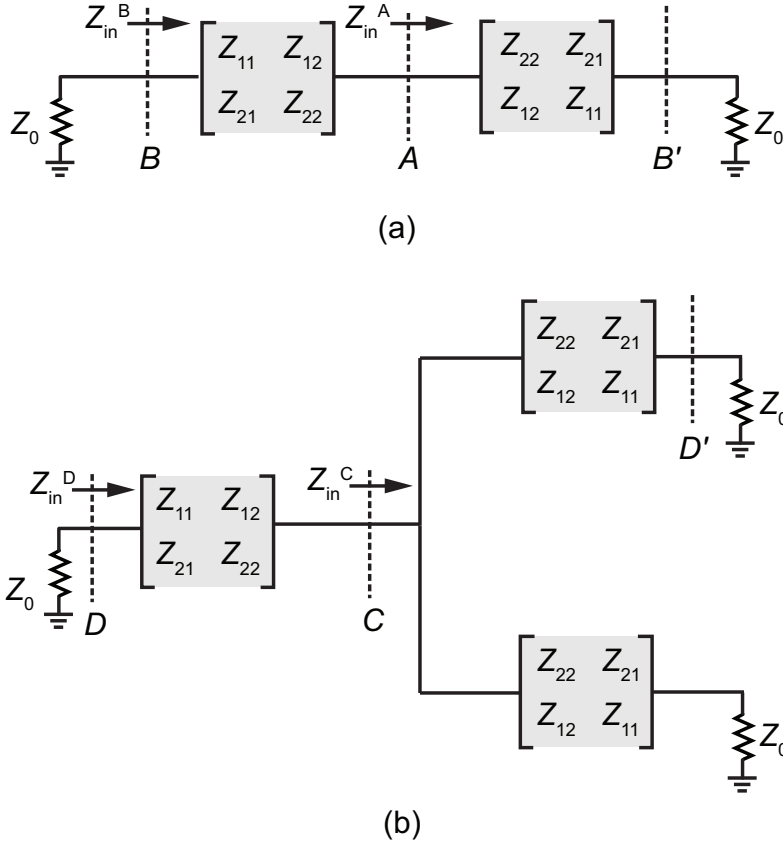
Figure 2.3: An illustration showing a generic Z matrix representation of (a) a 2-port back-to-back network and (b) a Y 3-port network.

This observation has inspired us to divide the circulator design process into two parts. First, the circulator *static* 3 port network response is synthesized based on the desired passband characteristics. In that aspect, we demonstrate, as will be discussed later, that the well-established microwave filter design techniques can easily be incorporated to yield the desired response. Second, the circulator *modulated* non-reciprocal characteristics can be achieved by choosing the proper STM-AMB parameters that achieve the desired isolation level.

2.2.2 Two- and Three-Port Networks

In this subsection, we analytically study the transmission characteristics of a 3-port Y network and a 2-port network. A symmetrical two-port network can be modeled as two identical branches stacked back-to-back, as shown in Fig. 2.3 (a). For a general illustration, each branch is defined using a **Z**-matrix. Here, the diagonal elements of the **Z**-matrix are

swapped due to the back-to-back configuration. Apparently, a Y-topology junction can be produced by adding one more branch based on the 2-port network, as illustrated in Fig. 2.3 (b).

For the two-port network of Fig. 2.3 (a), the input impedance Z_{in}^A at the reference plane A can be derived as

$$Z_{in}^A = Z_{22} - \frac{Z_{21}Z_{12}}{Z_{11} + Z_0}. \tag{2.1}$$

Here, we assume the network to be lossless and reciprocal for simplicity. As such, $Z_{ij}(i, j = 1, 2)$ of the $\mathbf{Z}$-matrix only have pure imaginary parts and can be rewritten as $Z_{11} = jX_{11}$, $Z_{21} = Z_{12} = jX_{21}$, and $Z_{22} = jX_{22}$, where X_{11}, X_{21}, and X_{22} are frequency-dependent variables. Therefore, (2.1) can be reduced to

$$Z_{in}^A = jX_{22} + \frac{X_{21}^2}{Z_0 + jX_{11}}. \tag{2.2}$$

The impedance Z_{in}^A can be considered as the loading to the left-hand branch. Hence, the input impedance Z_{in}^B at reference plane B is

$$Z_{in}^B = jX_{11} + \frac{X_{21}^2}{Z_{in}^A + X_{22}}. \tag{2.3}$$

Substituting (2.2) into (2.3) yields

$$Z_{in}^B = jX_{11} + \frac{X_{21}^2}{\dfrac{X_{21}^2}{Z_0 + jX_{11}} + j2X_{22}}. \tag{2.4}$$

From Z_{in}^B, the input reflection coefficient can be derived.

$$\begin{aligned} |\, \Gamma_{in}^B \,|^2 = |S_{11}^B|^2 = &\, |\, \frac{Z_{in}^B - Z_0}{Z_{in}^B + Z_0} \,|^2 \\ = &\, 1 - \frac{X_{21}^4 Z_0^2}{[(X_{11}X_{22} - X_{22}^2)^2 + X_{22}^2 Z_0^2][X_{11}^2 + Z_0^2]}. \end{aligned} \tag{2.5}$$

A lossless 2-port network has the following unitary condition for power conservation.

$$|S_{11}|^2 + |S_{21}|^2 = 1. \tag{2.6}$$

Taking (2.5) to (2.6) yields the transmission coefficient $|S_{21}^{BB'}|$ for the two-port network.

$$| S_{21}^{BB'} |^2 = \frac{X_{21}^4 Z_0^2}{[(X_{11}X_{22} - X_{22}^2)^2 + X_{22}^2 Z_0^2][X_{11}^2 + Z_0^2]}. \tag{2.7}$$

The Y-topology junction of Fig. 2.3 (b) can be analyzed in a similar way. The input impedance Z_{in}^C at reference plane C is $Z_{in}^C = 0.5 * Z_{in}^A$ and Z_{in}^D at reference plane D is

$$Z_{in}^D = jX_{11} + \frac{X_{21}^2}{j1.5X_{22} + \dfrac{0.5X_{21}^2}{Z_0 + jX_{11}}}. \tag{2.8}$$

Accordingly, the reflection coefficient at reference plane D can be derived as

$$\begin{aligned} | \Gamma_{in}^D |^2 &= | S_{11}^D |^2 \\ &= 1 - \frac{8X_{21}^4 Z_0^2}{9[(X_{11}X_{22} - X_{22}^2)^2 + X_{22}^2 Z_0^2][X_{11}^2 + Z_0^2]}. \end{aligned} \tag{2.9}$$

For a lossless and symmetric 3-port network, the unitary condition becomes

$$2 \mid S_{21} \mid^2 + \mid S_{11} \mid^2 = 1. \tag{2.10}$$

Hence, the transmission coefficient of the 3-port Y-junction is

$$| S_{21}^{DD'} |^2 = \frac{4}{9} \frac{X_{21}^4 Z_0^2}{[(X_{11}X_{22} - X_{22}^2)^2 + X_{22}^2 Z_0^2][X_{11}^2 + Z_0^2]}. \tag{2.11}$$

Interestingly, (2.7) and (2.11) reveal that the transmission coefficient of the three-port Y-network and that of a 2-port filter have the following relation.

$$| S_{21}^{DD'} |^2 = \frac{4}{9} | S_{21}^{BB'} |^2, \tag{2.12}$$

or equivalently in decibels,

$$| S_{21}^{DD'} | \text{ (dB)} = -3.522 + | S_{21}^{BB'} | \text{ (dB)}. \tag{2.13}$$

The significance of (2.12) and (2.13) is that apart from a constant factor, the Y-network transmission response is the same as that of a symmetric back-to-back 2-port network. As such, the circuit design of a static Y-network, which is the starting point in the circulator design flow, can start from a conventional symmetrical two-port network.

2.2.3 Y-Network Static Response Synthesis

In the previous section, we concluded that in order to design a Y-network, one should start with a symmetric 2-port network.In this subsection, we demonstrate a step-by-step method to synthesize a Y-network utilizing the well-established 2-port filter design techniques. As an illustrative example, we consider a 3-pole filter whose lowpass prototype is shown in Fig. 2.4 (a). Fig. 2.4 (b) shows the filter implementation using K-inverters and inductors, where the load and source impedance are scaled to Z_0. Here, the central inductor has twice the inductance of the side inductors to reserve two identical branches stacked back-to-back. The K-inverters represent the filtering coupling and can be expressed as

$$
\begin{aligned}
K_{0,1} = K_{3,4} &= \sqrt{\frac{Z_0 L_{LP}}{g_0 g_1}}, \\
K_{1,2} = K_{2,3} &= \sqrt{\frac{L_{LP} 2 L_{LP}}{g_1 g_2}}.
\end{aligned}
\tag{2.14}
$$

By applying the following lowpass-to-bandpass transformation, a third-order bandpass filter can be modeled as shown in Fig. 2.4 (c).

$$
L_{BP} = \frac{L_{LP}}{FBW \omega_0} \quad \text{and} \quad C_{BP} = \frac{FBW}{\omega_0 L_{LP}},
\tag{2.15}
$$

where FBW is the fractional bandwidth of the passband and ω_0 is the passband center angular frequency. It is worth mentioning that the K-inverter values of (2.14) can also be described in terms of the bandpass filter inductance (L_{BP}) by simply substituting (2.15) into (2.14). Lastly, the three-port Y-junction network can be constructed by simply adding one more branch to the center of the two-port network, as shown in Fig. 2.4 (d).

Fig. 2.5 compares the transmission and reflection profiles of a symmetrical two-port filter and a three-port Y-junction network. $K_{01} = K_{34} = 26.5, K_{12} = K_{23} = 14, L_{BP} = 17.8\,\text{nH}$,and $C_{BP} = 5.7\,\text{pF}$ are chosen for a Butterworth third-order bandpass filter of $FBW = 25\%$ and $f_0 = 500\,\text{MHz}$. The concluded relation (2.13) is also examined and confirmed by the close coherence among the transmission profiles. The Y-network has a passband insertion loss of $3.5\,\text{dB}$, which can be divided into a 3-dB loss due to power splitting and a 0.5-dB loss due to mismatch.
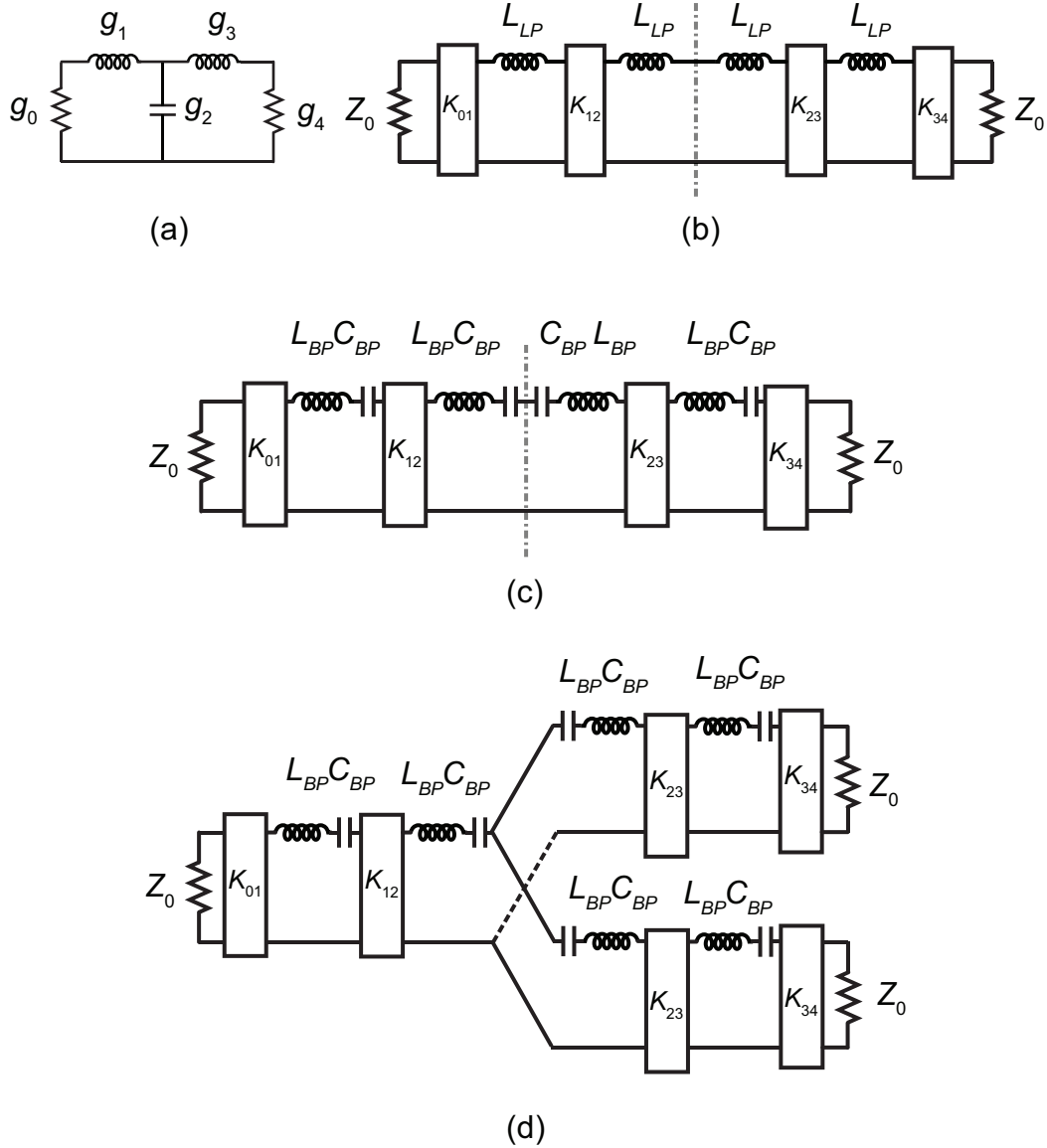
Figure 2.4: Constructing Symmetric Y Network: (a) normalized 3-order LPF prototype, (b) De-normalized LPF with K-inverter implementation, (c) 2-port BPF transformation, and (d) 3-port Y-network.

It should be noted that the concluded relation in (2.13) applies to arbitrary-order filter and Y-junction networks. In particular, a Y-junction network whose branch circuit has a resonator order of N can be synthesized from a $(2N-1)$-order two-port filter network. In this work, however, we focus on $N = 2$ for illustration simplicity.
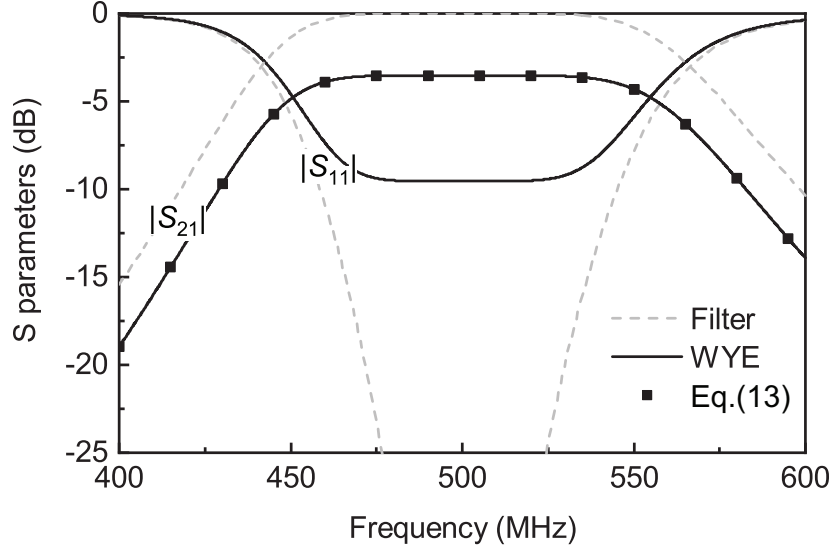
Figure 2.5: S-parameters of Y- and 2-port networks.

2.2.4 Modulated Response

In this subsection, STM with an incremental modulation phase of $120°$ is applied to the Y-junction network to obtain a wideband circulator isolation response. The equivalent circuit model of the proposed circulator is shown in Fig. 2.6. The capacitance of each resonator is modulated as

$$C_i(t) = C_{BP}\left[1 + \xi \cos\left(\omega_m t + (i-1)\, 120°\right)\right], \tag{2.16}$$

where $i = 1, 2, 3$. C_{BP} is the static bandpass capacitance, ω_m is the modulation angular frequency, and ξ is the modulation index.

In this work, we assume that the resonators in each branch have the same modulation parameters f_m and ξ. This assumption is made to facilitate the practical implementation of a time-varying capacitor.

To reach an optimum circulator response, we conduct a parametric study of the effect of each modulation parameter on the circulator main metrics, namely the insertion loss $|S_{21}|$, return loss $|S_{11}|$, and isolation $|S_{31}|$. The study is performed in ADS with the help of harmonic balance simulation tool to capture the harmonics created due to the STM-AMB. When either the modulation frequency or index is set to zero, the circuit response corresponds to the static response shown in Fig. 2.4 (e). Fig. 2.7 summarizes the
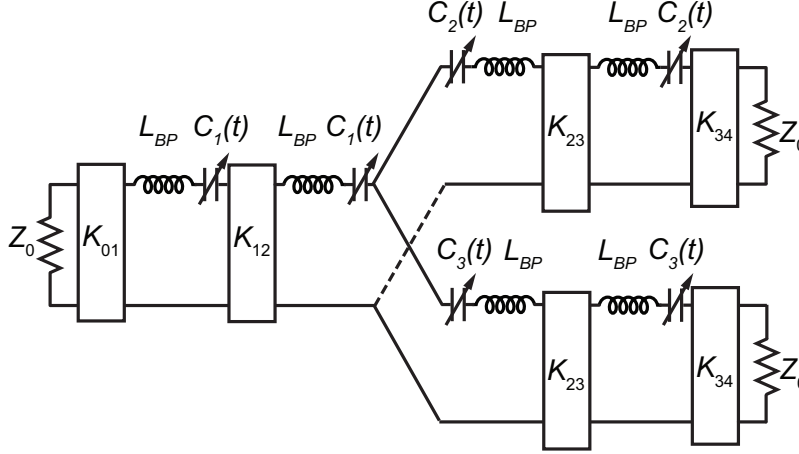
Figure 2.6: Y based circulator with time varying capacitor.

parameteric study results, where each row corresponds to a circulator metric, whereas the first two columns represent the parameter under study. In addition, the third column depicts the optimum response concluded from the study, which is also highlighted in the figures of the first two columns by a black-dashed lines.

First, we investigate the effect of the modulation frequency f_m (to have a more general descriptive figure we normalize it to our frequency of design i.e. f_{RF}=500 MHz) for a fixed modulation index ξ=0.34. From the isolation response shown in Fig. 2.7 (c), one can observe two locations with deep isolation levels around our target frequency. The first location is around $f_m/f_{RF} \approx 0.1$, while the the second is around $f_m/f_{RF} \approx 0.2$. Although the return loss in Fig. 2.7 (b) illustrates that the first location yields a better matching condition, this location suffers from a narrow passband response. This is more apparent from the insertion loss plot shown in Fig. 2.7 (a), where the circulator passband has the following trend; it is almost constant for $f_m/f_{RF} > 0.22$. Then, it slightly increases over the short range $0.15 < f_m/f_{RF} < 0.22$. With further decrease in the normalized modulation frequency, the passband diminishes to reach its minimum value at $f_m/f_{RF} \approx$ 0.05. For this reason, we choose the second location as the optimum f_m/f_{RF} value.

Second, we study the effect of modulation index under a constant f_m/f_{RF} value of 0.22. Fig. 2.7 (f) shows that the isolation is maximum around $\xi = 0.34$. Similar to the previous case, there is a trade off between enhancing the return loss and the circulator passband. Increasing ξ improves the return loss but on the expense of reducing the

33

circulator passband. A good compromise is reached at $\xi = 0.34$.

Based on the above studies, the modulation frequency and index are set to be f_m=112 MHz and ξ=0.34, respectively. The corresponding circulator behaviour is depicted in the last column of Fig. 2.7, where the circulator exhibits a flat insertion loss of 3.42 dB across the frequency range from $491 - 536.8$ MHz, a return loss of 8 dB, and a 20-dB IX FBW of 18.7%.

2.2.5 Design Guidelines

From a designer perspective, it would be beneficial to know in advance which filter 3-dB FBW to use in order to achieve certain 20-dB IX FBW. To provide an answer to this question, we have repeated our design methodology for different 3-dB FBW, and have recorded the corresponding 20-dB IX FBW of the optimum circulator that has been found through the previously discussed parametric studies. Fig. 2.8 summarizes the output of this study. From the figure, one can observe that the 20-dB IX FBW increases monotonically with the static filter 3-dB FBW. Using curve fitting, this increase can be expressed by using by a first order polynomial, which is expressed on the figure. Moreover, as the 3-dB FBW increases, the modulation parameters needed to achieve a 20-dB IX FBW also increase. This observation can be considered the limiting factor to realizing extremely large ($> 20\%$) 20-dB IX FBW. Furthermore, throughout this study we have assumed a Butterworth filter, yet for other type of filters, such as Chebyshev filters, a similar procedure can be developed that relates the 20-dB IX FBW to the different ripple levels and FBW.

In summary, given a desired 20-dB IX FBW, the proposed design guidelines are as follows:

Step 1: Find the corresponding 3-dB FBW of the 2-port Butterworth filter using Fig. 2.8.

Step 2: Apply equations (2.14) and (2.15) to implement a BPF using K-inverters.

Step 3: Construct a three-fold symmetric Y-network, which is achieved by first scaling the inductor/capacitor of the second resonator by a factor of two/half, respectively. Then, connecting an identical third branch at the axis of symmetry.
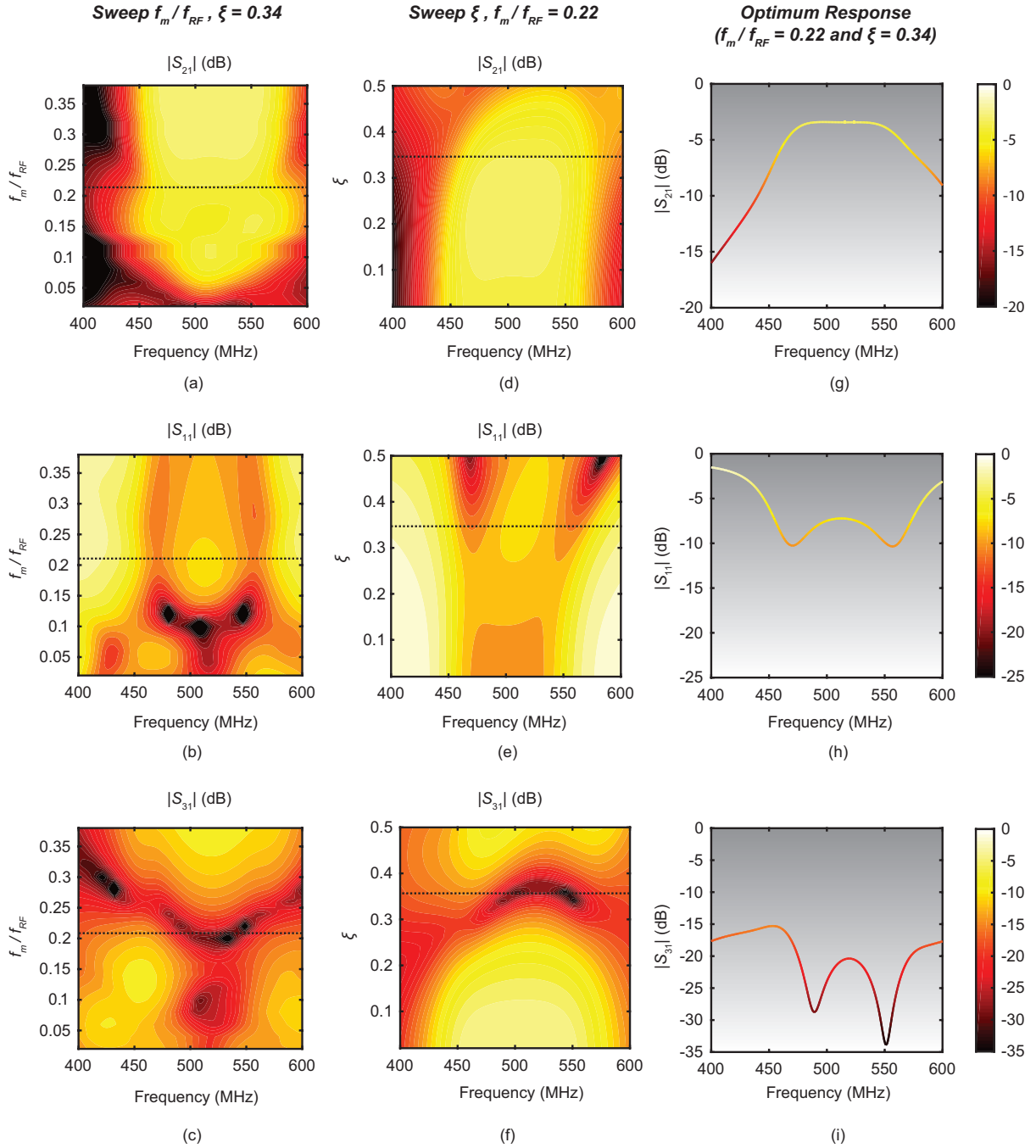
Figure 2.7: Parameteric study of the proposed second order STM-AM biased circulator (the dashed lines corresponds to the nominal response). First column shows the effect of different modulation frequency f_m/f_{RF} under constant modulation index of $\xi = 0.34$ on the circulator (a) $|S_{21}|$, (b) $|S_{11}|$, and (c) $|S_{31}|$. Similarly, the second column (d)−(f) illustrates the effect of varying the modulation index ξ for a fixed modulation frequency $f_m/f_{RF} = 0.22$ on the previously mentioned circulator parameters, respectively. The nominal circulator $|S_{21}|$, $|S_{11}|$, and $|S_{31}|$ responses are highlighted in the third column (g)−(i), respectively.

35
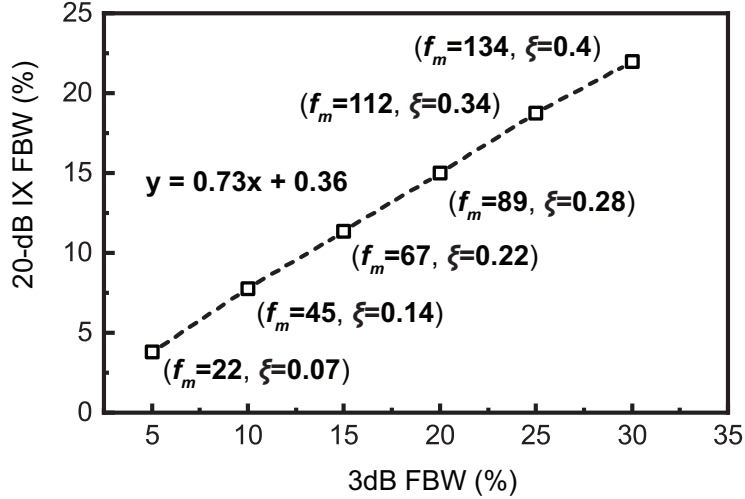
Figure 2.8: The achievable 20-dB IX FBW of different static 3-dB FBW.

Step 4: Replace all static capacitors in the network with time-varying capacitors as described by (2.16).

Step 5: Sweep the modulation parameters (f_m and ξ) until an optimum response is reached. An initial estimate can be deduced from the values given in Fig. 2.8.

2.3   Experimental Validation

In this section, we first discuss the realization of our proposed second order STM-AM biased circulator using off-the-shelf lumped components. Then, we carry out scattering parameters, spectrum, and linearity measurements.

2.3.1   Practical Implementation

By consulting Fig. 2.8, we select a Butterworth filter with a 3-dB BW of 125 MHz (25% at $f_0 = 500\,\mathrm{MHz}$) targeting a 20-dB IX FBW of around 18%. The corresponding modulation parameters are $f_m = 112\,\mathrm{MHz}$ and $\xi = 0.34$. Fig. 2.9 summarizes the steps taken to transform the ideal circuit into a practical one. First, we start by designing a circuit that achieves the required coupling coefficients (calculated in Section 2.2.3). It is shown in [44] that the K-inverters controlling the coupling between resonators can be approximated by a capacitive or an inductive T-network, whereas those controlling the coupling to external ports can be approximated with either a capacitive or inductive dividers/transformers.

(a)

(b)

(c)
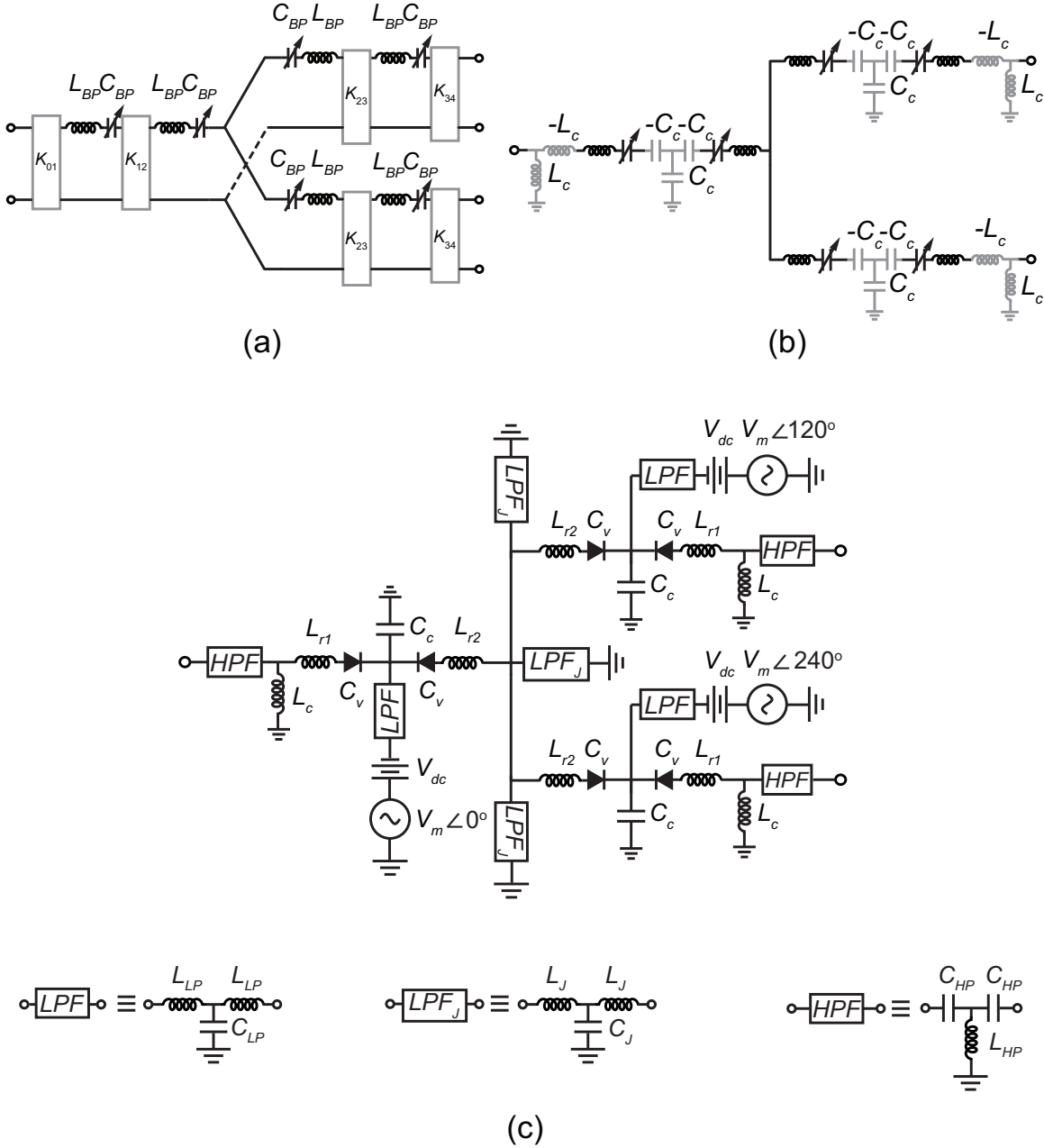
Figure 2.9: Evolution of practical circuit:(a) ideal circuit, (b) K-inverter implementation with lumped components, (c) STM-AMB realization using reversely-biased varactors along with LPF and HPF filters needed to isolate RF and Fm signals.

As illustrated in Fig. 2.9 (b), we select a capacitive T-network and an inductive divider. The reason behind that will become clear shortly as we discuss the practical implementation of a time-varying capacitor. It should be noted that, the negative capacitance and inductance associated with the above structures are combined with those of the main

series LC resonator to give equivalently a positive value.

Next, the ideal time varying capacitors are replaced by a varactor as shown in Fig. 2.9(c). The desired static capacitance value C_{dc} is achieved by reversely biasing the varactor with a dc voltage V_{dc}. The required V_{dc} can be extracted from the C$-$V curve provided in the data-sheet [45]. The choice of a capacitive, instead of an inductive, T-network is to allow V_{dc} to bias both varactors. Moreover, the external coupling inductor L_c as well as the low pass filter LPF_J provide a path for V_{dc} to ground. In conjunction with the V_{dc}, a sinusoidal signal with amplitude V_m and frequency f_m is provided in order to modulate the resonators.

A practical aspect to consider is the prevention of the leakage of the modulating signal to the RF ports and vice versa. This is achieved by placing a third-order high-pass filter at the RF port, and a third-order low pass filter at the modulating source, shown in Fig. 2.9 (c). It is worth mentioning that although the filter lumped component values are initially chosen based on classical microwave filter design techniques, fine tuning is required to account for the loading effect of the equivalent impedance of the other circulator constitutive components.

The circulator layout is carried out on a Rogers 5880 substrate with a thickness of 20 mil and relative permittivity of 2.2. Post-layout simulation is carried out in ADS momentum to account for all the parasitics in the layout. The parasitics of the varactors, such as the series contact resistance and the packaging parasitics, are included in the simulations. Table 2.1 summarizes the circulator main design parameters, the finalized component values, and their corresponding vendor part number.

Table 2.1: Summary of circulator design parameters

Parameters		Value	Part #
Ideal Filter	f_0	500 MHz	–
	BW_{3dB}	125 MHz	–
	L_r	17.8 nH	–
	C_r	5.7 pF	–
	$K_{01}\&K_{34}$	26.5	–
	$K_{12}\&K_{23}$	14	–
Modulation	f_m	112 MHz	–
	ξ	0.34	–
	V_m	2.6 V	–
Implementation	L_{r1}	10.2 nH	0807SQ-10N (Coilcraft)
	L_{r2}	17 nH	0807SQ-17N (Coilcraft)
	C_v	6 pF	SMV1234 (Skyworks)
	C_c	15 pF	0603N150AW251 (PPI)
	L_c	14.7 nH	0908SQ14N (Coilcraft)
	C_{LP}	47 pF	0603N360FW251 (PPI)
	L_{LP}	47 nH	0805HP-47N (Coilcraft)
	C_J	36 pF	0603N470FW251 (PPI)
	L_J	180 pH	2222SQ-181 (Coilcraft)
	C_{HP}	8.2 pF	0603N8R2AW251 (PPI)
	L_{HP}	14.7 nH	0908SQ14N (Coilcraft)

2.3.2 Results and Discussion

The fabricated and assembled PCB is shown in Fig. 2.10 (a), which occupies a total area of 53 mm × 45 mm. Fig. 2.10 (b) shows the measurement setup. The circulator small signal S-parameters are measured using the set-up depicted in Fig. 2.11 (a), which is comprised of a 4 port VNA (Agilent E5071A), a three-channel power source (Rigol DP832), 3 bias-tees, and two arbitrary function generators (Rigol DG5252). Figures 2.11(b)−(d) illustrate the circulator measured and simulated responses in both static and modulated cases.

First, the circulator static behaviour is investigated by connecting the dc port of the bias-tees to a dc power supply and terminating their high frequency port with a 50 Ω load. Fig. 2.11 (b) depicts the response for a dc bias voltage of $V_{dc} = 0.95$ V, where at 500 MHz,
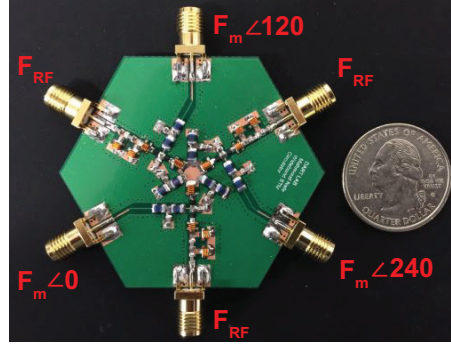
(a)
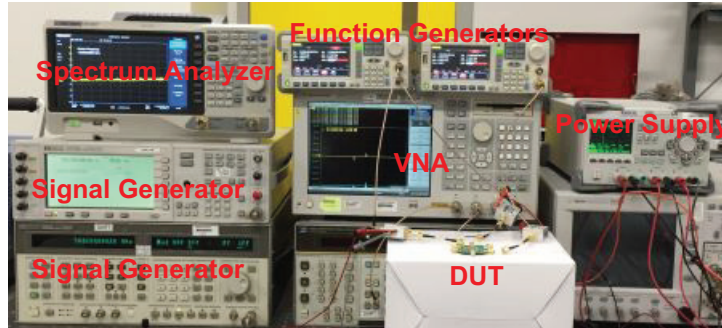
(b)

Figure 2.10: Photograph of (a) fabricated PCB and (b) measurement test bench.

the circuit shows an insertion loss of 5 dB and a return loss of 9.95 dB.

Second, the circulator modulated response is studied, where a precise phase difference of 120° is set between the modulating signals by phase locking both function generators to the same reference clock as shown in Fig. 2.11 (a). The circulator non-reciprocal S-parameters for modulation frequency of f_m=110 MHz and peak amplitude of $V_{ac} = 2.7$ V is depicted in Fig. 2.11 (c).

From the figure, it is clear that the modulated response has second order filter-like behavior with a flat passband, and two distinct resonance peaks in both return loss and reverse isolation. The circulator demonstrates a minimum insertion loss of 4 dB at 500 MHz, and is better than 7 dB across the circulator passband. In addition, the circulator is well-matched with a return loss value of 11.5 dB at 500 MHz. The isolation exceeds 20 dB across the frequency range from 467 MHz to 542.8 MHz, and thus achieving a 20-dB IX FBW of 15.4 %. Moreover, the transmission phase, depicted in Fig. 2.11 (d), shows that the circulator exhibits a linear phase response across the frequency range
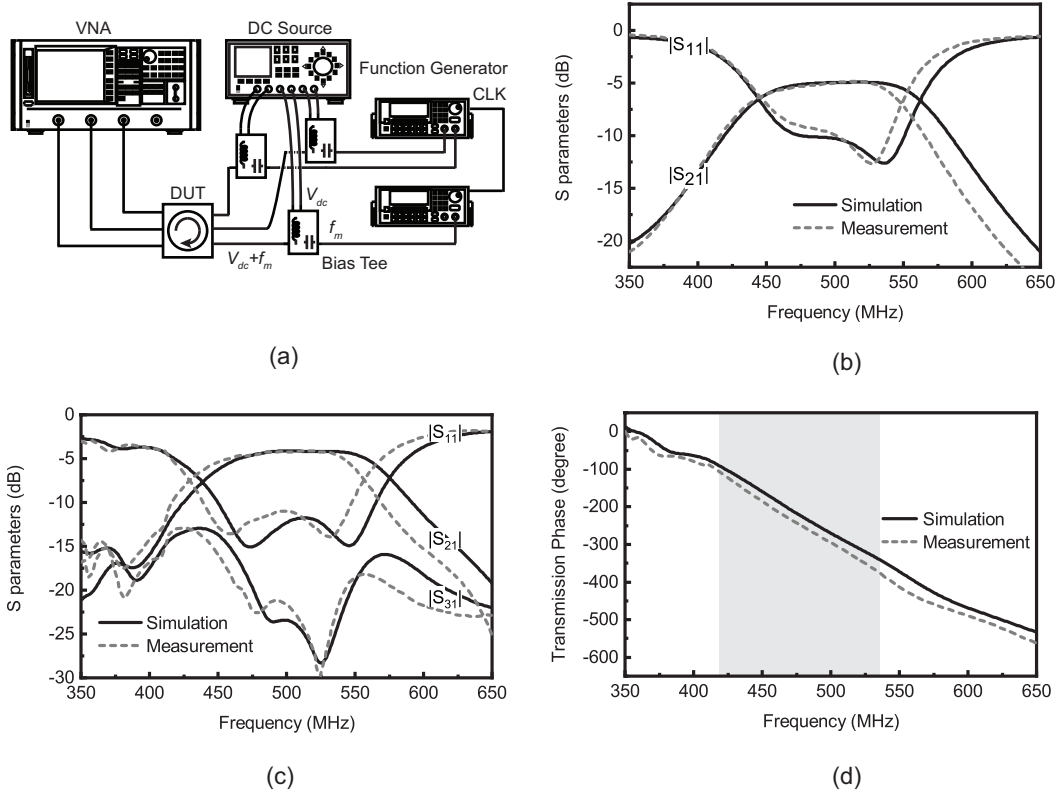
Figure 2.11: Small signal S-parameters: (a) block diagram of measurement setup, (b) static response, (c) modulated response, and (d) transmission phase.

highlighted by the shaded region. This indicates that the circulator shows a flat group delay, which would reduce the distortion due to dispersion in applications where the input RF signal occupies a finite bandwidth.

Apart from a slight frequency shift and a small reduction in the passband bandwith, there is a good match between the simulated and measured data. These deviations may be attributed to either inaccuracy in the parasitic models provided by the vendors for the various lumped components or imperfections in soldering the components. Also, the practical implementation of the circulator experiences an extra loss of 1-1.2 dB compared to that of using ideal components. This extra loss is attributed to the finite unloaded Q of the available lumped components as well as the inclusion of extra components needed for the design of the biasing and filtering circuitry. It is worth mentioning that this loss can significantly be reduced by designing the circulator based on microstrip-line resonators.

The harmonics generated due to the STM-AMB are examined using the setup in
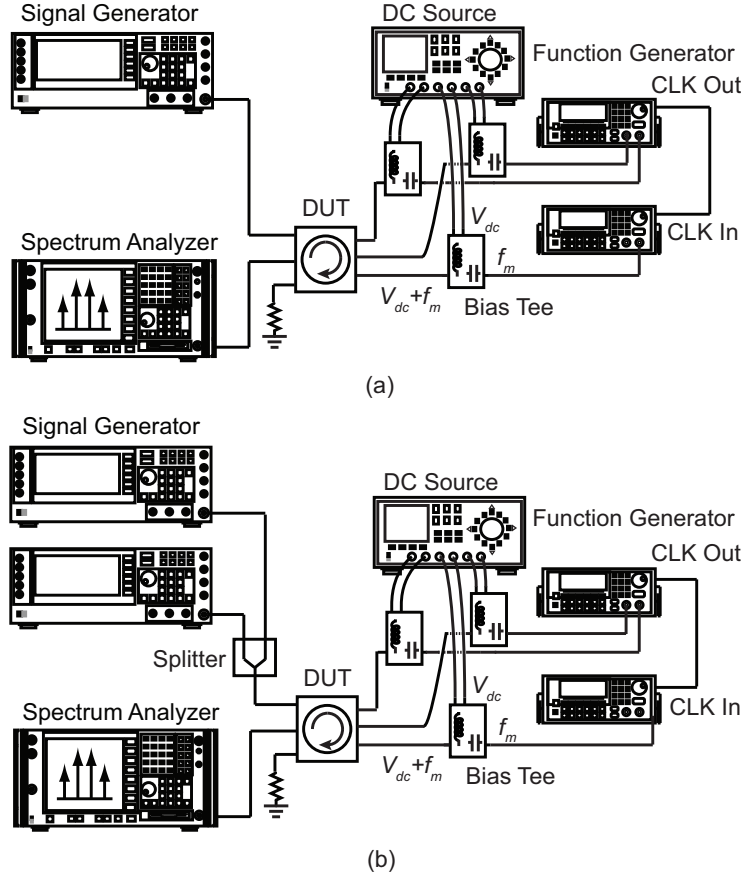
Figure 2.12: Block diagram for measuring: (a) harmonic spectrum and 1-dB compression point, and (b) third order intercept point.

Fig. 2.12 (a). A single tone RF signal at frequency $f_0 = 500\,\text{MHz}$ and power of $P_{in} = -10\,\text{dBm}$ is injected into one port of the circulator using a signal generator (HP8665B). The other two ports are alternatively connected to a spectrum analyzer (Siglent SSA3021X) and a $50\,\Omega$ termination. The corresponding spectra of the signals at the through and isolated ports are depicted in Fig. 2.13.

At $500\,\text{MHz}$, the received power at the through and isolated ports are $P_{Thru} = -14.6\,\text{dBm}$ and $P_{IX} = -35.6\,\text{dBm}$, repectively. These values agree well with the measured insertion loss and isolation. In addition to the carrier tone, there are 4 tones that residue in the spectrum of both ports. The two tones located at frequencies $390\,\text{MHz}$ and $610\,\text{MHz}$ correspond to the first order intermodulation products $f_{RF}\text{-}f_m$ and $f_{RF} + f_m$, which are lower than the carrier tone by $12\,\text{dBc}$ and $11.4\,\text{dBc}$, respectively. The remaining two tones at $440\,\text{MHz}$ and at $550\,\text{MHz}$ are the fourth $4f_m$ and fifth $5f_m$ order harmonics of the mod-
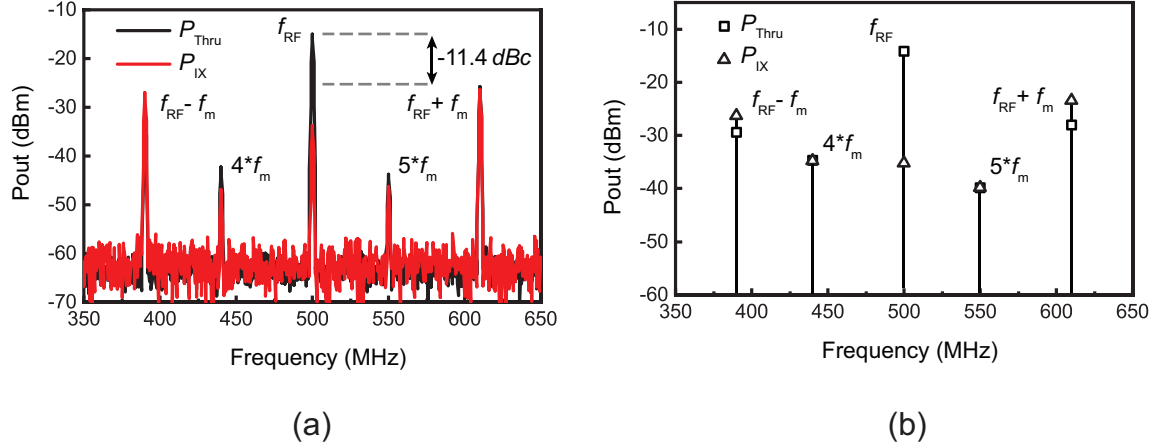
Figure 2.13: Spectrum at through and isolation ports: (a) measured, and (b) simulated.

ulating signal. These tones are independent of the input RF signal, and can be removed digitally from the spectrum.

Next, the circulator power handling is investigated by using single tone and two-tone tests. For the single tone test, the input power is swept using the same setup of Fig. 2.12 (a), while for the two tone test, a splitter is used to combine two tones at 495 MHz and 505 MHz i.e. 5 MHz separation from the circulator center frequency as shown in Fig. 2.12 (b). The simulated and measured data for both tests are depicted in Fig. 2.14. The circulator shows an input 1 dB compression point of P1dB=10 dBm, and an input third order intercept point of IIP3=15 dBm.
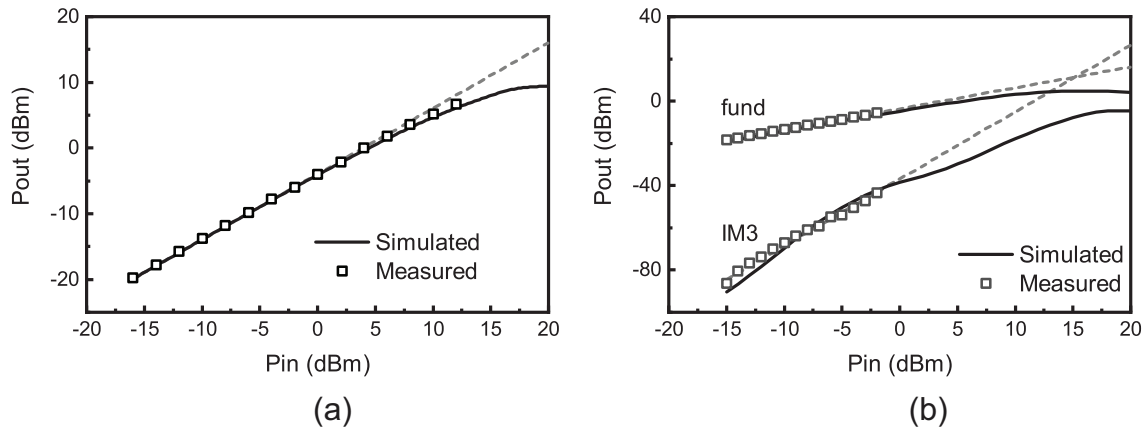
Figure 2.14: Large signal measurements: (a) single-tone, and (b) two-tone

43

2.4 Summary

A summary of the circulator performance in comparison with the state-of-the art magnetic-free circulators based on spatio-temporal angular momentum biasing is listed in Table 2.2. Thanks to using second order coupled resonators, our proposed circulator shows the widest 20-dB IX FBW with acceptable performance in terms of insertion and return losses. It is worth mentioning that while the focus of this work is to improve the 20-dB IX bandwidth, the linearity and power handling of the proposed work can be improved through the use of a differential or N-way circulator topology.

2.5 Acknowledgement

Table 2.2: Summary of state-of-art magnetless circulator based on spatio-temporal modulation angular momentum biasing (STM-AMB)

Metric\Reference	This work	[9]	[46]	[21]	[22]	[35]	[47]
Architecture	SE Y	SE Y	SE Δ	SE Δ	Diff. Δ	BB Diff. Y	Mod. Diff. Y
Resonator order	Second	First	First	First	First	First	First
Technology	SMT	SMT	65nm CMOS	SMT	SMT	SMT	180 nm CMOS
Modulating element	Varactor	Varactor	CMOS Varactor	Varactor	Varactor	Varactor	NMOS Switch
Frequency of operation	500 MHz	130 MHz	100 GHz	1000 MHz	1000 MHz	1000 MHz	915 MHz
f_m/f_{rf} (%)	22	30.8	14.2	19	10	11	11.6
DC bias (V)	0.95	1.1	N/A	19.6	7.3	8	N/A
Modulation Signal (V_{peak})	2.4	1.3	N/A	5.4	1.1	3.1	N/A
20-dB IX BW (%)	15.4	7[*]	13.5[++]	2.4	2.3	13.8	2.4[+]
IX[1](dB)	22	65	47	55	25	29	65[+]
IL[1](dB)	4	9	5.8	3.3	0.78	4.2	4.8[+]
RL[1](dB)	11.5	4	16	10.8	23	11.7	11[+]
IP1dB[1](dBm)	10	3.27[**]	11.2	29	28	N/A	N/A
IIP3[1](dBm)	15	5.7[**]	N/A	33.7	31	N/A	6
First Order IM products (dBc)	-11.4	-14[**]	-16	-11.3	-29	-22	-20
Size (mm^2)	53×45	22×17	N/A[***]	13×11	2×(13×1	22×22	6×6

[1] at center frequency

[*] Deduced from Fig. 12 in [9]

[**] Based on circuit simulation

[***] Unpackaged bare die size is 0.21 mm^2

[+] Using external impedance tuner

[++] Estimated from Fig. 17 in [46]

Chapter 3

Magnetic-free RF Circulators Based on STM of Higher Order Coupled Resonators

In this chapter, we study the behavior of higher order $(n > 2)$ circulators. Moreover, as we increase the order, we examine the relationship between the circulator modulated 20-dB IX FBW and the constitutive static filter 3-dB FBW. Furthermore, we analyze the insertion loss of higher order single ended and differential circulators. Last but not least, we provide a lower limit on the modulation frequency to ensure proper operation.

3.1 Reflection, Transmission, and Isolation Responses of Higher Order STM Based Circulators

In the previous chapter, we have demonstrated that using a 2nd order circulator can result in 2 notches in the $|S_{31}|$ dB (IX) response. Moreover, a wideband 20-dB IX FBW can be achieved by choosing the appropriate 3-dB static filter FBW. Based on that, one might intuitively assume that we can improve the IX response with further increase in the order. Thus, we conduct a comprehensive study on the modulation parameters and compare the circulator response as we increase the order.

Without the loss of generality, we will conduct this study on circulators built in a Y-topology. It is worth mentioning that the circulator's order is determined by the number
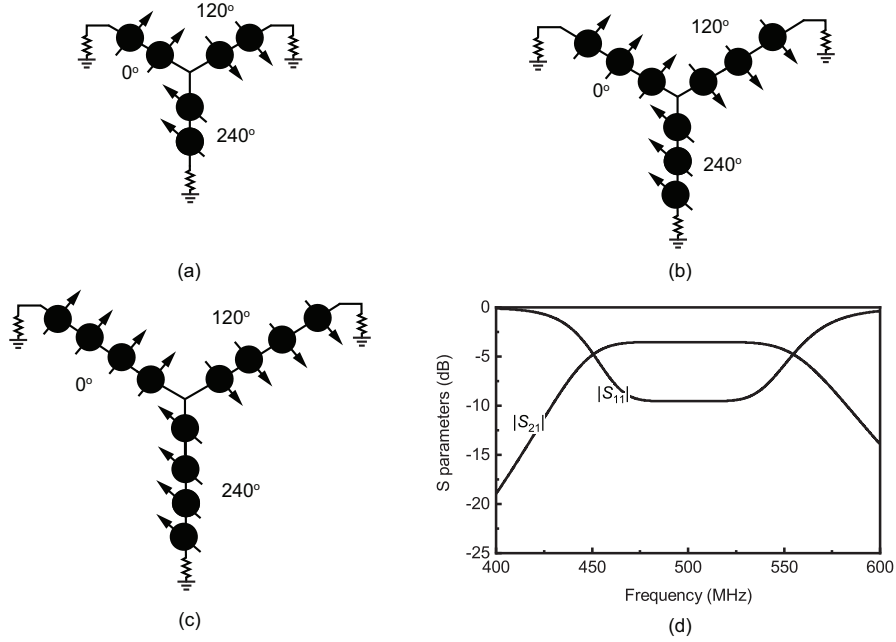
Figure 3.1: Investigated higher order circulators: (a) 2nd, (b) 3rd, (c) 4th, and (d) static response. Here, $|S_{21}| = |S_{31}|$

of resonators in one branch. As explained in the previous chapter, to synthesize a three-fold symmetric Y-network with a circulator order (n), we should start with a static 2-port filter network with order of (2n-1). Thus, for this study a third-, a fifth-, and a seventh-order Butterworth filters are needed for the construction of a 2nd-, a 3rd-, and a 4th-order circulator, respectively. The static response of all filters is designed for $f_0 = 500\,\text{MHz}$ and FBW $= 25\,\%$. Moreover, for simplicity we assume that all resonators located in one branch are modulated with the same modulation parameters, namely the modulation frequency f_m and the modulation depth d_m. Also, a progressive phase shift of 120° is applied to the modulating signals of each branch. Fig. 3.1 depicts the investigated 2nd-, 3rd-, and 4th-order circulators along with the corresponding static response.

To thoroughly study the modulated response of higher order circulators, we perform a 2D nested loop for f_m and d_m. For each circuit, we vary the f_m from 75 MHz to 225 MHz with a step of 25 MHz. For each f_m value, d_m is swept from 0.1 to 0.8. Regardless of the circulator order, we observe that across all f_m values: For $d_m < 0.2$, the non-reciprocity is weak, while for $d_m > 0.5$, the passband is highly attenuated leading to an unacceptable circulator response. Hence, the region of interest is $0.2 < d_m < 0.5$. The results of each

order are individually plotted in the Appendix A.1, herein we focus on comparing the $|S_{11}|$, $|S_{21}|$, and $|S_{31}|$ of each order for the cases of $d_m = 0.4$ and $d_m = 0.5$. These values of d_m are chosen since the overall circulator behavior of all orders shows acceptable levels of matching, insertion loss, and isolation.

In terms of return loss, Fig. 3.2 depicts the $|S_{11}|$ of the different orders. As shown in the figure, the 2nd and 3rd order circulators show two and three reflection zeros in their passband, respectively. On the other hand, this is not the case for the 4th-order. This observation negates the original intuition that the number of poles in the $|S_{11}|$ should match the circulator order. Consequently, for the return loss response, increasing the order beyond 3rd order will have diminishing returns.

Regarding the $|S_{21}|$ depicted in Fig. 3.3, clearly we can observe that increasing the order results in a sharper filter response. Hence, higher order circulators will have the advantage of a higher out-of-band rejection. It should be noted that in this study we have ignored the insertion loss and used ideal components. We will discuss the insertion loss in the next section. Moreover, the $|S_{31}|$ is shown in Fig. 3.4, where it should be noted that for most d_m cases the $|S_{31}|$ is below 20 dB. Moreover, in regards to the number of poles in the isolation response the 2nd order show 2 poles. Meanwhile, the 3rd order shows mostly 2 poles as well with the exception of the case corresponding to the modulation parameters $f_m = 150\,\text{MHz}$ and $d_m = 0.5$. Surprisingly, the 4th order only show 2 poles, which indicates that the isolation behaves in a similar manner as the return loss. Therefore, increasing the order beyond 3rd order will not have a significant improvement in the isolation response.

To sum up, increasing the order has the advantage of giving a sharper circulator roll-off which could be beneficial to attenuate any non-linear effects along the transceiver chain. For the return loss, we did not observe any clear relationship between the number of reflection zeros and the circulator order. In the same manner, the number of poles in the isolation did not increase with the order. This study suggests that a 3rd order circulator would suffice to provide a modulated response with moderate insertion loss, high out-of-band rejection, and good matching and isolation.
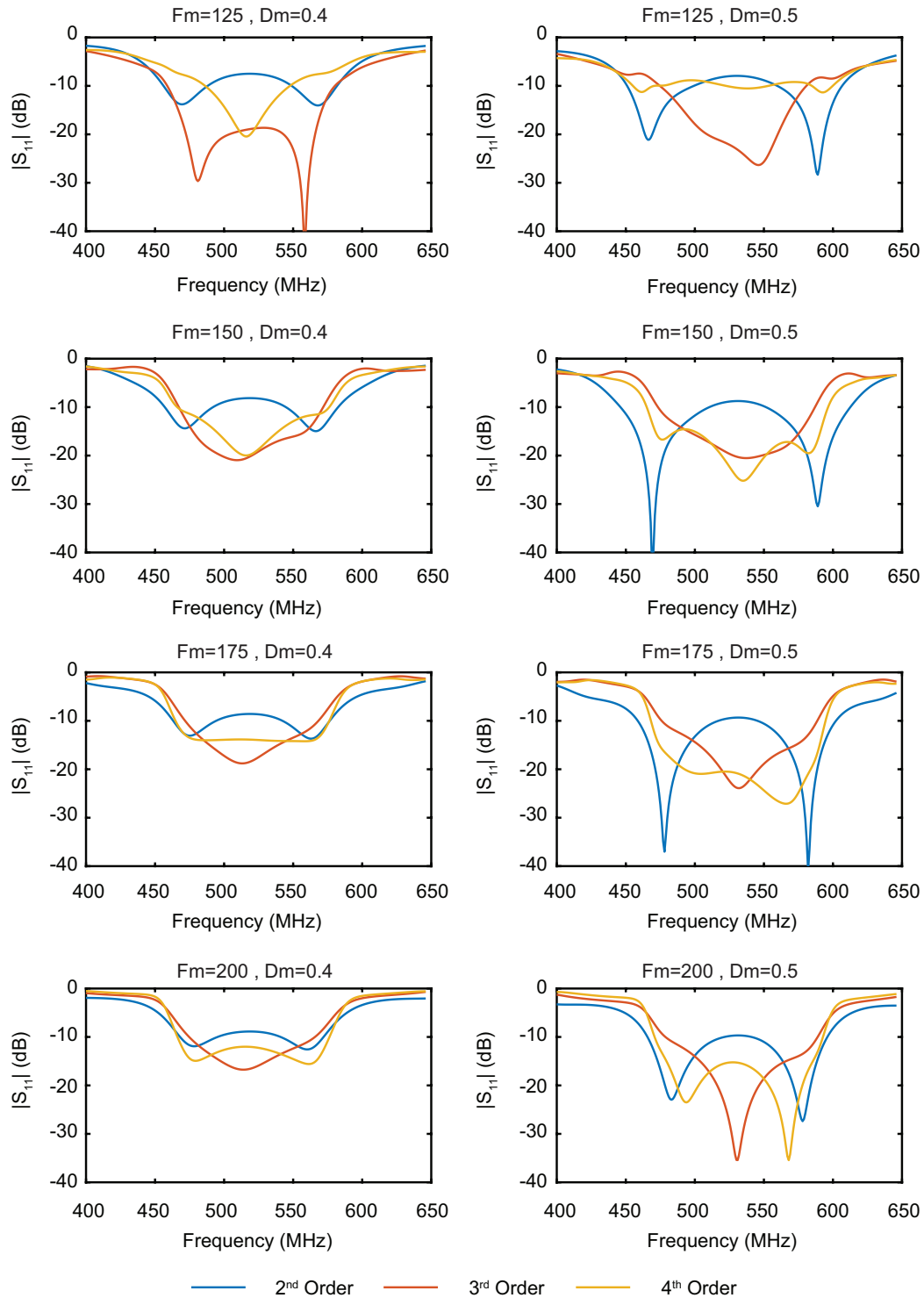
Figure 3.2: Modulated $|S_{11}|$ responses for 2nd, 3rd, and 4th order circulators under optimum range of f_m and d_m.

49
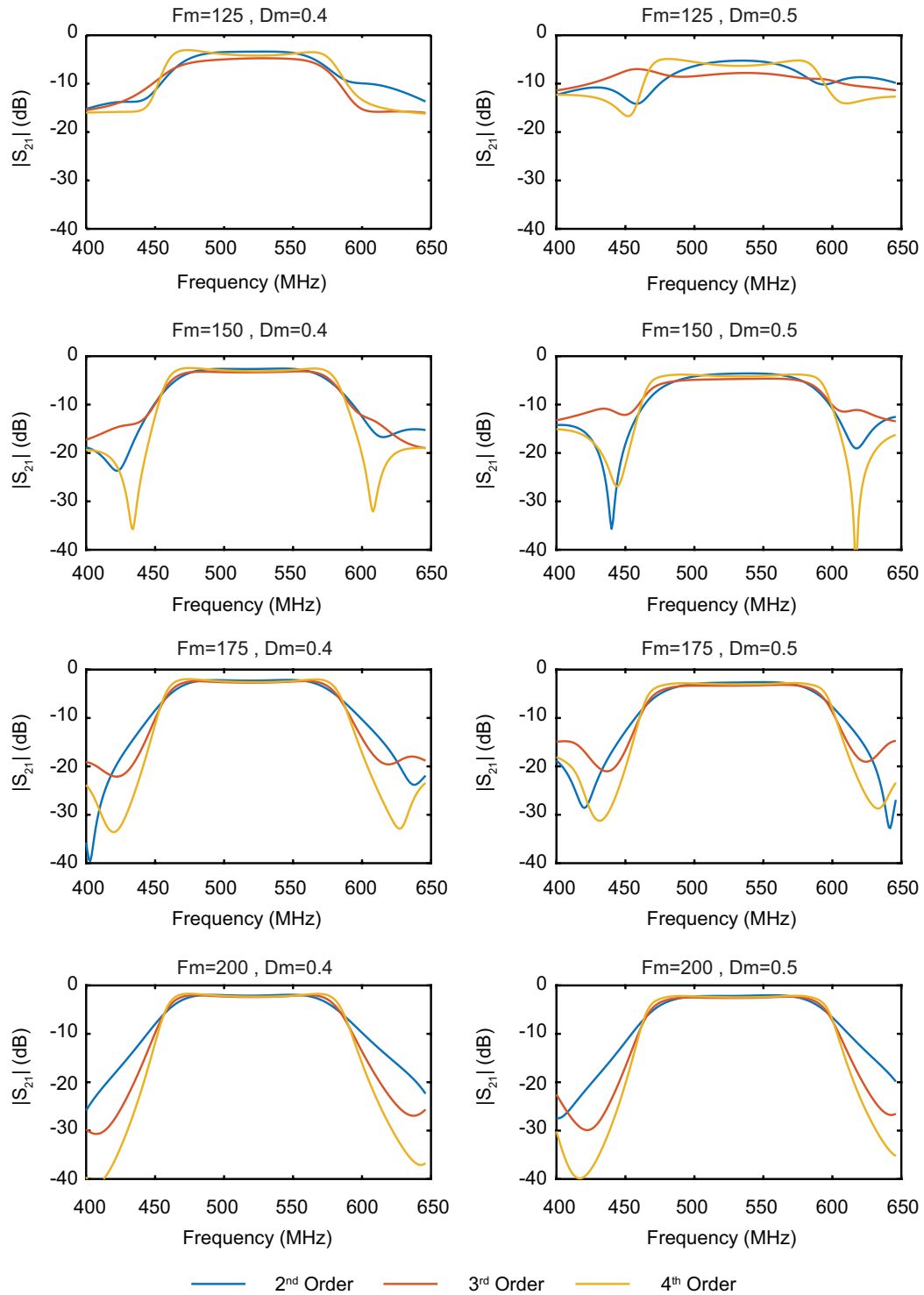
Figure 3.3: Modulated $|S_{21}|$ responses for 2nd, 3rd, and 4th order circulators under optimum range of f_m and d_m.
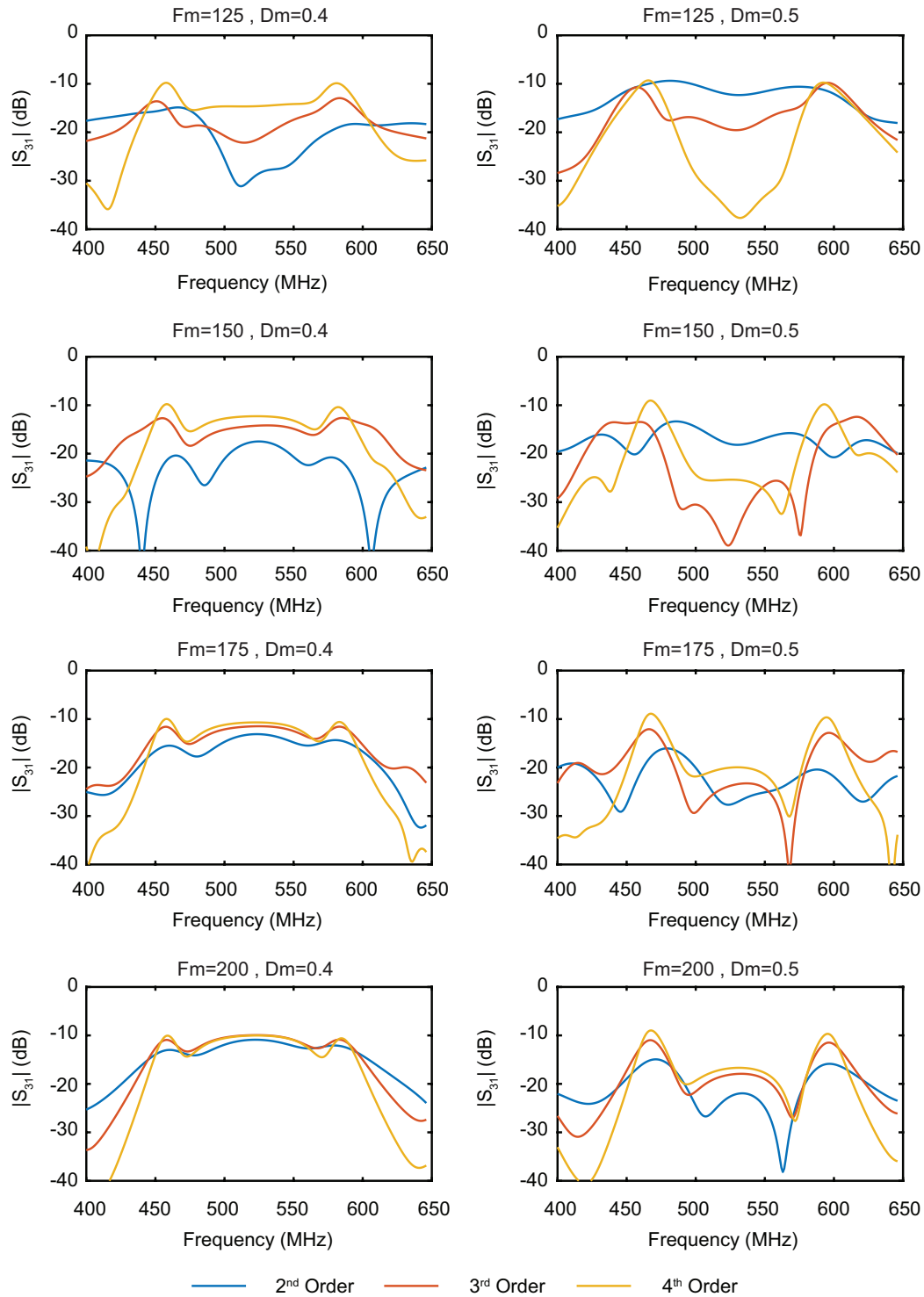
Figure 3.4: Modulated $|S_{31}|$ responses for 2nd, 3rd, and 4th order circulators under optimum range of f_m and d_m.

3.2 Generalized Relationship of Modulated 20-dB IX FBW and Static Filter 3-dB FBW

The proposed design technique in the previous chapter is a two-step design procedure: First, the circulator Y-network is synthesized at a desired frequency f_0 and to attain a $|S_{21}|$ passband of certain 3-dB FBW. Second, the $|S_{31}|$ is attenuated by the application of STM. The modulation parameters (f_m and d_m) are optimized, such that we can reach a compromise between IL, matching, and 20-dB IX BW. In this section, we would like to investigate the relationship between the filter static 3-dB FBW and the circulator modulated 20-dB IX FBW for 2nd, 3rd, and 4th order circulators. We envision that finding this relationship could act as a lookup table for future designers to choose the static 3-dB FBW that would satisfy their required 20-dB IX FBW. Fig. 3.5 depicts the steps taken during this study. As mentioned earlier we will conduct this study for different orders, hence the first step is to choose the order of the circulator circuit. Second, the static filter 3-dB FBW is selected, where the FBW under study are from 0 to 30 % with an incremental step of 5 %. We have stopped at 30 %, since this is the maximum fractional bandwidth that can be practically implemented with conventional lumped or discrete components. After the Y network is constructed via the steps illustrated in section 2.2.3, we sweep the modulation parameters. To give a generic description for the modulation frequency, we normalize it to the 3-dB filter static bandwidth. For this study, f_m is swept from $(0 - 2.5)$ 3-dB BW. For each f_m, the modulation index is increased until the isolation is below 20 dB. Any further increase will decrease the 20-dB IX BW and increase the insertion loss. For illustration, we show the $|S_{31}|$ response as we vary d_m for the case of 3-dB FBW=10 % and normalized $f_m = 1.5$. In this case, we stop at $d_m = 0.25$. Finally, it should be noted that the center frequency is 500 MHz.

The corresponding results are depicted in Fig. 3.6, where we normalize the 20-dB IX FBW with respect to the 3-dB FBW and normalize the f_m with respect to the absolute 3-dB BW. Interestingly from the figure, one can observe that the normalized 20-dB IX FBW is almost constant with respect to the normalized f_m. Moreover, the flatness of the curve is maintained across the different 3-dB FBW. This observation indicates that the
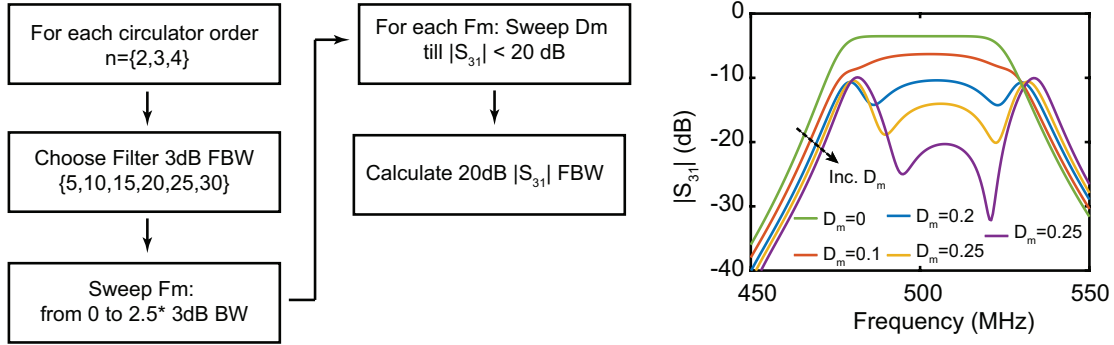
Figure 3.5: Illustration showing a flow chart of the steps taken to find the relationship between the circulator modulated 20-dB IX FBW and the static filter 3-dB FBW.

relationship between the normalized 20-dB IX FBW and the normalized f_m is independent of the filter 3-dB FBW. Furthermore, we can also clearly see that this observation also applies to the other orders as well. This fact greatly simplifies the design and optimization of higher order STM based circulators. Fig. 3.7 depicts the 20-dB IX FBW versus the 3-dB FBW evaluated at $f_m = 2*(\text{3-dB BW})$. From the figure, one can clearly see the linear relationship, which is maintained across all orders. Matlab is used to curve fit the simulated data, where the corresponding equation is found to be $y = 0.6x$.
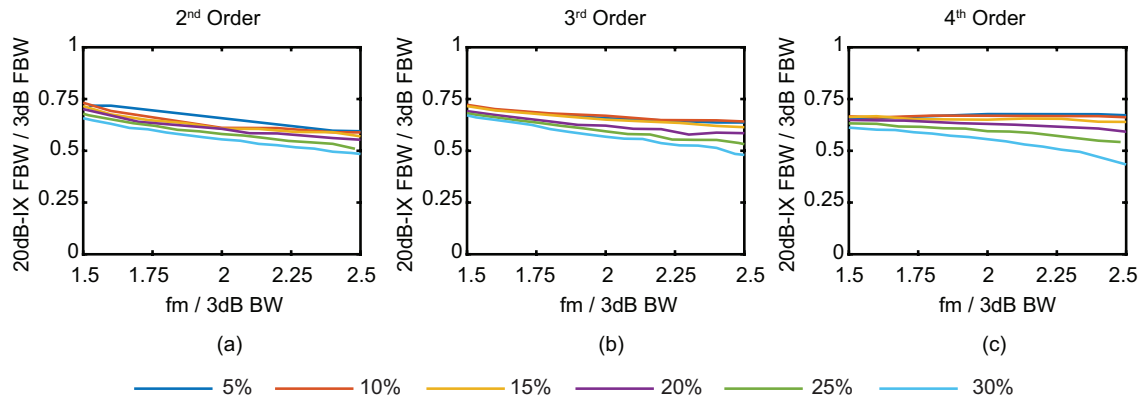
Figure 3.6: The normalized 20-dB IX FBW versus the normalized f_m across different 3-dB FBW for (a) 2nd, (b) 3rd, and (c) 4th order circulators.

3.3   Circulator Insertion Loss

Although the isolation is an important metric of a circulator, the insertion loss is also a key parameter. This is because the circulator is the first component, after the antenna,
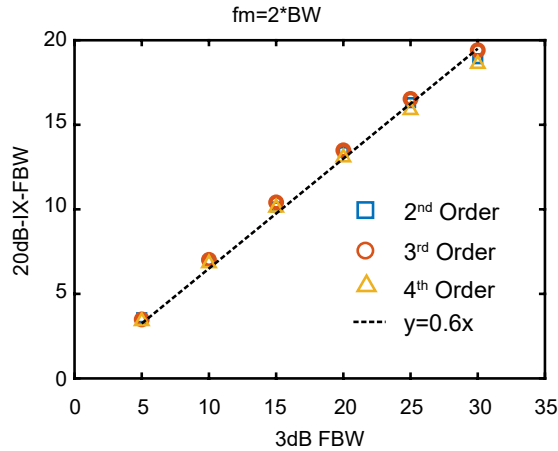
Figure 3.7: Linear relationship between the 20-dB IX FBW and the 3-dB FBW evaluated at $f_m = 2 * (3\text{-dB BW})$.

along the receiver chain. As a result the receiver's overall noise figure is dominated by the circulator noise figure, which since it is a passive device is equal to its insertion loss.

In this section, we would like to turn our attention to the insertion loss of the circulator, and its relationship to the modulation frequency. Fig. 3.8 (a) depicts the insertion loss at the center frequency as we vary the normalized f_m for the different orders. It should be noted that we fixed the static 3-dB FBW to be 5 %.
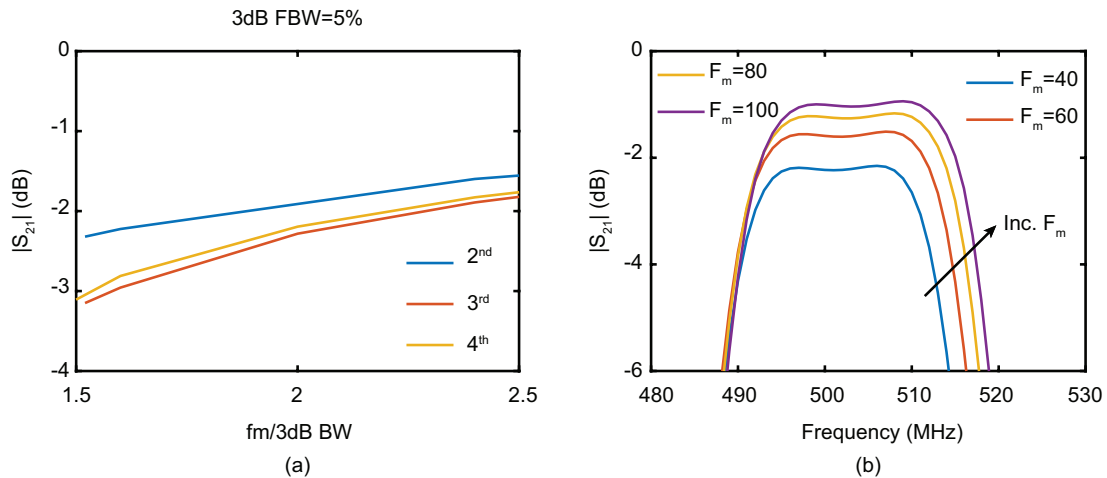
Figure 3.8: Insertion loss trends. (a) $|S_{21}|$ plotted against the normalized f_m for the different orders at 3-dB FBW $= 5$ %. (b) In-band $|S_{21}|$ response with increasing f_m for 2nd order case.

From the figure, we can observe that the insertion loss decreases (improves) as we

increase the normalized f_m. Moreover, as we increase the order, the insertion loss increases (deteriorates). However, the incremental increase in the insertion loss due to the increase in the order tends to saturate at around $f_m = 2.5 * (3\text{-dB BW})$. Fig. 3.8 (b) depicts the in-band $|S_{21}|$ response for the case of the 2nd order, where we can clearly observe that the $|S_{21}|$ response shifts up towards $0\,\mathrm{dB}$ as we increase the modulation frequency f_m.
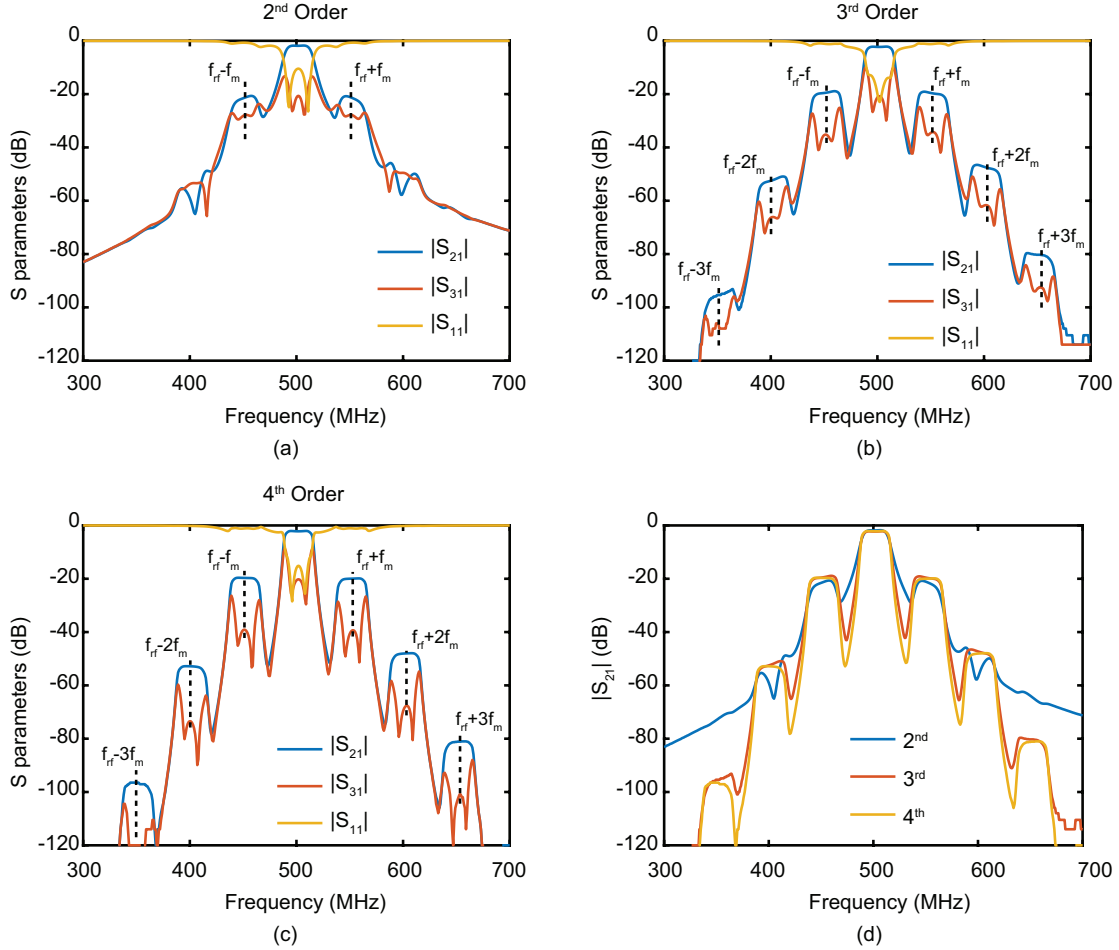
Figure 3.9: Images of the passband created at the intermodulation products ($f_{rf} \pm n f_m$). (a) 2nd order, (b) 3rd order, (c) 4th order, and (d) $|S_{21}|$ of all orders, where the images become more apparent for $n > 2$.

To further investigate the $\mathrm{IL} - f_m$ dependency, we simulate the various orders over a wide range of frequency. Fig. 3.9 depicts the results for the case of FBW $= 5\,\%$. From the figure, we can see that due to the application of spatial-temporal modulation, images of the passband appear at the intermodulation products. Also, the images at higher order intermodulation products become more visible as we increase the circulator order. This
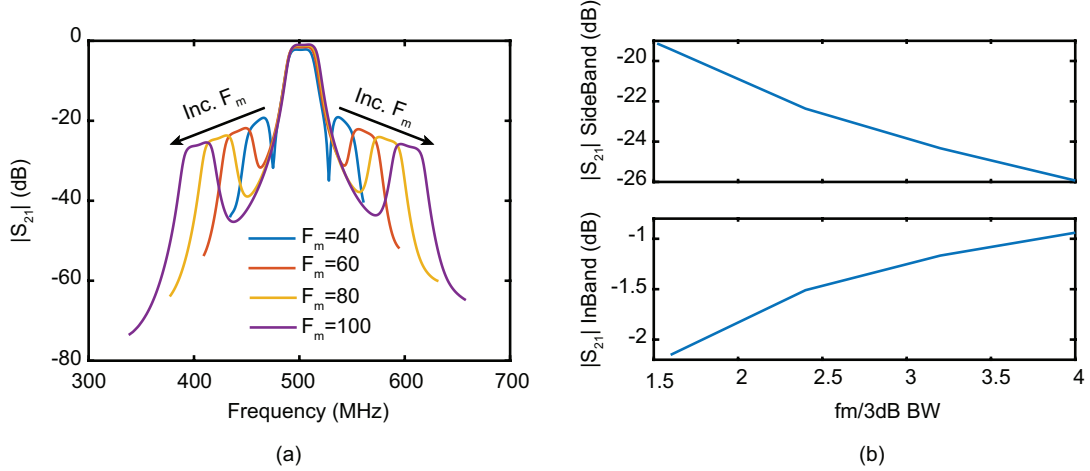
Figure 3.10: (a) Circulator response due to the increase in f_m. (b) In-band and passband-images (sidebands) $|S_{21}|$ trend with increasing f_m.

could be attributed to the fact that the filter-like skirt response of the circulator becomes sharper as we increase the order. Therefore, the images at higher order intermodulation frequencies can stand out from the filter roll-off skirt (Fig. 3.9 (d)). Another point of view is that as we increase the circulator order, the amplitude of the higher order intermodulation mixing products increases leading to their prominent appearance in the spectrum. The reason behind the increase in the insertion loss as we increase the circulator order (Fig. 3.8 (a)) could also be explained by noticing that at the intermodulation products the response is also non-reciprocal. This indicates that some energy is consumed to break the reciprocity at the intermodulation products, whose mixing product order increases as we increase the circulator order.

Fig. 3.10 (a) shows the spectrum of the 2nd order circulator (FBW = 5 %) as we increase the modulation frequency. From the figure, we can see that the images effectively create transmission zeros in the circulator frequency response. From microwave filter theory, it is well known that placing transmission zeros very close to the passband of the filter cause the insertion loss to increase. Thus, increasing f_m pushes away the images, and hence the accompanying transmission zeros away from the passband. As a result the insertion loss decreases. This is confirmed by Fig. 3.10 (b) where the in-band insertion loss decreases as we increase the modulation frequency (to generalize we normalized it to the filter 3-dB BW). Similarly, the $|S_{21}|$ amplitude at the intermodulation products decreases as we

56

increase f_m indicating that they are shifted towards higher frequencies.

It is worth mentioning that increasing the f_m has the advantage of improving the insertion loss, however from a practical implementation point of view there should be a sufficient $f_{rf} - f_m$ isolation. As f_m increases, it approaches f_{rf} and reduces the isolation, which forces the designer to use complicated duplexer circuits (in most cases these circuit trade isolation with insertion loss). This fact puts an upper limit on the choice of f_m. Gaining insight of the images created at the intermodulation products can be used to find the lower limit of f_m. Recall from the sampling theorem that if the sampling frequency does not follow Nyquist sampling rate ($f_s \geq 2\,\text{BW}$), then aliasing will occur [48]. Considering both factors, we find $f_m = 1.5\,(3\text{-dB BW})$ is a good starting point.
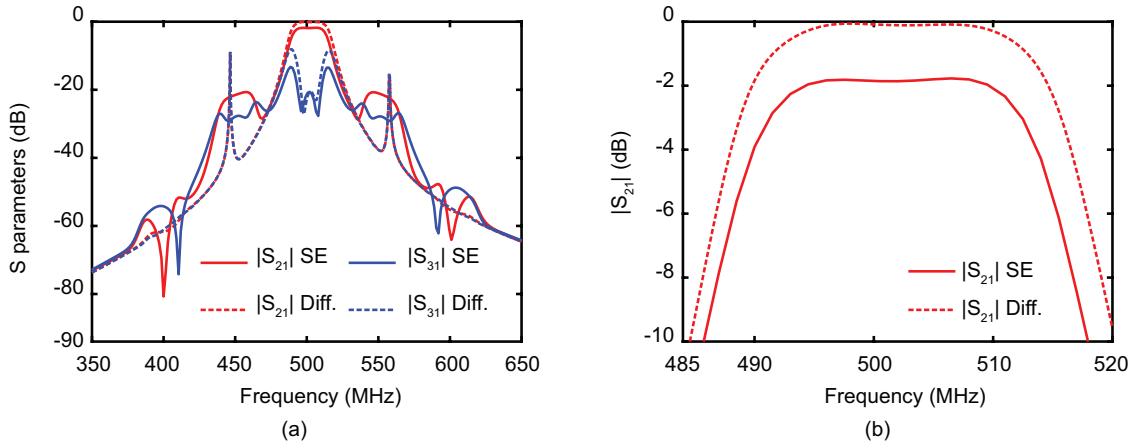
Figure 3.11: Comparison of single ended and differential typologies for 2nd order circulator for FBW $= 5\,\%$ and $f_m = 50\,\text{MHz}$. (a) $|S_{21}|$ and $|S_{31}|$. (b) In-band $|S_{21}|$.

3.3.1 Differential Topology

In [22], magnetic free circulators using STM of RF resonators connected in a differential topology have been suggested to reduce the insertion loss. Fig. 3.11 compares the S-parameters of 2nd order circulators with single and differential typologies. Both circulators are designed for FBW of $5\,\%$. It should be noted that the modulation parameters of both circuits are optimized, such that the isolation is below $20\,\text{dB}$. Also, the differential topology needs lower values of modulation frequency and depth to reach the 20-dB IX level ($f_{m,SE} = 50\,\text{MHz}$ and $f_{m,Diff.} = 25\,\text{MHz}$, $\xi_{SE} = 0.09$ and $\xi_{Diff} = 0.14$). Moreover from Fig. 3.11(a), we can see that the differential typology managed to not only remove

the images at the $f_{rf} \pm f_m$, but also to make the response at these frequency reciprocal. As a result, more energy is preserved, and the insertion loss decreases by about $2\,\mathrm{dBs}$ as shown in Fig. 3.11(b).

3.4   Conclusion

In this chapter, we first investigate the behaviour of higher order STM based circulators, namely 2nd, 3rd, and 4th orders. Based on these studies, we conclude that increasing the order has the advantage of having a sharper roll-off. In contrary to our initial intuition, increasing the order did not result in additional poles in the reflection and isolation responses. Second, we investigated the relationship between the modulated circulator 20-dB IX FBW and the static filter 3-dB FBW. The study reveals that a linear relationship exists and is found to be $y = 0.6x$. Moreover, this relationship is independent of the modulation frequency as well as is valid to all investigated orders. Finally, we investigate the dependency of the circulator insertion loss on the modulation frequency. Our study shows that STM creates images of the passband at the intermodulation frequencies. As a result Nyquist sampling theorem can be applied to set a lower limit on the modulation frequency $(f_m = 2\,\mathrm{BW})$. Moreover, the images create transmission zeros in the circulator passband. Thus, increasing the modulation frequency pushes the transmission zeros away from the passband causing a reduction in the insertion loss. Another important point to mention is that increasing the modulation frequency reduces the $f_{rf} - f_m$ isolation. As a result we propose a starting value of $f_m = 1.6\,\mathrm{BW}$. Finally, we illustrate that employing a differential topology improves the insertion loss, since it cancels the images created at the intermodulation frequencies..

Chapter 4

Novel Multi-functional Non-Reciprocal Filtering Microwave Power Divider Using Space-Time Modulated $\lambda_g/2$ Resonators

This chapter reports a novel multi-functional microwave power divider (PD), where the proposed circuit is designed to provide, in addition to a 3-dB equal-power split, the responses of a bandpass filter (BPF) and an isolator. First, the co-design of a PD and BPF is achieved through the use of six distributed varactor-loaded half-wavelength resonators arranged into two branches of three inline coupled resonators. Second, the isolation functionality is integrated by spatially and temporally modulating the varactors with sinusoidal signals, which breaks the reciprocity without relaying on bulky magnets. As a proof of concept, an isolating and a filtering power divider (IFPD) is designed at a center frequency of $900\,\mathrm{MHz}$ and a fractional bandwidth (FBW) of $5\,\%$. The fabricated prototype shows an insertion loss of $3.37\,\mathrm{dB}$, a port-to-port isolation better than $20\,\mathrm{dB}$ across the band, a 20-dB reverse transmission isolation bandwidth of $45\,\mathrm{MHz}$, and an impedance match at all ports better than $10\,\mathrm{dB}$ across the operating bandwidth.

4.1 Introduction

The everlasting demand for reducing the cost of wireless communication systems, and at the same time supporting more services has fueled researchers to devise various miniaturization techniques. One common approach is to replace a cascade of devices with a single device having the capability of performing the functionality of all the replaced devices. This approach has the advantage of not only size reduction, but also alleviates the insertion loss of the additional interconnects [49, 50].

BPFs, PDs, and isolators are crucial components in most modern wireless systems. Several literature report the co-design of a BPF and a PD (a FPD) [51–53]. In [51], the $\lambda/4$ transmission lines of a conventional Wilkinson power divider are replaced by J-inverters along with a number of coupled resonators. The resonators are implemented as a folded net-shaped microstrip resonators. Based on that, the authors have demonstrated a FPD with a second and a third order Chebyshev bandpass filter response. Also, they have presented a PD with a fourth order quasi-elliptic filter response with two transmission zeros to improve the filter selectivity. In [52], the authors have improved the in-band isolation and reduced the amplitude and phase imbalances by introducing a highly symmetric coupling FPD structure. In [53], a tunable FPD with quasi-elliptic filter response is presented, where the center frequency is tuned via varactors while preserving the filter absolute bandwidth.

Regarding isolators, they are non-reciprocal devices that are conventionally implemented using magnets or ferromagnetic materials. This hinders their integration with CMOS IC fabrication processes, and results in high-cost and bulky devices. In [1], the reciprocal two-way transmission is broken via the usage of split-ring resonators loaded with a unilateral transistors. Although a strong non-reciprocity is achieved, the proposed isolator suffered from poor power handling.

Several approaches are studied to alleviate the need of magnets, one of those is the use of time-variance [9, 13, 38]. In [9], the authors have demonstrated that the non-reciprocity can be broken by biasing the circuit with angular momentum as oppose to using a magnetic field. The angular momentum biasing is implemented in the RF/microwave circuits

domain by modulating a number of RF resonators arranged in space with time-shifted sinusoidal signals. The authors have referred to such modulation as spatial-temporal modulation (STM).

Since its introduction, STM has been extensively studied and used in the design of magnet-free circulators [21,22,35,46,47,54], because of their potential usage in the upcoming 5G full-duplex transceivers. It is worth mentioning that STM differential circulators have shown excellent performance in terms of low insertion loss, wideband isolation, and high power handling [22,35].

Moreover in [55], Wu et. al have illustrated for the first time, to our best knowledge, the spectral analysis and co-design of an STM based filtering isolator (FI). The fabricated prototype has shown a second order Chebyshev filter-like characteristics with only 1.5 dB of insertion loss and a 20-dB reverse isolation across 15% fractional bandwidth ($f_0 = 200$ MHz). In addition, reference [56] has generalized the analysis to a coupled matrix representation. To verify the analysis, the authors have demonstrated a magnet-free FI based on third and fourth order Chebyshev filters. It should be noted that the filters have been implemented by $\lambda/4$ microstrip resonators, which led to a significant size reduction.

Furthermore, the first demonstration of a non-reciprocal filtering splitter was reported in [57], where the authors cascaded a Wilkinson power divider with a non-reciprocal magnetic-free filter. It should be noted that the two circuits are designed individually, then they are cascaded serially. On the contrarily, in this work we combine the well-established microwave filter design techniques with the concept of STM to design an isolating and a filtering 3-dB microwave power divider (IFPD). The proposed IFPD can replace the conventional cascade of the three individual components (Fig. 4.1 (a)) with a single component (Fig. 4.1 (b)), hence it can save considerable area as well as reduce cost and insertion loss. This chapter is organized as follows. Section 4.2 discusses the analysis and circuit design which is decomposed of static and modulated modes. The static mode is focused on the filter and power divider co-design, while the modulated mode is dedicated for the integration of the isolator functionality through STM. Section 4.3 discusses the
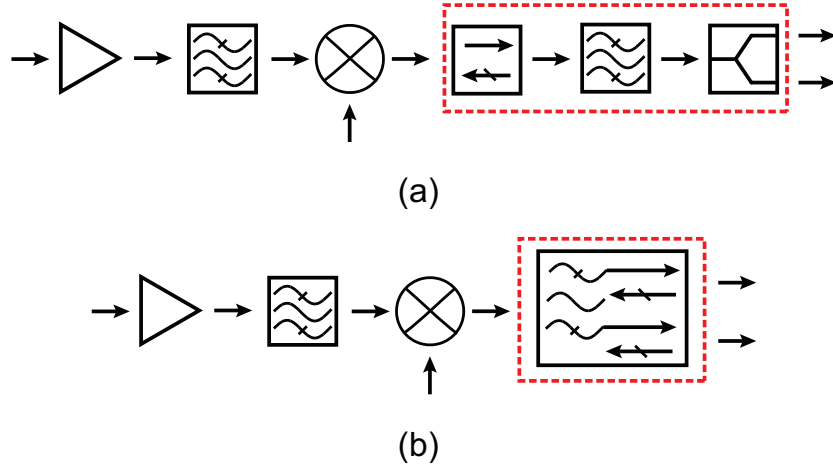
Figure 4.1: Block diagram of a generic RF front-end with (a) individual isolator, BPF, and a PD and (b) proposed IFPD.

measurement results and their correlation with simulations. Section 4.4 concludes the chapter.

4.2 Analysis and Circuit Design

As demonstrated in [11, 55, 58], the circuit behaviour during forward transmission is not significantly affected by the application of space-time modulation. This finding simplifies the design process, since one can firstly design the circuit to satisfy a certain desired static response. Secondly, the modulation is applied to yield a non-reciprocal response.

In this section, we start by synthesizing the static circuit response to achieve a $3\,\mathrm{dB}$ power divider with an integrated functionality of a bandpass filter. After that, the non-reciprocity is broken by modulating the circuit simultaneously in space and time, and thus realizing an isolator.

4.2.1 Static Mode

4.2.1.1 Theoretical Analysis

The proposed topology for the filtering 3-dB power divider (FPD) is shown in Fig.4.2 (a). As depicted, the FPD is composed of two branches split at the input port/source, and each branch has 3 coupled resonators. Under even-mode excitation, the circuit behavior is reduced to only one branch as shown in Fig. 4.2 (b). This equivalent circuit constitutes a 3-pole filter whose response can be sculptured into any desired response by specifying
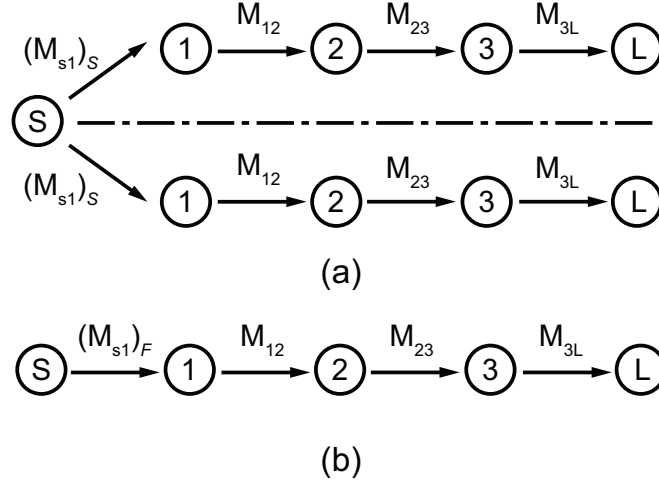
Figure 4.2: (a) Topology of the proposed filtering power divider and (b) Equivalent topology under even-mode excitation.

the external quality factor and coupling coefficients. The corresponding coupling matrix for this 3-pole filter can be described as [44]

$$
M = \begin{bmatrix}
0 & (M_{S1})_F & 0 & 0 & 0 \\
(M_{S1})_F & M_{11} & M_{12} & M_{13} & 0 \\
0 & M_{12} & M_{22} & M_{23} & 0 \\
0 & M_{13} & M_{23} & M_{33} & M_{3L} \\
0 & 0 & 0 & M_{3L} & 0
\end{bmatrix}
\tag{4.1}
$$

, where we only assume direct coupling i.e. neither cross coupling nor source/load coupling exist. Also, we consider all resonators to have the same resonant frequency (synchronously tuned filter), which implies that $M_{11} = M_{22} = M_{33} = 0$. It should be noted that since we are operating under even mode excitation, therefore the filter source impedance is half that of the original power divider. This can be expressed in terms of the mutual coupling as

$$
(M_{S1})_F = \sqrt{2} \times (M_{S1})_S.
\tag{4.2}
$$

Moreover, M_{S1} can be written as

$$
M_{S1} = \frac{1}{\sqrt{Q_{e,in} \times FBW}}
\tag{4.3}
$$

, where FBW is the filter fractional bandwidth and $Q_{e,in}$ is the input quality factor. Combining (4.2) with (4.3) and at given FBW results in

$$(Q_{e,in})_F = 0.5 \times (Q_{e,in})_S. \tag{4.4}$$

The significance of (4.4) is that the filter and PD will have the same input impedance characteristics, despite adding a second branch, if the filter is designed with twice its $Q_{e,in}$. Meanwhile, all the other coupling coefficients are kept unchanged.

For illustration, we choose a 3-pole Chebyshev filter with 0.043 dB passband ripple level, center frequency $f_0 = 900$ MHz, and FBW $= 5\%$. This corresponds to lowpass prototype values of $g_0 = g_4 = 1$, $g_1 = g_3 = 0.8516$, and $g_2 = 1.1032$. From the LPF prototype, the mutual coupling coefficients can be computed as

$$M_{S1} = \frac{1}{\sqrt{g_0 g_1}}$$
$$M_{ij} = \frac{1}{\sqrt{g_i g_j}} \tag{4.5}$$
$$M_{3L} = \frac{1}{\sqrt{g_3 g_4}}$$

, where i and j=1,2,3 (i $\neq$ j). Based on (4.5) and the prototype values, the corresponding coupling matrix becomes

$$M = \begin{bmatrix} 0 & 1.0836 & 0 & 0 & 0 \\ 1.0836 & 0 & 1.0317 & 0 & 0 \\ 0 & 1.0317 & 0 & 1.0317 & 0 \\ 0 & 0 & 1.0317 & 0 & 1.0836 \\ 0 & 0 & 0 & 1.0836 & 0 \end{bmatrix}. \tag{4.6}$$

With the given f_0 and FBW, the PD external quality factors and coupling coefficients can be computed through

$$Q_{e,in} = \frac{2}{FBW \times M_{S1}^2}, \tag{4.7}$$
$$Q_{e,out} = \frac{1}{FBW \times M_{3L}^2}, \tag{4.8}$$
$$k_{12} = FBW \times M_{12} = k_{23}, \tag{4.9}$$

, which are found to be: $Q_{e,in} = 34.1$, $Q_{e,out} = 17$, and $k_{12} = k_{23} = 0.0516$.
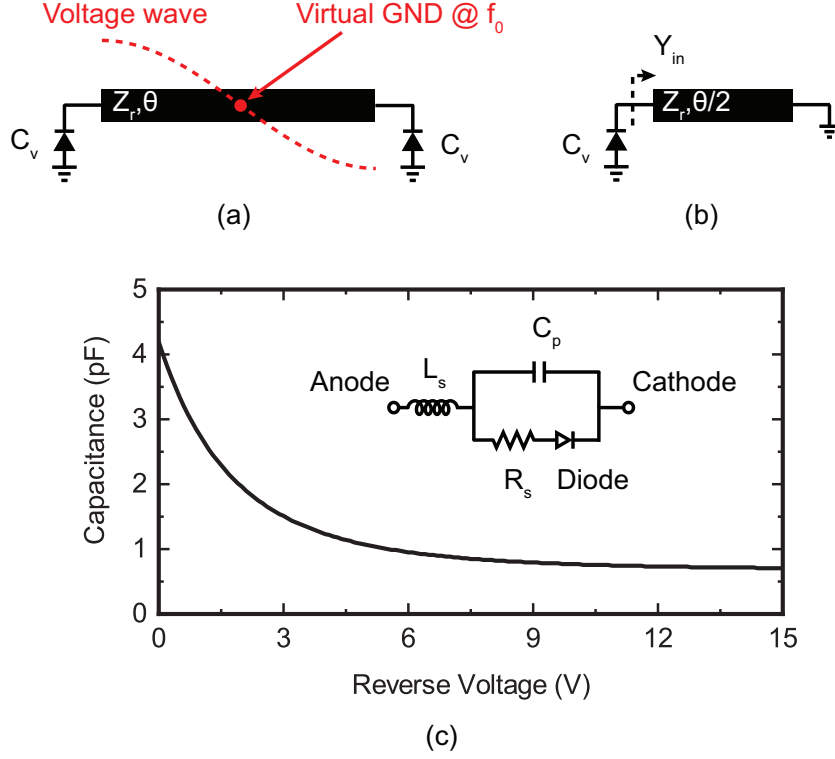
Figure 4.3: (a) Half-wavelength symmetrically varactor-loaded resonator, (b) odd-mode half circuit, and (c) C-V curve and circuit model of Skyworks SMV1232 varactor with $L_s = 1.7$ nH, $R_s = 1.5\,\Omega$, and $C_p = 0.68\,\text{pF}$.

4.2.1.2 Resonator

In this work, we choose a half-wavelength resonator, which is symmetrically loaded on both sides with varactors. The voltage distribution of the fundamental resonant mode has a virtual RF ground at the center of the resonator as depicted in Fig. 4.3 (a). As explained in [58], this virtual RF ground provides an inherent isolation between the RF signal (f_{rf}) and the DC/modulating signal (f_m). As a result, a high $f_{rf} - f_m$ isolation can be achieved, which extremely simplifies any required additional duplexing circuits.

The resonator's input admittance under odd-mode excitation (Fig. 4.3 (b)) can be found to be

$$Y_{in} = j(\omega C_v - Y_r \cot(\frac{\theta}{2})). \tag{4.10}$$

The resonant frequency can be evaluated by equating $Y_{in} = 0$, resulting in

$$f_{res} = \frac{Y_r}{2\pi C_v} \cot\left(\frac{\theta}{2}\right) \tag{4.11}$$

65

For a target resonant frequency of 900 MHz and by setting $Z_r = 80\,\Omega$ and $\theta = 127^o$, the loading capacitor value becomes $C_v = 1.1\,\mathrm{pF}$. Skyworks SMV1232 varactor is used in this work, whose C-V curve and circuit model are shown in Fig. 4.3 (c). Based on that, a dc bias voltage of $V_{dc} = 5\,\mathrm{V}$ corresponds to the required capacitance.

4.2.1.3   Filtering Power Divider Implementation

In this section, we follow Dishal's methodology [44, 59] to realize the desired filter parameters ($Q_{e,in}$, $Q_{e,out}$, and coupling coefficient $K = K_{12} = K_{23}$). In order to reduce the resonator form factor, we fold it to form a ring-shaped resonator as shown in Fig. 4.4 (a). Moreover according to Dishal's method, design curves relating the filter electrical parameters to the physical dimensions are needed.

First, for $Q_{e,in}$ and $Q_{e,out}$, a two-port network is formed by coupling two sources on each side of the resonator. The coupling is done through a coupled-line structure, which is formed between the feedline and the lateral side of the resonator as depicted in Fig. 4.4 (a). Then, the Q_e can be determined from the $|S_{21}|$ (dB) response by applying

$$Q_e = \frac{2f_0}{\Delta f_{3\,dB}} \tag{4.12}$$

, where f_0 is the resonance frequency (fixed at 900 MHz by the biasing voltage V_{dc}) and $\Delta f_{3\,dB}$ is the 3-dB bandwidth. It should be noted that the feedline for $Q_{e,in}$ is longer as compared to that of $Q_{e,out}$. Also, its source impedance is $Z_s = 100\,\Omega$, while for $Q_{e,out}$ its $Z_s = 50\,\Omega$. This is to account for the second branch that will be added to form a power divider, and to keep the input impedance unaltered, respectively. Finally, for simplicity the V_{dc} is fed through an ideal RF choke.

The Q_e is affected by how much power is coupled through the coupled-line structure. Thus, it is dependant on the gap of coupled-line (g_f), the length of coupled-line (L_{c1}/L_{c2}), and the capacitor connected to the end of the feedline (C_1/C_2). Qualitatively, the capacitor value changes the voltage/current distribution along the feedline, hence changes the amount of coupled energy concentrated in the region of coupled-line structure.

Fig. 4.4 (b) shows the extracted $Q_{e,in}$ for different capacitor C_1 values and coupled-line L_{c1} length under a fixed gap of $g_f = 0.2\,\mathrm{mm}$. It is observed that $Q_{e,in}$ is inversely proportional to both L_{c1} and C_1. According to this figure, a $Q_{e,in} = 34.1$ can be realized at

$L_{c1} = 20.9\,\text{mm}$ and $C_1 = 2\,\text{pF}$. Similarly, Fig. 4.4 (c) shows the extracted $Q_{e,out}$ for different capacitor C_2 values and coupled-line L_{c2} length under a fixed gap of $g_f = 0.2\,\text{mm}$. In this case, a $Q_{e,out} = 17$ can be implemented at $L_{c2} = 20.2\,\text{mm}$ and $C_2 = 2\,\text{pF}$.
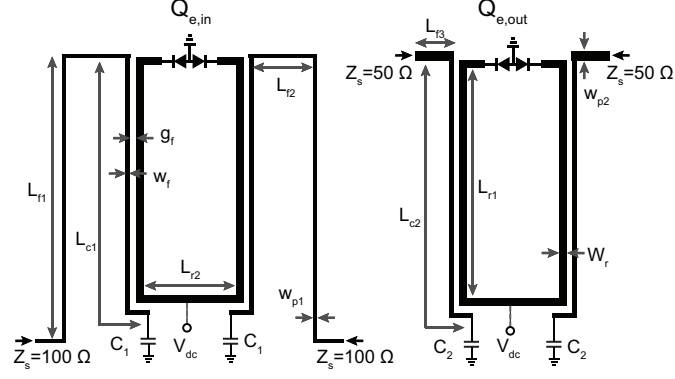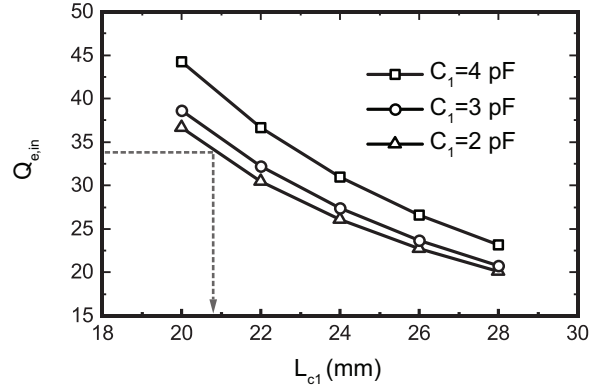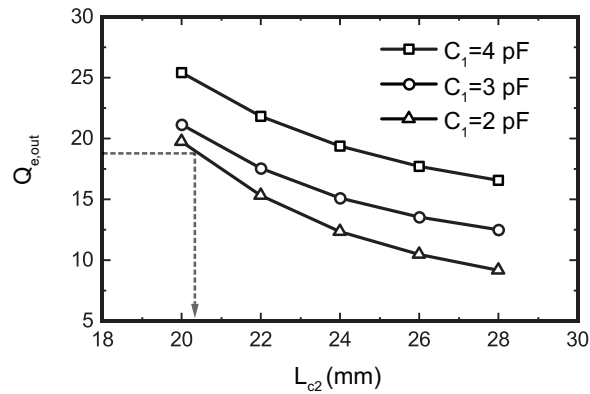
Figure 4.4: (a) Circuit model for extracting $Q_{e,in}$ and $Q_{e,out}$. (b) $Q_{e,in}$ and (c) $Q_{e,out}$ for different coupling length and capacitor values. Here, $L_{f1} = 45\,\text{mm}$, $L_{f2} = 10\,\text{mm}$, $L_{f3} = 5\,\text{mm}$, $L_{r1} = 29.2\,\text{mm}$, $L_{r2} = 9.3\,\text{mm}$, $W_{p1} = 0.42\,\text{mm}$, $W_{p2} = 1.78\,\text{mm}$, $W_f = 0.5\,\text{mm}$, $W_r = 0.73\,\text{mm}$.

Second, for the coupling coefficient (K) we construct a 2-port network composed of two resonators separated by a distance (S). Then, each resonator is weakly coupled to a source of $50\,\Omega$ impedance as depicted in Fig. 4.5 (a). The weak coupling condition is applied to eliminate the loading effect of the source impedance, and is enforced by the ideal transformer turn ratio (N).

In general, the coupling between 2 resonators in close proximity of one another is due to their intertwined time varying electric and magnetic fields. Depending on the relative orientation of the 2 resonators, a single or mixed electrical and magnetic coupling can be present. In our case, both coupling exist, also they tend to cancel one another [44]. Hence, the total coupling is given by

$$k = \mid k_m \mid - \mid k_e \mid .$$ (4.13)

From the $|S_{21}|$ (dB) response shown in Fig. 4.5 (a), two resonance peaks can be observed. The coupling coefficient can be quantitatively computed as

$$k = \frac{f_2^2 - f_1^2}{f_2^2 + f_1^2}.$$ (4.14)

, where f_1 and f_2 are the first and second resonant frequency, respectively. It should be noted that the transformer turn ratio (N) is adjusted, such that the minimum between the two peaks is at $|S_{21}| = 40\,\text{dB}$ (it is a sign for satisfying the weak coupling condition).

The distance S between the resonators is varied, then (4.14) is used to calculate K at each case. Fig. 4.5 (b) summarizes the results, where one can observe that K is inversely proportional to the distance between the two resonators. It is worth mentioning that at a much higher S-value, K will reach zero. With further increase in S, it will start to increase again. This attributes to the significant decrease in the electric field until the only coupling mechanism is due to the magnetic field. According to this figure, a $K = 0.0516$ can be realized at $S = 0.6\,\text{mm}$.

4.2.2   Modulated Mode

4.2.2.1   Ideal Studies

In order to find the optimal STM parameters, we conducted a parametric study (as suggested in [42]) on an ideal filtering power divider (Fig. 4.2 (a)) with the same characteristics
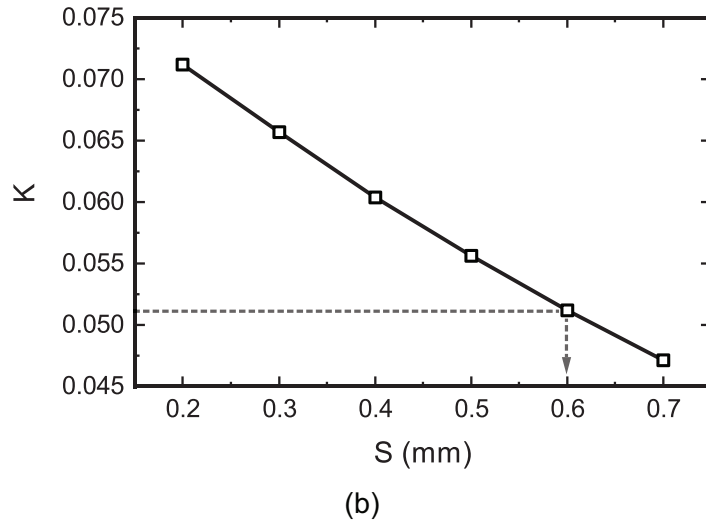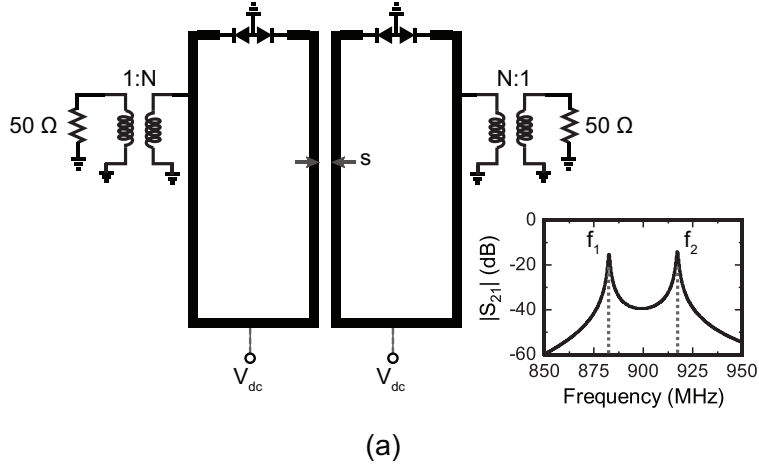
Figure 4.5: (a) K-extraction circuit model and (b) K versus the distance between resonators. Here, N=65.

specified by the even-mode filter discussed in the previous section. It should be noted that the resonators are modeled as ideal LC tanks with a time varying capacitor, which is mathematically described as

$$C_i(t) = C_v \left[1 + \xi \cos(\omega_m t + (i-1)\phi)\right], \tag{4.15}$$

where $i = 1, 2, 3$. C_v is the capacitance calculated in the static mode, ω_m is the modulation angular frequency, ξ is the modulation index, and ϕ is the progressive phase shift. For simplicity, we assume all the resonators have the same modulation index and frequency. This study is conducted in ADS with the help of harmonic balance simulation tool.

Fig. 4.6 summarizes the simulation studies, where the first three columns correspond to

the frequency response with respect to changing f_m/f_{rf} (f_m normalized to f_{rf}=900 MHz), ξ, and ϕ, respectively. The fourth column shows the circuit response under optimal modulation parameters, namely $f_m/f_{rf}=0.044$, $\xi=0.075$, and $\phi=55°$. The five rows in the figure are for the filtering power divider $|S_{11}|$, $|S_{21}|$, $|S_{12}|$, $|S_{22}|$, and $|S_{32}|$, respectively in dB.

As shown in the first column when $f_m/f_{rf}>0.06$, the $|S_{11}|$ and $|S_{22}|$ responses improve and show 3 deep distinctive reflection zeros. However, the $|S_{21}|$ and $|S_{12}|$ show weak non-reciprocity despite being close to 0 dB. Moreover, the port-port isolation $|S_{32}|$ deteriorates to around 10 dB. For $f_m/f_{rf}<0.03$, although the response shows strong non-reciprocity, deep port-to-port isolation, and good matching at both ports, the passband becomes very narrow (response resembles a 1-pole filter response). Based on that, the optimum choice for f_m/f_{rf} lies in the range $0.03-0.06$. A good compromise is found at $f_m/f_{rf}=0.044$.

In regards to the modulation index ξ, the second column shows that the smaller ξ, the lower the insertion loss $|S_{21}|$ and the better the matching at both ports ($|S_{11}|$ and $|S_{22}|$). For instance, although $|S_{12}|$ and $|S_{32}|$ becomes significantly low at around $\xi=0.2$, the $|S_{21}|$ deteriorates reaching around $10-15$ dB. The deterioration in $|S_{21}|$ with the increase in ξ can be attributed to shifting the resonance frequency outside the filter passband. Therefore, ξ should be kept relatively small, and based on the figure a good response can be achieved at $\xi=0.044$.

Regarding the progressive phase shift ϕ, it is interesting to note that $|S_{21}|$ and $|S_{12}|$ have odd-symmetry to one another around $\phi=180°$. Moreover, the port-to-port isolation $|S_{32}|$ has even symmetry around $\phi=180°$. This observation can be useful since we can change the direction of forward transmission while maintaining high port-to-port isolation. For $\phi>120°$, the matching at both ports show only one deep reflection zero, which narrows down the operational bandwidth. A good compromise is found at $\phi=55°$.

4.2.2.2 STM Practical Implementation

In the previous section, we assumed perfect f_m-f_{rf} isolation. Moreover, the inherent isolation due to the virtual ground of the $\lambda/2$ voltage distribution is only valid under odd mode excitation. In general, the resonator will be excited with both even and odd modes,
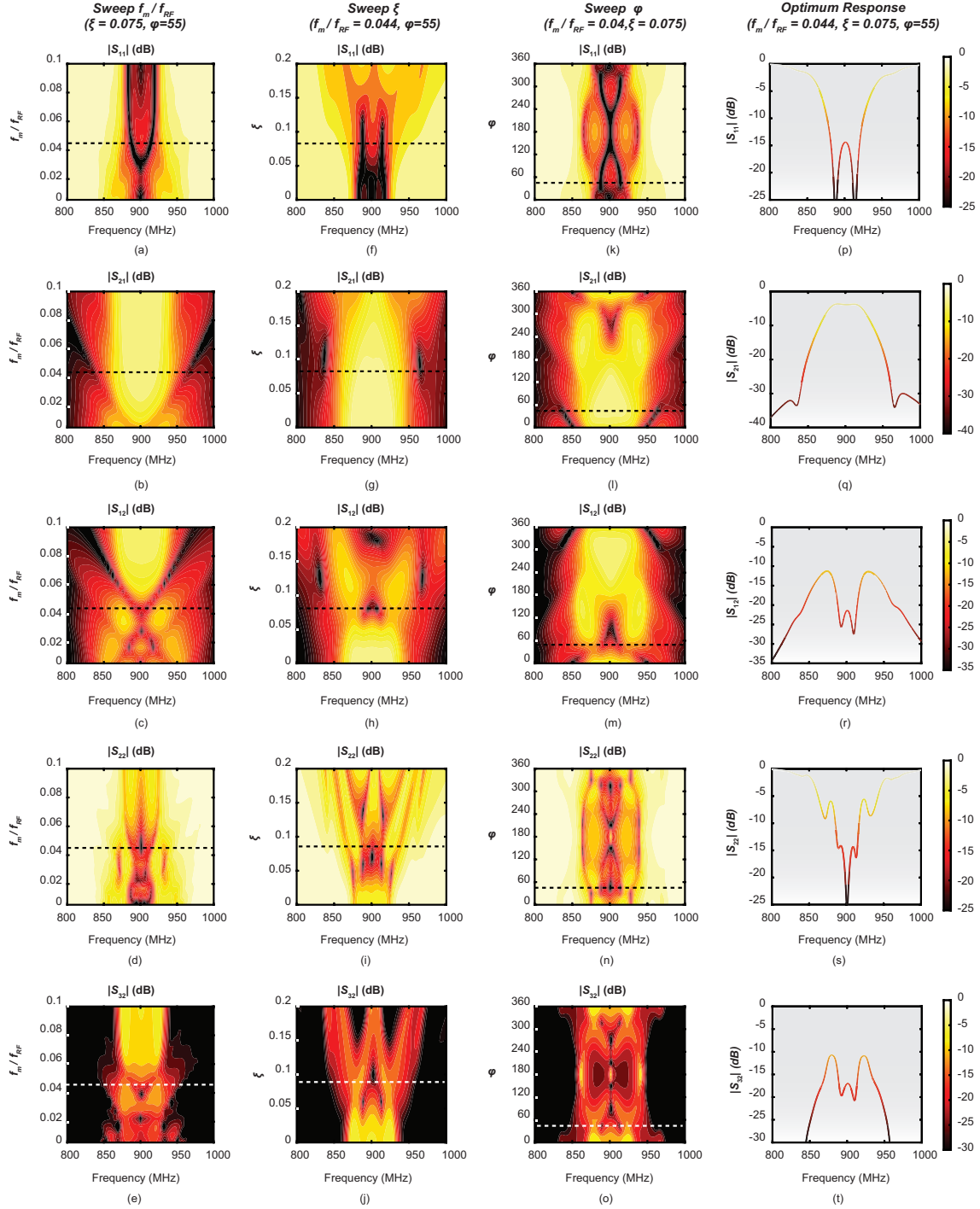
Figure 4.6: Parametric study of the proposed non-reciprocal power divider (the dashed line corresponds to the nominal response). First column shows the effect of varying f_m/f_{RF} (a) $|S_{11}|$, (b) $|S_{21}|$, (c) $|S_{12}|$, (d) $|S_{22}|$, and (e) $|S_{32}|$. The second column (f)$-$(j) illustrates the effect of varying ξ. The third column (k)$-$(o) shows the effect of varying ϕ. Nominal response is highlighted in the fourth column (q)$-$(t).

71
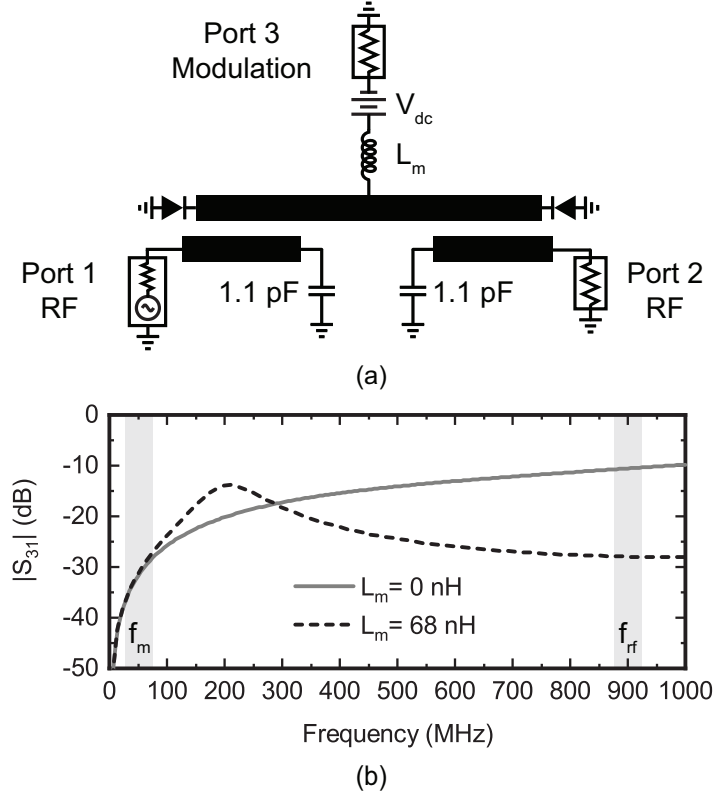
Figure 4.7: (a) Circuit model used to study $f_m - f_{rf}$ isolation. (b) $f_m - f_{rf}$ isolation ($|S_{31}|$, dB) under no inductor and with $L_m = 68$ nH. Here, $V_{dc} = 5$V.

and therefore the even mode will deteriorate the inherent isolation.

Fig.4.7 (a) is used to study the $f_m - f_{rf}$ isolation, where an inductor is added before the dc voltage and f_m source. The inductor acts as a first order LPF, and it is worth mentioning that thanks to the virtual ground we only need to use a first order as oppose to a third order [42]. From Fig.4.7 (b), we can observe that without the inductor the isolation at f_{rf} is only 10 dB, however adding an inductor with a value of $L_m = 68$ nH increases the isolation to about 30 dB. It should be noted that increasing the value of L_m will help improving the isolation but on the expense of a larger inductor package size (more parasitics). In this work, we used an inductor value of $L_m = 68$ nH.

4.2.3   Overall IFPD Design

As a final step, we combine the FPD geometrical parameters extracted from the static mode with the isolator STM $f_m - f_{rf}$ isolation circuitary from the modulated mode to yield a novel filtering power divider with integrated functionality of an isolator, namely a

IFPD.

The proposed circuit is implemented on Rogers R04003 substrate with $\epsilon_r = 3.55$, tangent loss of 0.0027, and thickness of $h = 0.813\,\mathrm{mm}$. ADS momentum is used for EM simulation and optimization. It should be noted that we used vendor provided models for all passives to account for any parasitics. Fig.4.8 depicts a sketch and a photograph of the fabricated overall IFPD circuit. Optimized geometrical values are found in the inset of the figure. The prototype's size is $105\,\mathrm{mm} \times 45\,\mathrm{mm}$ ($0.59\lambda_g \times 0.42\lambda_g$), where λ_g is the guided wavelength at the design frequency.

## 4.3 Measurement Results and Discussion

Fig. 4.9 shows the measurement setup for both small and large signal characterization. The setup is composed of a 4-port VNA (Agilent E5071A), a three-channel power source (Rigol DP832), 3 bias-tees, two arbitrary function generators (Rigol DG5252), two signal generators (HP8665B), and a spectrum analyzer (Siglent SSA3021X).

The static behaviour is investigated by connecting the dc port of the bias-tees to a dc power supply and terminating their high frequency port with a $50\,\Omega$ load. The supplied dc bias voltages are $V_{dc1} = 4.81\,\mathrm{V}$, $V_{dc2} = 5.06\,\mathrm{V}$, and $V_{dc3} = 4.2\,\mathrm{V}$. The difference in the bias voltage of each resonator is due to the following reasons: First, during the overall EM optimization process, the method of port tuning is implemented [59, 60] in order to maintain the desired equal-ripple return loss response. As a result, the resonant frequency, and hence the bias voltage, of each resonator is different. Second, as to compensate for any asymmetry that can arise from the unequal fabrication tolerance and parasitics of each varactor.

The simulated and measured responses for exciting the prototype from ports 1 ($|S_{11}|$, $|S_{21}|$, and $|S_{31}|$) and 2 ($|S_{22}|$, $|S_{12}|$, and $|S_{32}|$) are depicted in Fig. 4.10 (a) and Fig. 4.10 (b), respectively. Due to the circuit symmetry only port 2 responses are reported. From Fig. 4.10 (a), it is clear that the prototype shows simultaneously the behaviour of a band-pass filter with flat passband and an equal split power divider. The measured insertion loss ($|S_{21}|$) is $5.8\,\mathrm{dB}$ ($3 + 2.8\,\mathrm{dB}$), which is mainly due to the conductor loss, varactor
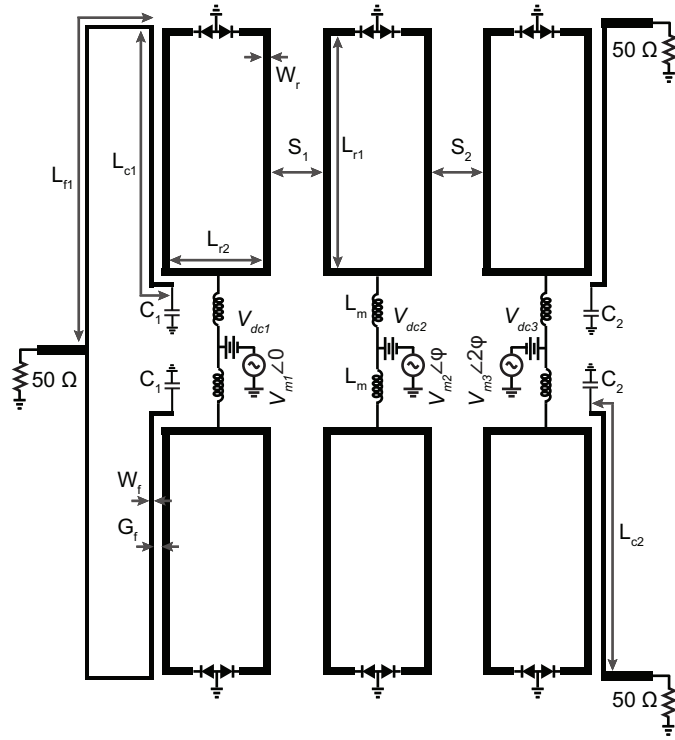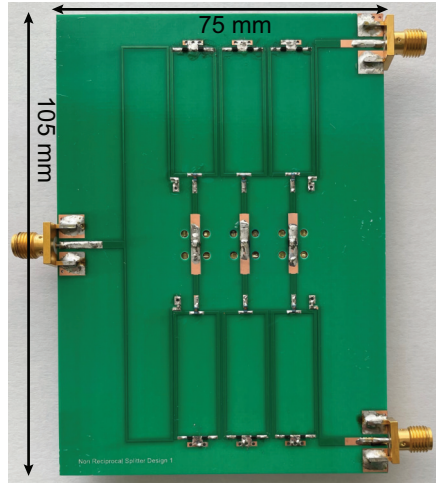
Figure 4.8: (a) Illustration of overall IFPD circuit and (b) Photograph of the fabrication PCB. Here, $L_{f1} = 55.02$ mm, $L_{c1} = 33.14$ mm, $L_{r1} = 28.48$ mm, $L_{r2} = 9.34$ mm, $S_1 = 0.66$ mm, $S_2 = 0.56$ mm, $W_r = 0.73$ mm, $W_f = 0.42$ mm, $G_f = 0.2$ mm.

loss, and the small fractional bandwidth of the filter. The measured 3-dB bandwidth is 53 MHz. The measured input matching ($|S_{11}|$) is better than 15 dB across the bandwidth. Fig.4.11 depicts the measured in-band amplitude and phase imbalances, which reports
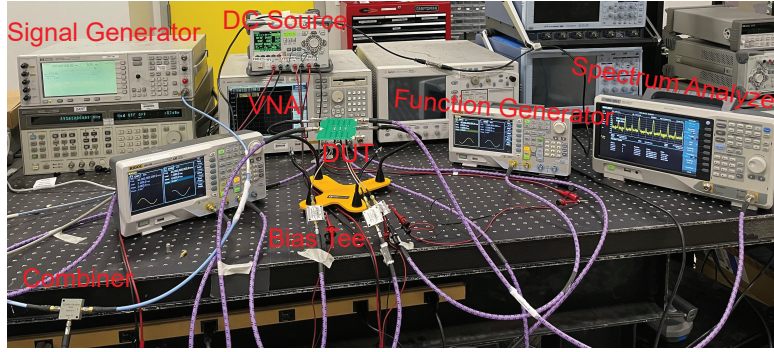
Figure 4.9: Photograph for the measurement setup.

that the amplitude imbalance is below 1 dB. Meanwhile, the maximum phase imbalance is 10° at the edge of the passband.

For the excitation from port 2, as shown in Fig. 4.10 (b) since we are in the static mode, therefore the response is reciprocal i.e. $|S_{12}| = |S_{21}|$. The measured matching ($|S_{22}|$) is better than 10 dB across the bandwidth. Furthermore, the measured port-to-port isolation $|S_{32}|$ is around 12 dB. This low port-to-port isolation is an inherent property in microwave T-junction splitter. As will be discussed, the application of STM will enhance the port-to-port isolation.

Second, the circuit is modulated with 3 sinusoidal signals (generated by two phase-locked arbitrary function generators) of frequency $f_m = 45$ MHz, progressive phase of $\phi = 55°$, and amplitudes of $V_{m1} = 1$ V, $V_{m2} = 1.09$ V, and $V_{m3} = 0.91$ V. Fig.4.12 (a) illustrates the response due to exciting from port 1. Apart from a small reduction in the passband, the response still has a filtering power divider characteristics. Moreover, the measured insertion loss ($|S_{21}|$) is 6.37 dB ($3 + 3.37$ dB). The additional 0.6 dB loss in the modulated case as compared to the static case is due to the generation of intermodulation products during STM. The measured 3-dB bandwidth is 45 MHz. The measured input matching ($|S_{11}|$) is better than 10 dB across the bandwidth.

Fig. 4.12 (b) depicts the excitation from port 2. The measured input matching ($|S_{22}|$) is better than 10 dB across the bandwidth. Under STM, the reverse transmission ($|S_{12}|$) is attenuated to become less than 20 dB across the band. To highlight the non-reciprocal response, Fig. 4.13 compares the forward ($|S_{21}|$) and reverse ($|S_{12}|$) transmission, where
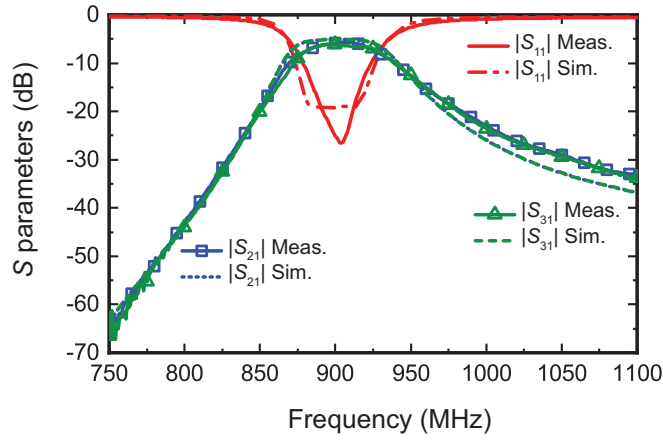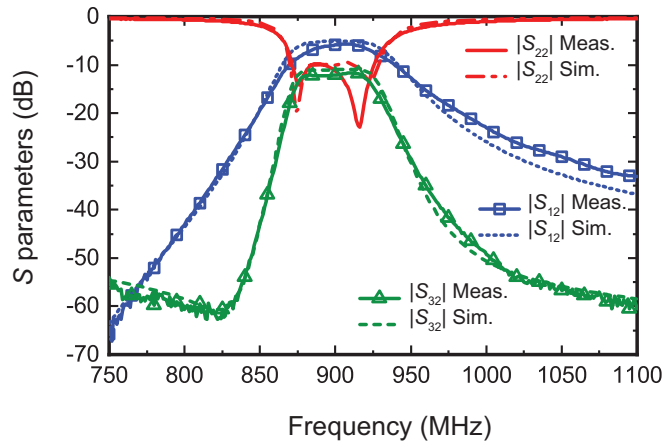
Figure 4.10: Measured and simulated Static S-parameters (a) $|S_{11}|$, $|S_{21}|$, and $|S_{31}|$. (b) $|S_{22}|$, $|S_{32}|$, and $|S_{12}|$.
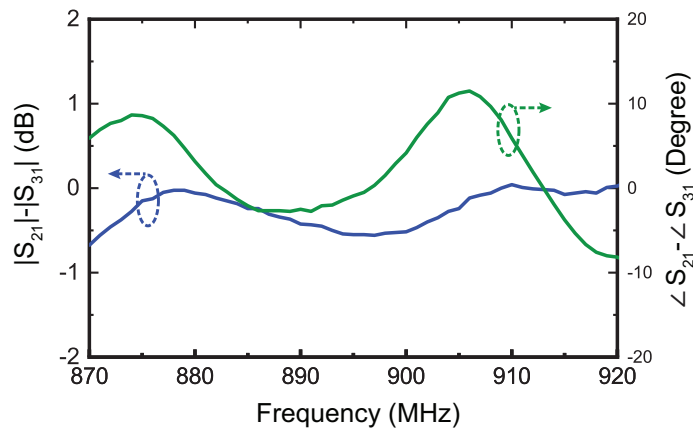
Figure 4.11: Measured amplitude and phase imbalance.
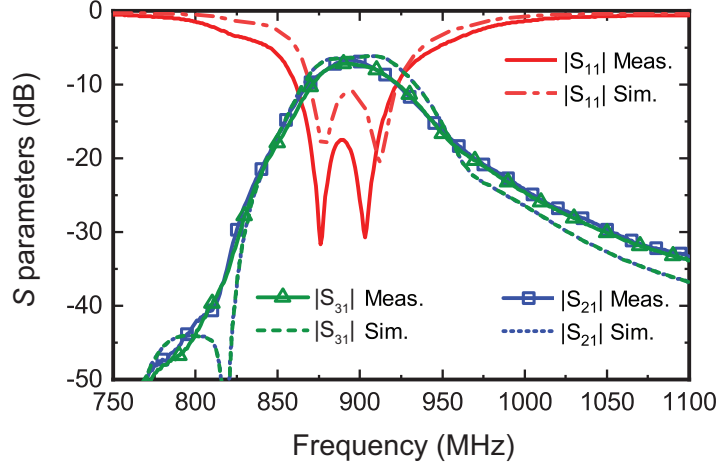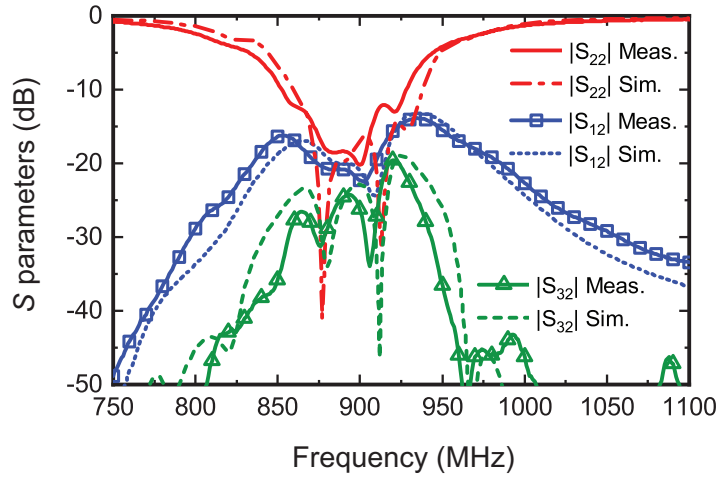
Figure 4.12: Measured and simulation S-parameters under modulation: (a) $|S_{11}|$, $|S_{21}|$, and $|S_{31}|$. (b) $|S_{22}|$, $|S_{32}|$, and $|S_{12}|$.

a directivity ($D = |S_{21}| - |S_{12}|$) of 14 dB is achieved across the band. Furthermore, the port-to-port isolation ($|S_{32}|$) shows two deep notches around 30 dB at the passband edges, and it is better than 20 dB throughout the operational bandwidth.

Fig. 4.14 compares $|S_{32}|$ in the modulated and static cases. It is clear that the $|S_{32}|$ improved significantly by at least 15 dB. It is worth mentioning that the poor port-to-port isolation of microwave T-power dividers is conventionally tackled by adding a resistor in-between the ports i.e. realizing a Wilkinson power divider. Herein, we alleviated the need of a resistor, and achieved a deep $|S_{32}|$ through the application of STM.
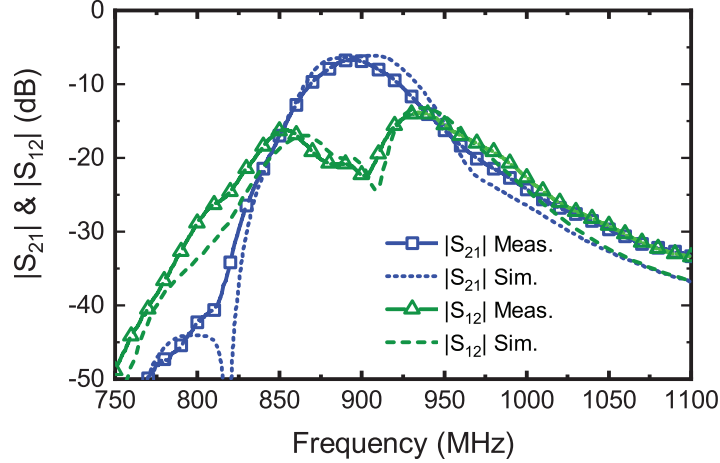
Figure 4.13: Measured and simulation forward S_{21} and reverse S_{12} transmission.
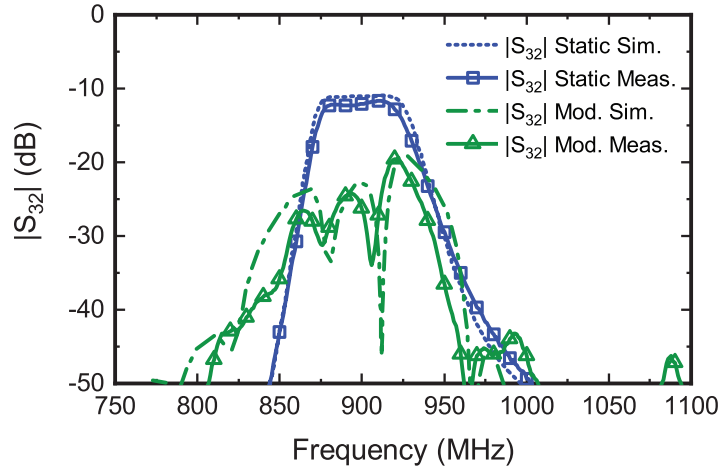
Figure 4.14: Measured and simulation port-to-port isolation S_{32} in static and modulated modes.

The harmonics generated due to the application of STM are examined using a single tone RF signal at frequency $f_0 = 890$ MHz and power of $P_{in} = -15$ dBm. When the tone is injected at port 1 using a signal generator (HP8665B), port 2 is connected to a spectrum analyzer (Siglent SSA3021X) and port 3 is terminated to $50\,\Omega$. In the following discussion, the resulting output spectrum will be referred to as P_{21}. Similarly, we injected a signal through port 2, and observed the spectrum at port 1 and port 3 successively, where their output spectra will be referred to as P_{12} and P_{32}, respectively. Fig. 4.15 depicts the resulting spectrum, where all output spectra are normalized to the output power at port 2 when injecting the signal from port 1 (P_{21}).

78

At 890 MHz, we can observe the non-reciprocal response due to STM, since P_{12} is lower than P_{21} by about 14 dB. This result agrees well with the measured directivity observed in the S-parameters. In addition, the port-to-port isolation is evident as the P_{32} is lower than P_{21} by about 20 dB. From the figure, we could also observe the first order intermodulation products f_{rf}-$f_m = 845$ MHz and $f_{rf}+f_m = 935$ MHz, which are lower than the carrier tone by 22 dBc and 12 dBc, respectively. Although not shown here for clarity, higher order harmonics of the modulation frequency also exists in the spectrum, however these tones are independent of the input RF signal, and can be removed digitally from the spectrum.

Next, the prototype power handling is investigated by using single tone and two-tone tests. For the single tone test, the input tone power is swept using the same setup used in the harmonic analysis, while for the two tone test, a combiner is used to combine two tones at 885 MHz and 895 MHz i.e. 5 MHz separation from the prototype center frequency. The simulated and measured data for both tests are depicted in Fig. 4.16. The prototype shows an input 1 dB compression point of P1dB $= 3.5$ dBm, and an input third order intercept point of IIP3 $= 8$ dBm.
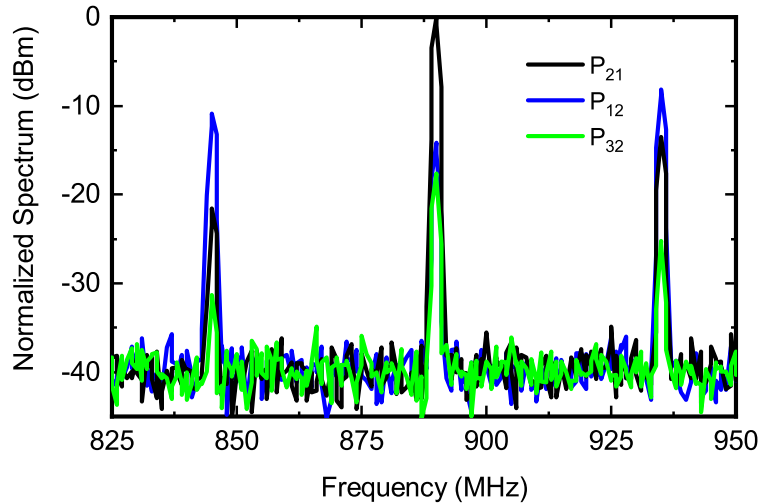
Figure 4.15: Measured spectrum normalized to the forward transmission output power. Here, P_{21} is the output power at port 2 when exciting from port 1. P_{12} is the output power at port 1 when exciting from port 2. P_{32} is the output power at port 3 when exciting from port 2.
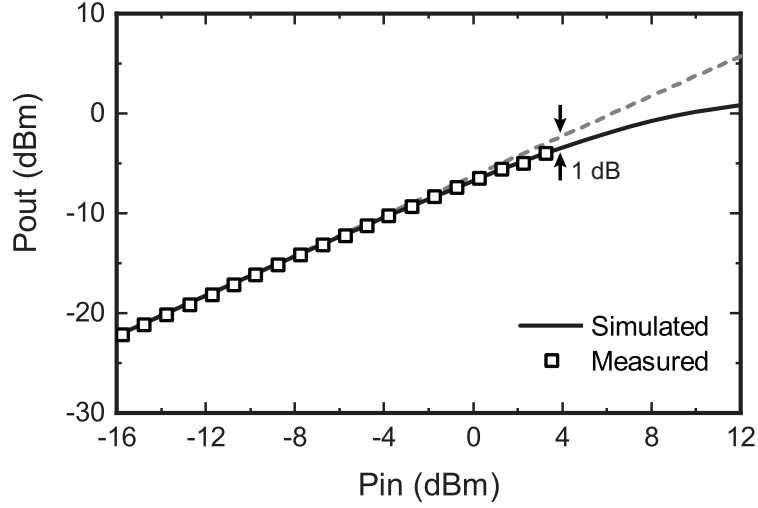
(a)
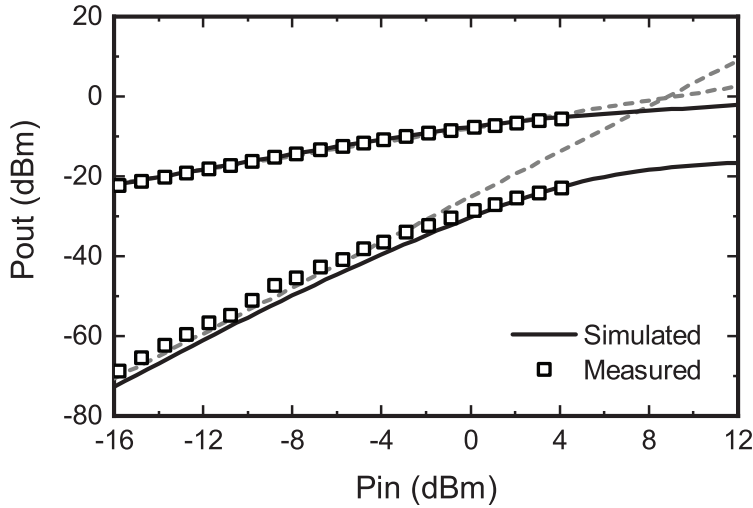
(b)

Figure 4.16: Measured and simulated (a) P1dB and (b) IIP3.

4.4 Conclusion

This chapter presents a novel multi-functional microwave circuit, namely an isolating and a filtering 3-dB power divider. The co-design of a bandpass filter and a 3-dB power divider is achieved by using even/odd analysis and simple coupling matrix synthesis method. Meanwhile, the integration of the functionality of an isolator is enabled through the application of spatial-temporal modulation. The introduced concepts are verified by the good correlation between the simulation and measurement results. Finally, the introduced

concepts can be extended to other microwave components, such as couplers and antennas, which would give rise to a new breed of low cost and miniaturized RF front-ends.

4.5 Acknowledgement

Chapter 5

Conclusion

5.1 Summary

In this dissertation, the analysis, design, and optimization of non-reciprocal higher-order magnetic-free microwave circuits are presented.

In chapter 2, a generic synthesis method for single-ended bandpass/Y second order STM-based circulators is presented. The proposed method is based on the observation that the circulator optimum modulated passband response is almost identical to that of a static 2-port filter whose order corresponds to the number of resonators in the circulator arm. This finding suggests that the circulator design can be done in two steps: First, the circulator static 3 port network response is synthesized based on the desired passband characteristics. Second, the circulator modulated response is optimized by the parametric study of the modulation frequency and depth. Furthermore, the proposed methodology is studied for different filter 3-dB FBW cases. For each case the optimum 20-dB IX FBW and the corresponding modulation parameters are recorded. Based on that, a linear relationship between the static filter 3-dB FBW and the circulator 20-dB IX FBW is found. This relationship can act as a guideline for designing second order STM-based circulators with arbitrary 20-dB IX FBW. For demonstration, a second order circulator with wideband 20-dB IX FBW is designed and fabricated. The fabricated prototype shows a 20-dB IX FBW of 15.4 %, low insertion loss of 4 dB, and good impedance matching of 12 dB.

In chapter 3, the behaviour of 2nd, 3rd, and 4th order STM-based circulators are rigorously studied. Based on that, the following conclusions are drawn: First, increasing the order has the advantage of giving sharper roll-off i.e. higher out-of-band rejection. Second, increasing the order did not provide additional poles in the reflection and isolation responses. In addition, the insertion loss/modulation frequency dependency is investigated for all orders, where our study shows that the application of STM creates images of the passband at the intermodulation frequencies. Moreover, increasing the order results in creating more images at higher mixing products, leading to an increase in the insertion loss. Furthermore, the Nyquist sampling theorem is used to set a lower limit on the modulation frequency ($f_m = 2 \, \mathrm{BW}$, where BW is the 3-dB bandwidth of the circulator-constitutive 2-port filter) as to avoid aliasing. Aliasing cause distortion in the circulator passband and limits the insertion loss to above $3 \, \mathrm{dB}$. Moreover, the passband images create transmission zeros in the circulator response. Thus, increasing the modulation frequency pushes the transmission zeros away from the passband causing a reduction in the insertion loss. Another important point to mention is that increasing the modulation frequency reduces the $f_{rf} - f_m$ isolation. As a result, a value of $f_m = 1.6 \, \mathrm{BW}$ is proposed as a compromise. Also, the relationship between the modulated circulator 20-dB IX FBW and the static filter 3-dB FBW is investigated. It is revealed that a linear relationship exists, which is independent of the modulation frequency as well as it is valid for all investigated orders.

Chapter 4 presents a 3-dB microwave power divider with the integrated functionality of a bandpass filter and an isolator. As discussed in chapter 2, the static and modulated responses of a circulator can be designed separately without significantly affecting the overall passband. This concept is also applied in this design, where the co-design of a bandpass filter and a 3-dB power divider (i.e. a filtering power divider) is first realized in the static mode, then the isolator functionality is added in the modulated mode through the application of STM. As a proof-of-concept, an isolating and filtering power divider is designed at center frequency of $900 \, \mathrm{MHz}$ and fractional bandwidth of $5\,\%$. In the static mode, a 3-pole Chebyshev filter with passband ripple of $0.043 \, \mathrm{dB}$ is chosen. Moreover,

the resonators are implemented as folded varactor-loaded $\lambda/2$ transmission lines. Furthermore, to account for the power division functionality, the filter input quality factor is doubled i.e. the filter is designed with asymmetric input/output quality actors. In the modulated mode, the varactors are modulated spatially and temporally , and the corresponding optimum modulation parameters are found via parametric studies. The measured overall response of the fabricated isolating and filtering power divider shows an insertion loss of 3.37 dB, a port-to-port isolation better than 20 dB across the band, a 20-dB reverse transmission isolation bandwidth of 45 MHz, and an impedance match at all ports better than 10 dB across the operating bandwidth.

5.2   Future Work

For future work, the following suggestions are made:

- To fulfill the demand for high communication data rates, there is an on-going pursuit to migrate to the millimeter-wave (mm-wave) frequencies. In mm-wave regime, the multi-GHz of bandwidth can significantly increase the achievable data rate per channel according to the Shannon theorem. The non-reciprocal circuits presented in this work are implemented by lumped or transmission line components. At mm-wave frequencies, these components suffer from high losses, and therefore can not be used in the design of non-reciprocal microwave circuits at these frequencies. To tackle this issue, cavity resonators in the form of rectangular/circular waveguides or substrate-integrated waveguides are proposed as an alternative structure to replace the lumped/transmission line based resonators.

- The modulating signals used in the application of STM are applied through arbitrary-function generators that are available in the lab. In practice, an integrated local oscillator or a frequency synthesizer is needed for the generation of the modulation signals. Moreover, the design of phase shifters are also needed to provide the necessary progressive phase shift between the space-time modulated resonators.

Appendix A

Appendix

A.1 2D Variation of modulation parameters for 2nd, 3rd, and 4th order circulators

In chapter 3, we wanted to study the circulator modulated behaviour as we increase the circulator order (n=2,3, and 4). To that end, we have performed a 2D nested loop for f_m and d_m. For each circuit, we vary the f_m from $75\,\mathrm{MHz}$ to $225\,\mathrm{MHz}$ with step of $25\,\mathrm{MHz}$. For each f_m value, d_m is swept from 0.2 to 0.5. Figures A.1, A.2, and A.2 depict the $|S_{11}|$, $|S_{21}|$, and $|S_{31}|$ of 2nd, 3rd, and 4th order circulator, respectively. From the figure, it is clear that the circulator behaviour of all orders are near-optimum (we say it is near-optimum since the isolation is below $20\,\mathrm{dB}$) for d_m=0.4 and 0.5.
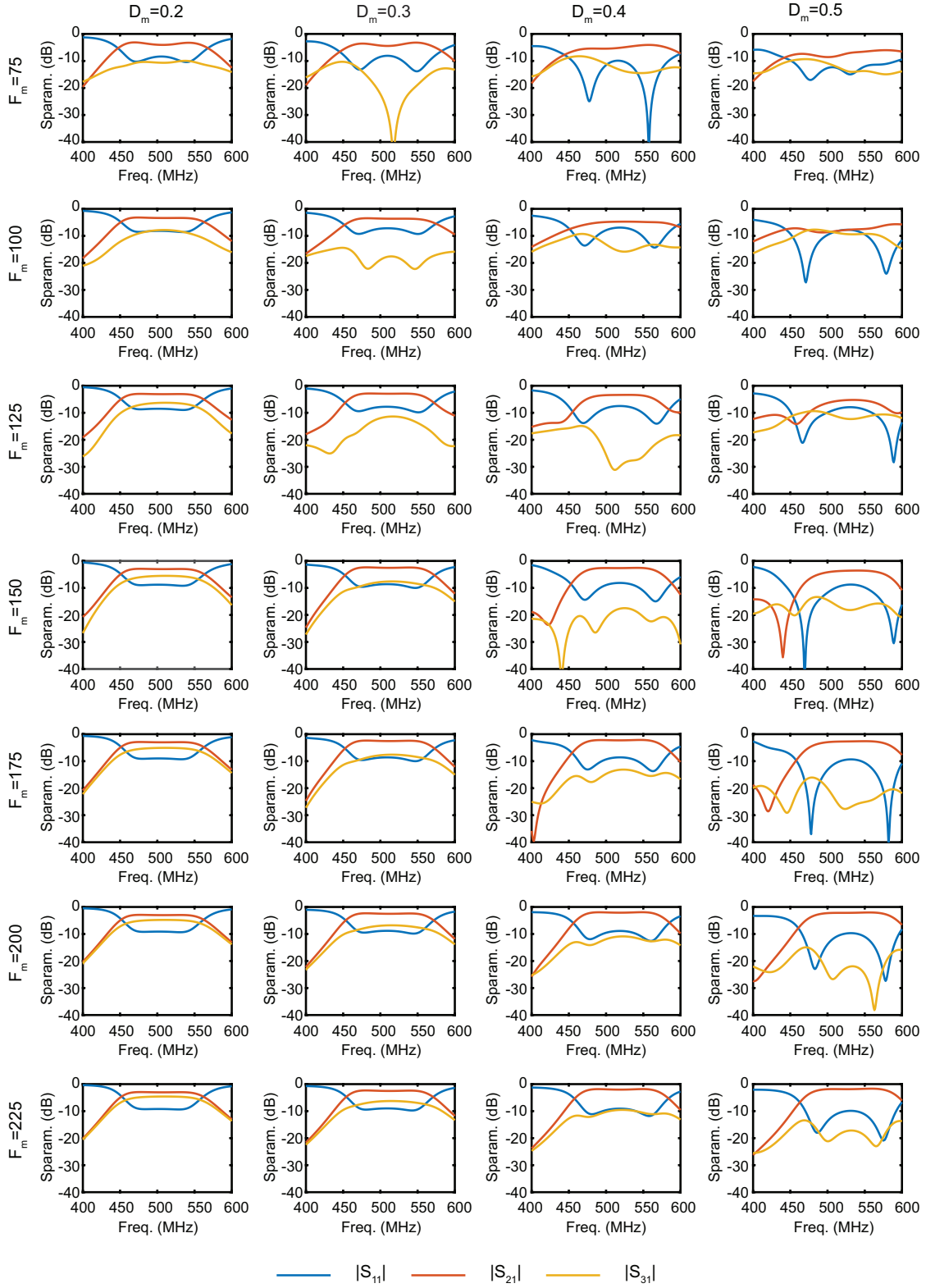
Figure A.1: Variation of modulation parameters f_m and D_m of 2nd order circulator.
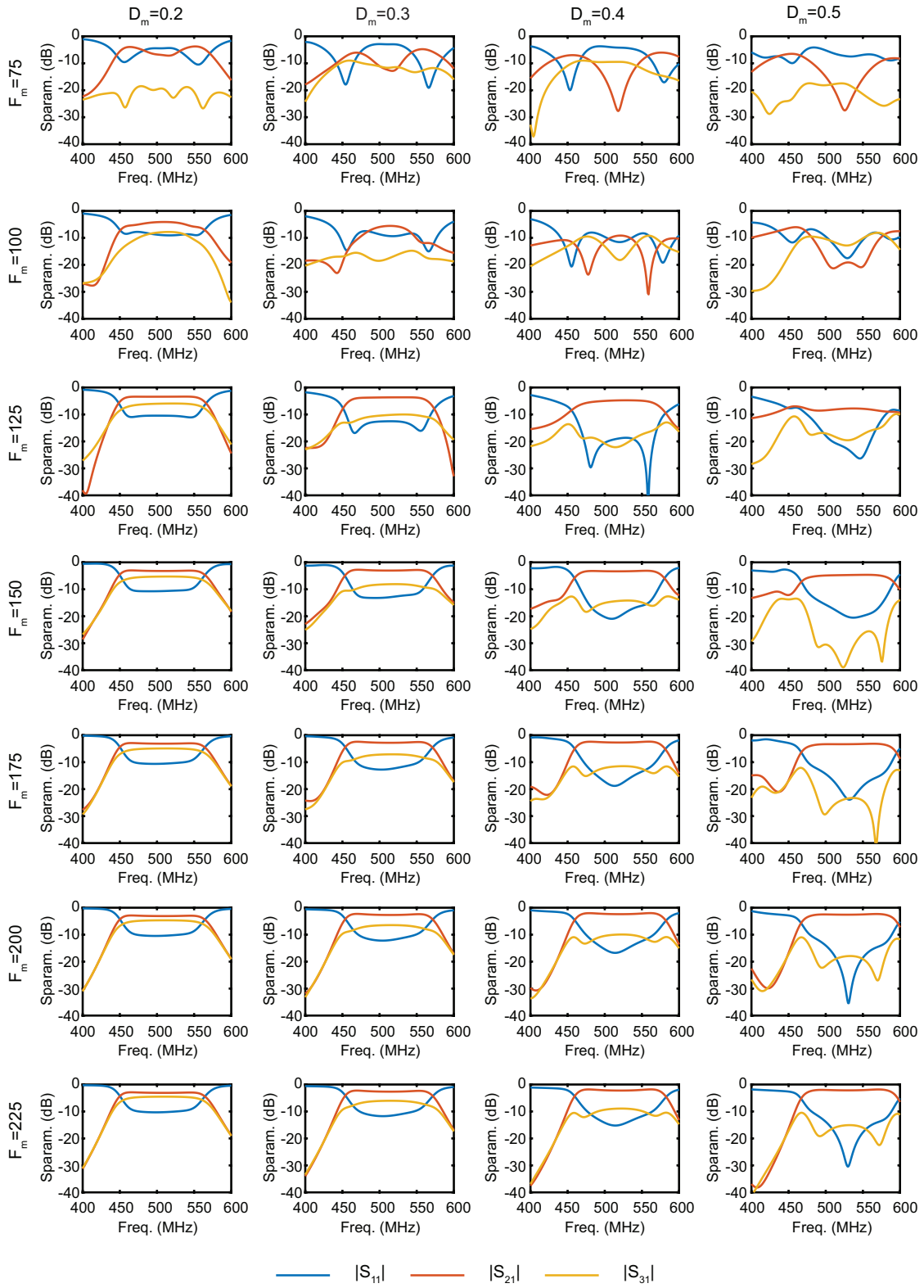
Figure A.2: Variation of modulation parameters f_m and D_m of 3rd order circulator.
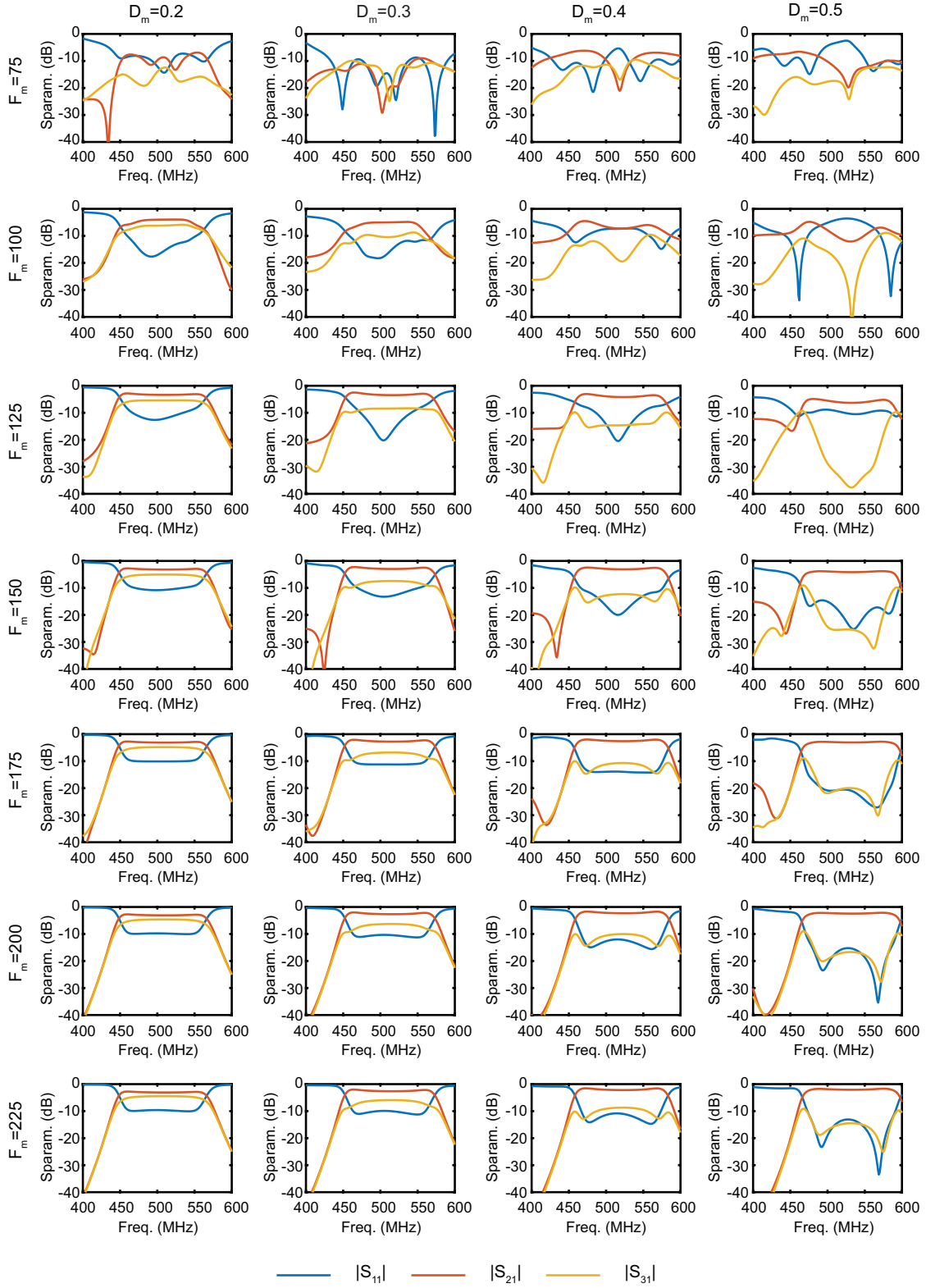
Figure A.3: Variation of modulation parameters f_m and D_m of 4th order circulator.

References

[1] C. Caloz, A. Alù, S. Tretyakov, D. Sounas, K. Achouri, and Z.-L. Deck-Léger, "Electromagnetic nonreciprocity," *Phys. Rev. Applied*, vol. 10, p. 047001, Oct 2018. [Online]. Available: https://link.aps.org/doi/10.1103/PhysRevApplied.10.047001

[2] V. S. Asadchy, M. S. Mirmoosa, A. Díaz-Rubio, S. Fan, and S. A. Tretyakov, "Tutorial on electromagnetic nonreciprocity and its origins," *Proceedings of the IEEE*, vol. 108, no. 10, pp. 1684–1727, 2020.

[3] N. Reiskarimian, A. Nagulu, T. Dinc, and H. Krishnaswamy, "Nonreciprocal electronic devices: A hypothesis turned into reality," *IEEE Microwave Magazine*, vol. 20, no. 4, pp. 94–111, April 2019.

[4] A. Kord and A. Alu, "Magnetless circulators based on synthetic angular-momentum bias: Recent advances and applications," *IEEE Antennas and Propagation Magazine*, 2020.

[5] A. Kord, H. Krishnaswamy, and A. Alù, "Magnetless circulators with harmonic rejection based on n-way cyclic-symmetric time-varying networks," *Phys. Rev. Applied*, vol. 12, p. 024046, Aug 2019. [Online]. Available: https://link.aps.org/doi/10.1103/PhysRevApplied.12.024046

[6] S. Tanaka, N. Shimomura, and K. Ohtake, "Active circulators: The realization of circulators using transistors," *Proceedings of the IEEE*, vol. 53, no. 3, pp. 260–267, March 1965.

[7] T. Kodera, D. L. Sounas, and C. Caloz, "Magnetless nonreciprocal metamaterial (MNM) technology: Application to microwave components," *IEEE Transactions on Microwave Theory and Techniques*, vol. 61, no. 3, pp. 1030–1042, March 2013.

[8] S. Qin, Q. Xu, and Y. E. Wang, "Nonreciprocal components with distributedly modulated capacitors," *IEEE Transactions on Microwave Theory and Techniques*, vol. 62, no. 10, pp. 2260–2272, Oct 2014.

[9] N. A. Estep, D. L. Sounas, and A. Alù, "Magnetless microwave circulators based on spatiotemporally modulated rings of coupled resonators," *IEEE Trans. on Microw. Theory and Techn.*, vol. 64, no. 2, pp. 502–518, Feb 2016.

[10] C. Sounas, Dimitrios L.and Caloz and A. Alú, "Giant non-reciprocity at the subwavelength scale using angular momentum-biased metamaterials," *Nature Communications*, vol. 4, p. 2407, Sep 2013.

[11] M. Nafe, X. Wu, and X. Liu, "A wideband magnetic-free circulator using spatiotemporal modulation of 2-pole bandpass filters," in *2019 IEEE Radio and Wireless Symposium (RWS)*, Jan 2019, pp. 1–3.

[12] D. M. Pozar, *Microwave Engineering*. Wiley, 2012.

[13] A. Kord, D. L. Sounas, and A. Alù, "Microwave nonreciprocity," *Proceedings of the IEEE*, vol. 108, no. 10, pp. 1728–1758, 2020.

[14] T. Kodera, D. L. Sounas, and C. Caloz, "Magnetless nonreciprocal metamaterial (MNM) technology: Application to microwave components," *IEEE Transactions on Microwave Theory and Techniques*, vol. 61, no. 3, pp. 1030–1042, March 2013.

[15] H.-C. Kuo, C.-C. Lin, C.-H. Yu, P.-H. Lo, J.-Y. Lyu, C.-C. Chou, and H.-R. Chuang, "A Fully Integrated 60-GHz CMOS Direct-Conversion Doppler Radar RF Sensor With Clutter Canceller for Single-Antenna Noncontact Human Vital-Signs Detection," *IEEE Transactions on Microwave Theory and Techniques*, vol. 64, no. 4, pp. 1018–1028, 2016.

[16] D. L. Sounas, J. Soric, and A. Alú, "Broadband passive isolators based on coupled nonlinear resonances," *Nature Electronics*, vol. 1, pp. 113–119, February 2018.

[17] D. L. Sounas and A. Alù, "Fundamental bounds on the operation of fano nonlinear isolators," *Phys. Rev. B*, vol. 97, p. 115431, Mar 2018. [Online]. Available: https://link.aps.org/doi/10.1103/PhysRevB.97.115431

[18] A. Kord, D. L. Sounas, and A. Alù, "Microwave nonreciprocity," *Proceedings of the IEEE*, vol. 108, no. 10, pp. 1728–1758, 2020.

[19] P. K. Tien, "Parametric amplification and frequency mixing in propagating circuits," *Journal of Applied Physics*, vol. 29, no. 9, pp. 1347–1357, 1958.

[20] A. L. CULLEN, "A travelling-wave parametric amplifier," *Nature*, vol. 181, no. 4605, p. 332, 1958.

[21] A. Kord, D. L. Sounas, and A. Alù, "Magnet-less circulators based on spatiotemporal modulation of bandstop filters in a delta topology," *IEEE Trans. on Microw. Theory and Techn.*, vol. 66, no. 2, pp. 911–926, Feb 2018.

[22] ——, "Pseudo−linear time-invariant magnetless circulators based on differential spatiotemporal modulation of resonant junctions," *IEEE Trans. on Microw. Theory and Techn.*, vol. 66, no. 6, pp. 2731–2745, June 2018.

[23] M. Baraani Dastjerdi, S. Jain, N. Reiskarimian, A. Natarajan, and H. Krishnaswamy, "Analysis and design of a full-duplex two-element mimo circulator-receiver with high tx power handling exploiting mimo rf and shared-delay baseband self-interference cancellation," *IEEE Journal of Solid-State Circuits*, vol. 54, no. 12, pp. 3525–3540, 2019.

[24] H.-C. Chou, Y.-H. Kao, C.-C. Peng, Y.-J. Wang, and T.-S. Chu, "An x-band frequency-modulated continuous-wave radar sensor system with a single-antenna interface for ranging applications," *IEEE Transactions on Microwave Theory and Techniques*, vol. 66, no. 9, pp. 4216–4231, 2018.

[25] L. Ranzani and J. Aumentado, "Circulators at the quantum limit: Recent realizations of quantum-limited superconducting circulators and related approaches," *IEEE Microwave Magazine*, vol. 20, no. 4, pp. 112–122, 2019.

[26] B. J. Chapman, E. I. Rosenthal, J. Kerckhoff, B. A. Moores, L. R. Vale, J. A. B. Mates, G. C. Hilton, K. Lalumière, A. Blais, and K. W. Lehnert, "Widely tunable on-chip microwave circulator for superconducting quantum circuits," *Phys. Rev. X*, vol. 7, p. 041043, Nov 2017. [Online]. Available: https://link.aps.org/doi/10.1103/PhysRevX.7.041043

[27] J. Kerckhoff, K. Lalumière, B. J. Chapman, A. Blais, and K. Lehnert, "On-chip superconducting microwave circulator from synthetic rotation," *Physical Review Applied*, vol. 4, no. 3, Sep 2015. [Online]. Available: http://dx.doi.org/10.1103/PhysRevApplied.4.034002

[28] J. G. Andrews, S. Buzzi, W. Choi, S. V. Hanly, A. Lozano, A. C. K. Soong, and J. C. Zhang, "What will 5g be?" *IEEE Journal on Selected Areas in Communications*, vol. 32, no. 6, pp. 1065–1082, 2014.

[29] M. Biedka, Y. E. Wang, Q. M. Xu, and Y. Li, "Full-duplex rf front ends : From antennas and circulators to leakage cancellation," *IEEE Microwave Magazine*, vol. 20, no. 2, pp. 44–55, 2019.

[30] N. Reiskarimian, T. Dinc, J. Zhou, T. Chen, M. B. Dastjerdi, J. Diakonikolas, G. Zussman, and H. Krishnaswamy, "One-way ramp to a two-way highway: integrated magnetic-free nonreciprocal antenna interfaces for full-duplex wireless," *IEEE Microwave Magazine*, vol. 20, no. 2, pp. 56–75, Feb 2019.

[31] D. Korpi, J. Tamminen, M. Turunen, T. Huusari, Y. Choi, L. Anttila, S. Talwar, and M. Valkama, "Full-duplex mobile device: pushing the limits," *IEEE Communications Magazine*, vol. 54, no. 9, pp. 80–87, Sep. 2016.

[32] A. Sabharwal, P. Schniter, D. Guo, D. W. Bliss, S. Rangarajan, and R. Wichman, "In-band full-duplex wireless: Challenges and opportunities," *IEEE Journal on Selected Areas in Communications*, vol. 32, no. 9, pp. 1637–1652, 2014.

[33] L. Laughlin, M. A. Beach, K. A. Morris, and J. L. Haine, "Electrical balance duplexing for small form factor realization of in-band full duplex," *IEEE Communications Magazine*, vol. 53, no. 5, pp. 102–110, 2015.

[34] E. Ahmed, A. M. Eltawil, Z. Li, and B. A. Cetiner, "Full-duplex systems using multireconfigurable antennas," *IEEE Transactions on Wireless Communications*, vol. 14, no. 11, pp. 5971–5983, Nov 2015.

[35] A. Kord, D. L. Sounas, Z. Xiao, and A. Alù, "Broadband cyclic-symmetric magnetless circulators and theoretical bounds on their bandwidth," *IEEE Trans. on Microw. Theory and Techn.*, vol. 66, no. 12, pp. 5472–5481, Dec 2018.

[36] D. Korpi, J. Tamminen, M. Turunen, T. Huusari, Y. Choi, L. Anttila, S. Talwar, and M. Valkama, "Full-duplex mobile device: pushing the limits," *IEEE Communications Magazine*, vol. 54, no. 9, pp. 80–87, Sep. 2016.

[37] L. Laughlin, M. A. Beach, K. A. Morris, and J. L. Haine, "Electrical balance duplexing for small form factor realization of in-band full duplex," *IEEE Communications Magazine*, vol. 53, no. 5, pp. 102–110, May 2015.

[38] N. Reiskarimian and H. Krishnaswamy, "Magnetic-free non-reciprocity based on staggered commutation," *Nature Communications*, vol. 7, p. 11217, Apr 2016.

[39] N. Reiskarimian, J. Zhou, and H. Krishnaswamy, "A cmos passive lptv nonmagnetic circulator and its application in a full-duplex receiver," *IEEE Journal of Solid-State Circuits*, vol. 52, no. 5, pp. 1358–1372, May 2017.

[40] T. Dinc, A. Nagulu, and H. Krishnaswamy, "A millimeter-wave non-magnetic passive soi cmos circulator based on spatio-temporal conductivity modulation," *IEEE Journal of Solid-State Circuits*, vol. 52, no. 12, pp. 3276–3292, Dec 2017.

[41] A. Nagulu, T. Dinc, Z. Xiao, M. Tymchenko, D. L. Sounas, A. Alù, and H. Krishnaswamy, "Nonreciprocal components based on switched transmission lines," *IEEE Transactions on Microwave Theory and Techniques*, vol. 66, no. 11, pp. 4706–4725, Nov 2018.

[42] X. Wu, X. Liu, M. D. Hickle, D. Peroulis, J. S. Gómez-Díaz, and A. Álvarez Melcón, "Isolating bandpass filters using time-modulated resonators," *IEEE Transactions on Microwave Theory and Techniques*, vol. 67, no. 6, pp. 2331–2345, June 2019.

[43] X. Wu, M. Nafe, A. A. Melcón, J. Sebastián Gómez-Díaz, and X. Liu, "A nonreciprocal microstrip bandpass filter based on spatio-temporal modulation," in *2019 IEEE MTT-S International Microwave Symposium (IMS)*, June 2019, pp. 9–12.

[44] J.-S. Hong and M. J. Lancaster, *Microstrip Filters for RF / Microwave Applications*. Wiley, 2001.

[45] "https://store.skyworksinc.com/products/detail/smv1234079lf-skyworks/20991/."

[46] C. Yang and P. Gui, "85−110 GHz CMOS Magnetic-Free Nonreciprocal Components for Full-Duplex Transceivers," *IEEE J. Solid-State Circuits*, vol. 54, no. 2, pp. 368–379, Feb 2019.

[47] A. Kord, M. Tymchenko, D. L. Sounas, H. Krishnaswamy, and A. Alù, "CMOS Integrated Magnetless Circulators Based on Spatiotemporal Modulation Angular-Momentum Biasing," *IEEE Trans. Microw. Theory and Techn.*, vol. 67, no. 7, pp. 2649–2662, July 2019.

[48] A. V. Oppenheim, A. S. Willsky, and S. H. Nawab, *Signals & Systems (2nd Ed.)*. USA: Prentice-Hall, Inc., 1996.

[49] Y. Wu, L. Jiao, Z. Zhuang, and Y. Liu, "The art of power dividing: A review for state-of-the-art planar power dividers," *China Communications*, vol. 14, no. 5, pp. 1–16, 2017.

[50] F.-J. Chen, L.-S. Wu, L.-F. Qiu, and J.-F. Mao, "A four-way microstrip filtering power divider with frequency-dependent couplings," *IEEE Transactions on Microwave Theory and Techniques*, vol. 63, no. 10, pp. 3494–3504, 2015.

[51] C.-F. Chen, T.-Y. Huang, T.-M. Shen, and R.-B. Wu, "Design of miniaturized filtering power dividers for system-in-a-package," *IEEE Transactions on Components, Packaging and Manufacturing Technology*, vol. 3, no. 10, pp. 1663–1672, 2013.

[52] C.-F. Chen and C.-Y. Lin, "Compact microstrip filtering power dividers with good in-band isolation performance," *IEEE Microwave and Wireless Components Letters*, vol. 24, no. 1, pp. 17–19, 2014.

[53] L. Gao, X. Y. Zhang, and Q. Xue, "Compact tunable filtering power divider with constant absolute bandwidth," *IEEE Transactions on Microwave Theory and Techniques*, vol. 63, no. 10, pp. 3505–3513, 2015.

[54] A. Kord, D. L. Sounas, and A. Alù, "Achieving full-duplex communication: Magnetless parametric circulators for full-duplex communication systems," *IEEE Microwave Magazine*, vol. 19, no. 1, pp. 84–90, Jan 2018.

[55] X. Wu, X. Liu, M. D. Hickle, D. Peroulis, J. S. Gomez-Diaz, and A. Álvarez Melcon, "Isolating bandpass filters using time-modulated resonators," *IEEE Transactions on Microwave Theory and Techniques*, vol. 67, no. 6, pp. 2331–2345, 2019.

[56] A. Alvarez-Melcon, X. Wu, J. Zang, X. Liu, and J. S. Gomez-Diaz, "Coupling matrix representation of nonreciprocal filters based on time-modulated resonators," *IEEE Transactions on Microwave Theory and Techniques*, vol. 67, no. 12, pp. 4751–4763, 2019.

[57] J. Zang, S. Wang, A. Alvarez-Melcon, and J. S. Gomez Diaz, "Nonreciprocal filtering power dividers," *AEU - International Journal of Electronics and Communications*, vol. 132, p. 153609, 2021. [Online]. Available: https://www.sciencedirect.com/science/article/pii/S1434841121000066

[58] X. Wu, M. Nafe, A. A. Melcon, J. S. Gomez-Diaz, and X. Liu, "Frequency tunable non-reciprocal bandpass filter using time-modulated microstrip $\lambda_g/2$ resonators," *IEEE Transactions on Circuits and Systems II: Express Briefs*, vol. 68, no. 2, pp. 667–671, 2021.

[59] D. G. Swanson, "Narrow-band microwave filter design," *IEEE Microwave Magazine*, vol. 8, no. 5, pp. 105–114, 2007.

[60] D. Swanson and G. Macchiarella, "Microwave filter design by synthesis and optimization," *IEEE Microwave Magazine*, vol. 8, no. 2, pp. 55–69, 2007.